MATERIALS SCIENCE DIVISION
COAL TECHNOLOGY TENTH QUARTERLY REPORT,

January—March 1977

U of C-AUA-USERDA

ARGONNE NATIONAL LABORATORY, ARGONNE, ILLINOIS

The facilities of Argonne National Laboratory are owned by the United States Government. Under the terms of a contract (W-31-109-Eng-38) between the U. S. Energy Research and Development Administration, Argonne Universities Association and The University of Chicago, the University employs the staff and operates the Laboratory in accordance with policies and programs formulated, approved and reviewed by the Association.

ANL-77-41

ARGONNE NATIONAL LABORATORY
9700 South Cass Avenue
Argonne, Illinois   60439

MATERIALS SCIENCE DIVISION
COAL TECHNOLOGY TENTH QUARTERLY REPORT,
JANUARY—MARCH 1977

Principal Investigator

W. A. Ellingson
Project Leader

TABLE OF CONTENTS

iii

TABLE OF CONTENTS (Contd.)

LIST OF FIGURES

LIST OF FIGURES (Contd.)

LIST OF TABLES

MATERIALS SCIENCE DIVISION
COAL TECHNOLOGY TENTH QUARTERLY REPORT,
JANUARY–MARCH 1977

HIGHLIGHTS

Task A — Evaluation of Ceramic Refractories for Slagging Gasifiers
(C. R. Kennedy, R. J. Fousek, D. J. Jones, and R. B. Poeppel)

Construction of the bottom section of the slag-corrosion furnace, redesigned to provide prototypic thermal gradients, has been completed and the fourth 500-h corrosion test has been initiated. Three types of silicon carbide and one type of silicon-oxynitride brick are being exposed to an acidic slag.

Task B — Evaluation of Ceramic Coatings for Coal-conversion Plants
(S. Danyluk, R. B. Poeppel, and G. M. Dragel)

Samples that were exposed to the corrosion-erosion furnace by Solar, Inc., were shipped to ANL on March 11, 1977.

Task C — Application and Development of Nondestructive Evaluation Methods for Coal-conversion Processes (W. A. Ellingson, W. J. Shack, and C. L. Johnson)

The first field data on erosive wear of an installed refractory-lined transfer line was obtained this quarter. This has shown that 100% of the lining could be eroded in less than 300 h of exposure to Al_2O_3 particles. Acoustic-emission data on high-density isothermally heated refractory bar specimens has shown that most crack damage occurs below 500°C and the cooling rate may be as important as the heat-up rate. Field tests on acoustic-valve-leak-detection systems have shown that known leaks can be detected and separated from structure-borne noise using a frequency window between 375 and 800 kHz.

Task D — Corrosion Behavior of Materials in Coal-conversion Processes
(K. Natesan and O. K. Chopra)

Preliminary corrosion experiments were conducted in gas mixtures that have been selected for exposure of uniaxial tensile specimens of Type 310 stainless steel, Incoloy 800, Inconel 671, and U. S. Steel alloy 18-18-2. The results after a 200-h exposure showed that the first three of the above alloys developed Cr-rich oxide scale. The U. S. Steel alloy 18-18-2 developed a (Cr,Fe) sulfide scale that had a significantly larger growth rate than the oxide scales in other specimens. It seems that the ~ 2 wt % Si in the U. S. Steel alloy 18-18-2 alters the mode of attack from oxidation to sulfidation. Results are presented on the corrosion behavior of materials, as a function of oxygen partial pressure in a multicomponent gas environment, and on the experiments to evaluate the role of steam in the gas mixture on the corrosion

behavior of Type 310 stainless steel. The results showed that steam is not an essential component to establish the corrosion behavior of an alloy as long as the same oxygen, sulfur, and carbon potentials are simulated by adjusting the relative amounts of different molecular gas species.

Task E -- <u>Erosion Behavior of Materials in Coal-conversion Processes</u>
       (W. J. Shack)

        A brief literature review of analytical models for the two-phase flow of particles and fluids is presented. A qualitative discussion of a set of simplified equations is given, and a dimensionless group that describes the fraction of particles actually impacting the wall of an elbow is developed. Quantitative results, which show the importance of particle diameter, are given for particle trajectories in an elbow that carries fluid.

Task F -- <u>Component Performance and Failure Analysis</u>   *(S. Danyluk,*
       G. M. Dragel, and M. D. Gorman)

        Components from the Morgantown Energy Research Center high-pressure gas producer (rabble arm), the HYGAS Pilot Plant (alonized coupons), and the Synthane Pilot Plant (steam line) were analyzed to determine the cause of the failure. Three final reports have been issued: "EBV Ball-valve stem Failure -- Synthane Coal-gasification Pilot Plant," "Analysis of the Gate-valve Failure -- Grand Forks Energy Research Center Fixed-bed Slagging Gasifier Pilot Plant," and "Failure Analysis of the Thermocouple Assembly in the HYGAS Coal Pretreatment Vessel."

MATERIALS SCIENCE DIVISION
COAL TECHNOLOGY TENTH QUARTERLY REPORT,
JANUARY-MARCH 1977

ABSTRACT

This broad-base materials engineering program, begun in October 1974, includes studies on both ceramic (refractory) and metallic materials presently being used or intended for use in coal-conversion systems. Appropriate laboraory and field experiments are integrated such that the results have immediate impact on the present pilot-plant and proposed demonstration-plant designs. This quarterly report, for the period January-March 1977, presents the technical accomplishments.

INTRODUCTION

The economical conversion of coal into cleaner and more usable fuels will be advanced through use of durable materials systems. The present report is the tenth quarterly progress report submitted by Argonne National Laboratory to the Division of Materials and Exploratory Research/ERDA Fossil Energy under project Number 7106, "Materials Technology for Coal Conversion Processes."

The project includes six tasks: (A) evaluation of ceramic refractories exposed to coal-slag abrasion-corrosion typical of that encountered in slagging gasifiers; (B) evaluation of coat performance under erosive environments; (C) development, evaluation, and application of nondestructive evaluation methods applicable to coal-conversion systems, such as in-situ erosive-wear detection/monitoring; (D) development of analytical models to predict corrosion behavior, e.g., phase transformations, of iron- and nickel-base alloys in gaseous environments; (E) development of analytical models to predict the erosive-wear behavior of materials used in coal-conversion plants, and (F) analysis of failed coal-gasification plant components. Progress in all Tasks is discussed in the present report.

Task A -- Evaluation of Ceramic Refractories for Slagging Gasifiers
(C. R. Kennedy, R. J. Fousek, D. J. Jones, and R. B. Poeppel)

The purpose of Task A is to evaluate the resistance of various refractory bricks to attack by molten coal slag. Three tests in the slag-abrasion rig have been reported.[1-5] These tests were characterized by an atypical temperature gradient within the bricks. During this quarter, the rig was modified to produce prototypic gradients, and the fourth 500-h test was initiated.

In the modified rig (Fig. 1), the bricks are provided with water-cooled chills. Water temperature and flow are monitored so heat flux can be calculated. Standard 9 x 4-1/2 x (3,2)-in. wedge bricks are used (if wedges are not available, straights are cut to fit). The narrow ends of the bricks are exposed to the slag. The wedges are cut to three different lengths so

1

that three temperature gradients can be studied. Bricks of four compositions can be tested simultaneously. Each chill cools three bricks of one length and composition. The center brick is thereby shielded from the effects of neighboring bricks of different lengths and/or compositions.

The fourth test includes silicon carbide with three bond systems: (1) nitride bonded (number 91), (2) silicate bonded (number 93), and (3) oxynitride bonded (number 37). A silicon oxynitride (number 36) composition is also included. Thermocouples have been inserted in the center brick in each group of three at 12.7 mm (0.5 in.), 38.1 mm (1.5 in.), 88.9 mm (3.5 in.), and 177.8 mm (7 in.), for full-length bricks, from the hot face (Fig. 2). To enhance heat transfer between the chills and bricks, a high thermal conductivity silicon carbide cement* mixed with a monoaluminum phosphate solution† has been utilized. Thermal profiles in each of the brick types and lengths, prior to the addition of the slag, are shown in Fig. 3.

The slag composition utilized in the fourth test is simulated Montana Rosebud (Table I). (The initially high Fe_2O_3 content resulted from a batching error and was corrected shortly after the test began.) The slag temperature was maintained at $\sim 1500°C$.

Task B -- Evaluation of Ceramic Coatings for Coal-conversion Plants
(S. Danyluk, R. B. Poeppel, and G. M. Dragel)

Metallic specimens with partial or total coatings were exposed to high-velocity (~ 38 m/s) char particles at 980°C and a pressure of 240 kPa (35 psi) for 3.6 Ms (1000 h). The coating materials and substrates are listed in Table II. The exposure was conducted in the ERDA-owned corrosion-erosion furnace by Solar, Inc. The samples were shipped to ANL on March 11, 1977. Metallographic investigation of the samples will be conducted in the coming quarter.

Task C -- Application and Development of Nondestructive Evaluation Methods for Coal-conversion Processes (W. A. Ellingson, W. J. Shack, and C. L. Johnson)

1. Erosive-wear Detection and Monitoring

a. Metallic Transfer Lines

(1) Laboratory Ultrasonic Studies. The erosive-wear data on the HYGAS cyclone separator, which was reported in Ref. 5, were analyzed to obtain estimates of the wear rate of the Stellite liner and the azimuthal distribution of wear within the cyclone.

The most severe wall-thickness reduction observed in the cyclone inlet region occurred along the inlet centerline. The azimuthal distribution of measurement locations along the centerline is shown in Fig. 4a. Bitter[6] has presented a qualitative argument to describe the distribution of erosive

---

*Carborundum Company, Keasbey, NJ.

†Mobil Chemical Company, Richmond, VA.

wear in the elbow of a pipe (Fig. 4b). The results reported by Bitter
suggest that maximum erosion for the cyclone should occur in the 20-50°
azimuthal range. The actual distribution of erosive wear for ∿1000 h of
coal feed between February 1976 and June 1976 is shown in Fig. 5. Little
wear is observed in the 20-50° range. Actually, it is difficult to predict
the pattern of wear a priori. As the modeling studies reported under Task E
show, the distribution of particle impacts is a complex function of the
fluid-flow properties and the particle size and density.

An average thickness loss for the Stellite lining can be obtained
by averaging the measured values for positions ranging from 73-153°. This
average value can then be plotted as a function of exposure time,[7] as shown
in Fig. 6. In Fig. 6, the thickness loss at the time of the first measure-
ment at 1×10^8 s (200 h) was obtained by taking the difference between the
measured thickness and the initial thickness. Since the value of the initial
thickness could vary because of counterbore misalignment, differences in
coating thickness, etc., the values of the total thickness loss shown in
Fig. 6 are only approximate. The changes in thickness between measurements
are independent of these errors, however, and thus the data shown in Fig. 6
can be used to estimate the wear rate (i.e., loss of thickness per day). A
straight-line fit through the three data points gives a wear rate of
0.063 mm/100 h for a nominal particle velocity in the cyclone of 14 m/s,
a particle loading of 1.5 kg/acm (acm ≡ actual cubic meter of gas), and a
cyclone operating temperature of 315°C. Since the original thickness of the
Stellite overlay was 3.2 mm, the data indicate that the overlay will have
an operating lifetime of ∿5000 h.

(2) Field Studies. Progress will be reported in the next quarterly
report.

b. Refractory-lined Transfer Lines

(1) Gamma Radiography Development. Previous work[2-4] using gamma
radiography to examine refractory-lined transfer lines has shown that this
method can be used to define the bore and hence can be used to determine the
extent of erosive wear. During this quarter, a set of radiographic images
of the 502 Ash transfer line at the Battelle Agglomerating Ash gasifier were
taken after ∿200 h of solids (Al_2O_3 particles) circulation and compared with
the initial images obtained in February 1976. Figure 7 shows the bore geometry
before and after the 200-h exposure. Figure 8 is a schematic of the entire
flow directional change system and shows that part for which the erosive wear
data were obtained. It is interesting to note that the erosive wear on the
outside radius of the inner bore could be expected, but the erosive wear on the
inside radius of the bore would not. The inner surface wear was not caused
by erosive wear due to particle impact of the normal flow but rather by
the air-lift injection lines blowing normal stream particles into the wall.
The transfer line is presently being recast, and baseline radiographic images
of the complete section shown in Fig. 8 have been obtained for future examina-
tion.

The results of this radiography development program to date have
shown that gamma radiographic imaging can be used to

(a) Inspect refractory-lined transfer lines for bore definition.

(b) Inspect refractory-lined transfer lines for proper installation of air-lift line injections, including angle and wall thickness.

(c) Determine plugging of air-lift injectors.

(d) Determine time-dependent erosive wear of installed refractory.

A more complete analysis of the erosive-wear data obtained to date will appear in the next quarterly report.

(2) Infrared Imaging -- Pattern Recognition. During this quarter, a study of the potential use of thermal patterns obtained by infrared imaging to determine erosive wear in refractory-lined transfer lines was continued. This technique is needed to supplement the gamma-radiography development because of personnel problems encountered when the high-strength ($\approx$ 75 Ci) ^{60}Co source is used. The passive infrared-imaging camera can be used at all times but requires an appropriate heat-transfer model to allow calculation of the defect size from the thermal patterns obtained. Analytical heat-transfer models were used to determine theoretical thermal patterns from synthesized cavity defects.

The structure being modeled is a cylindrical pipe with an inner refractory layer bonded to a steel shell. The boundary conditions imposed on the two surfaces consisted of a prescribed surface temperature (750°C) on the inside (hot) surface and convective cooling on the outside surface. The computer model is being developed to study the heat transfer through the pipe under steady-state conditions.

The computer program was used to study thermal patterns in the four cases shown in Table III. Table III also shows the data used in the calculations. The selection of Case 2 permits assessment of the effects of the increase in the convective heat-transfer coefficient on thermal patterns due to, e.g., wind speed at test site. Selection of Case 3 allows examination of the effect of a refractory of lower thermal conductivity; the thermal conductivity of the steel shell is nearly invariant to minor composition changes and is therefore treated as constant in all cases. Finally, Case 4 was selected to determine the effect of changes in both the thermal conductivity and the convective heat-transfer coefficient.

Preliminary data showing the effect of changes in rectangular cavity size on the thermal patterns have been obtained. Figure 9 shows the temperature versus distance from the cavity centerline for several rectangular cavities when a steady-state temperature of 750°C (1500°F) is applied to the cavity side for the thermal conductivities, convective coefficients and refractory sizes listed in Table III. The data obtained from Fig. 9 suggest that the thermal distribution across the cavity can be modeled as a parabola. Figure 10 shows a rectangular cavity and a typical temperature distribution across the surface. From such an analysis, the temperature is

4

available as a parameter for extraction and also (a) the integrated area A, (b) the span W of any isotherm, and (c) the area change between selected isotherms. These features will be examined for applicability, and the most promising features will be used as the discriminating parameters for erosive-wear calculations.

In the studies to date, the results show that the hot-spot temperature has been found to increase rapidly with an increase in the depth of the cavity (see x-intercepts of curves in Fig. 9). When the depth of the cavity increases from 62 to 68 mm for all widths, this hot-spot temperature increases by ∿400°C. (The family of curves for the 68-mm-cavity depth lies outside the Fig. 9 region and is therefore not shown.) As mentioned above, the analysis given represents only preliminary studies. A more detailed investigation, which will include error analysis and additional parametric studies, is scheduled for the next quarter of work. Future studies will include the effect of contact resistance and implement the thermal-conductivity data being obtained in other ERDA/FE-sponsored programs.

2. Refractory-installation Practices

a. Acoustic Emission

Work has continued on the evaluation of the use of acoustic emission as a means to control the firing schedule of castable refractories. As previously reported,[4] an apparent correlation existed between the temperature internal to a thick refractory wall and the total acoustic-emission counts, N. This is not a totally unexpected result, since previous investigations[8-10] have shown that selected acoustic-emission parameters can be used as discriminators between refractory types as well as a clear indication of imminent fracture. However, the intent of this program is to show that the final response of the refractory, i.e., lifetime and mechanical reliability, can be improved by following a heating schedule which minimizes the amount of crack damage the refractory undergoes during the actual firing schedule. This means that reliable acoustic-emission data must be obtained from refractory samples during curing to 1000°C. Since commercially available acoustic-emission transducers have a maximum service temperature of 500°C, an acoustic waveguide is necessary between the specimen and the sample. The acoustic coupling between the specimen and the waveguide is very critical because the acoustic energy released in the specimen (i.e., micro- and/or macrocrack formation) must be transferred to the waveguide. Presently available couplant material cannot be used above 300-400°C. Thus, an alternative coupling mechanism must be employed. Robinson et. al.[8] employed spring-loaded mullite rods in direct contact with the specimen to obtain their results. During this quarter, we have employed embedded quartz waveguides, as shown in Fig. 11. The sample was supported in the furnace on knife edges made of high density, prefired refractory. The transducer was attached to a 25-mm-dia quartz cylinder that had been fused to the 6-mm-dia quartz waveguide. The waveguide was cast into the refractory sample such that 38 mm of waveguide were in direct contact with the sample. All samples studied this quarter were made of KAOTAB,*

---

*KAOTAB is a product of Babcock and Wilcox with a fired density of 2.4 x 10^3 kg/m^3.

which had been cast with a water content of 12% so that significant cracking would occur. The cast samples were 25 mm wide x 25 mm high and 254 mm long. The cold and hot muduli of rupture, after being exposed to different firing schedules, will be determined. During this reporting period, all samples were cured with the controlled heat-up rates shown in Table IV.

One obvious variable is the capability to reproduce samples. Presently, the samples are prepared by using a Hobart mixer and vibrated on a shaker table for a fixed amount of time, typically 60-90 s. To ensure that the procedure did not permit segregation to occur, metallographic samples have been prepared from the "bar" specimens, as shown schematically in Fig. 14. The samples are vacuum impregnated with an epoxy solution and polished, yielding a clear distribution of particle size. Figures 15 and 16 show, respectively, typical results of a transverse section (3.4X) and a longitudinal section (3.6X). The transverse section shows no apparent segregated grain structure.

Two samples were run simultaneously for statistical data variation. Figure 12 shows the total acoustic-emission count as a function of temperature for two castings run at the same heating and cooling rate but at different times. The data for castings 2 and 3 were averaged for the two samples run simultaneously. It is very interesting to note that, since the data were generated from the heating schedule shown in Table IV, significant counts do not accumulate until the maximum previous temperature has been exceeded. This was especially true when heating to 500°C after heating to 120°C. Little activity was detected during the 1000°C run. Figures 13a-c are plots of counts versus time, and the temperature ramp is superimposed for ease of interpretation. Note that, during cooling from 1000°C, a significant increase was detected, which was probably the result of damage caused by the severe cooling rate. This suggests that controlled cool-down should be considered just as controlled heat-up. An increase in acoustic activity was detected in the 120 and 500°C cool-down cycles, although not to the same extent.

All data reported herein were obtained using a 175-kHz resonant transducer with a band-pass filter of 125-250 kHz. Also, data have been taken with a 375-kHz center-frequency transducer, and the comparison will be reported next quarter.

The embedment of the quartz waveguide in the refractory gives rise to the question of whether the acoustic-emission detected is from rubbing noise caused by differences in thermal expansion or from the curing of the refractory, i.e., water evaporation, microcracking or phase transformations. In an attempt to determine whether the detected acoustic activity was caused by rubbing of the waveguide by the refractory, a two-dimensional locating system was employed with waveguides coupled to each end of the specimen. Specimens were cast and acoustic data and location information were obtained. The data show that the acoustic activity is uniform over the length of the specimen, implying that the effect of the embedded waveguide was not significant. A more complete analysis will be given next quarter.

3. Component Inspection

a. Infrared Thermal Profiling of Valves

In the development of a valve-testing program for coal-gasification systems, one important objective of the program is to verify that the valve can operate satisfactorily at high temperatures. To obtain a valid test, the heating in the tests must be accomplished in a manner that simulates actual thermal gradients, thermal stresses, and internal temperatures. Unfortunately, the temperature fields within valves in actual service are not well known, since it is difficult to make direct temperature measurements. Modeling studies are useful, but uncertainty always exists in the choice of heat-transfer coefficients, and direct confirmation by experimental techniques is desirable. During this quarter, infrared scans were made on a number of valves at the Morgantown Energy Research Center low-Btu gasification facility in an attempt to obtain direct in-situ thermal profiles.

The valves examined were the top cyclone lockhopper valve (a 6-in. full-port ball valve, MERC valve number 060), Fig. 17a, the top ash lockhopper valve (a 12-in. full-port ball valve, MERC valve number 1207), Fig. 17b, and the north bottom coal lockhopper feed valve (a 10-in. full-port ball valve, MERC valve number 1002), Fig. 17c. Reference temperatures were measured on each of the valves using a contact pyrometer, as shown in Fig. 18.

The infrared scanning system used was an AGA Thermovision Model 750, a lightweight completely portable system designed for field use. It is basically a scanning camera designed to detect emissions in the 2 to 5-μm wavelength infrared spectrum rather than the visual spectrum. The resultant image is displayed on a black and white television monitor and a picture of the object is produced where darker portions correspond to cooler sections of the object and lighter portions correspond to warmer sections of the object. The temperature range spanned by the thermal picture can be selected by the operator. Quantitative temperature measurements are made by knowing a reference temperature at one point and then using available calibration curves to identify isothermal regions (i.e., areas of equal temperature) above and below the known temperature. The isothermal regions correspond to equal tones of gray. The system enables the isothermal regions to be readily identified by superposing brightened isothermal areas on the thermal picture. The isotherm level (i.e., the isothermal area selected for brightening picture (see, e.g., Fig. 19). The ten divisions of the scale represent fractions of the temperature range spanned in the picture. A quantitative relation between the isotherm level and the temperature can be determined by using the calibration curves for the instrument.

A sequence of thermal pictures of the ash-removal valve, with the isotherm level varied to identify different isothermal areas, is shown in Fig. 19a-g). The temperature range from the hottest to the coldest part is ∿11°C. Not only are the surface thermal gradients small, but the actual surface-temperature levels [maximum temperature ∿64°C (147°F)] are surprisingly low. A second sequence of pictures at a narrower temperature range is shown in Fig. 20a-e. At this temperature range setting, it is impossible to scan the entire valve body, but greater detail and resolution are possible over a portion of the body.

7

Thermal pictures of the coal-feed lockhopper valve are shown in Fig. 21a and b. Although the camera is set on a sensitive range (nominally 2°C), little temperature variation can be observed; the "hot spots" visible in Fig. 21b are <2°C hotter than the remainder of the valve body. The actual temperature of the hot spot is 37°C (98°F), as measured with a contact pyrometer.

The infrared scans of the top cyclone lockhopper valve are shown in Fig. 22a-e. The reference temperature on the upstream side of the valve was measured as 60°C (140°F) with the contact pyrometer. As indicated in Fig. 22a, little temperature variation occurs over the upper and lower halves of the valve (i.e., they appear in the picture as a uniform gray tone), although the flanges appear slightly cooler, i.e., a darker gray tone. Because the temperatures were so uniform when the isotherm level was adjusted to brighten isothermal areas, it was difficult to obtain properly exposed pictures for a permanent record. When the shutter speed was increased, it was possible to obtain Fig. 22b. The high shutter speed decreases visual resolution because the faster speed captures the raster lines of the scanning camera. It is clear from the picture, however, that the upper and lower housings of the valve are quite uniform in temperature. The flange was examined separately at a more sensitive range (=5); as Fig. 22e shows, the flange is also nearly isothermal.

It should be noted that variations in emissivity are not significant for the valves examined. The painted surface of the top cyclone was in good condition, but the surfaces of the other valves were more weathered. Painted surfaces and oxidized surfaces have emissivities close to the ideal blackbody value (=1) assumed in the calculation of the temperatures from the infrared data. A few new bright metal scratches were visible on the top cyclone lockhopper valves, which gave spurious readings because of the low emissivity of brightly polished metal.

The thermal profiles obtained for the three valves are similar in character. The surface temperatures were rather low, and no significant thermal gradients were observed.

It is tempting to conclude that this implies the only significant temperature gradients in the valves are through the thickness of the body. However, the use of infrared techniques for the analysis of temperature variations in compact, thick-walled objects constructed from materials of high thermal conductivity is not well developed, and some comparisons with our modeling studies must be made before any firm conclusions can be drawn.

b. Acoustic Monitoring of Valves

(1) Valve Leak Detection by Acoustic Emission. Field testings of an acoustic-emission valve leak-detection system was carried out at the MERC low-Btu coal-gasification facility and the Synthane high-Btu pilot plant. The objectives of the field measurements were to investigate the sensitivity of the acoustic-emission measurements to the background "noise" present in an operating coal-gasification facility and to determine whether leakage indications could actually be obtained on in-service valves.

The acoustic-emission system used for the field tests consisted of an AET Model 140A preamplifier, an AET Model 201 single-channel processor, and a HP 3475B digital multimeter. A Tektronix Model 314 portable oscilloscope was used to visually monitor the acoustic-emission signals. Three transducers were examined: AET Models 175L, 375L, and 750L. These are resonant-response transducers with peaks at 175, 375, and 750 kHz, respectively.

Tests were run on the top cyclone lockhopper valve (a 6-in. full-port ball valve), the top ash lockhopper valve (a 12-in. full-port ball valve) and the north bottom coal feed lockhopper valve (a 10-in. full-port ball valve) at MERC. In addition, measurements were made on structural members in an attempt to distinguish between a "local" flow noise generated by a leaking valve and general background structure-borne noise associated with the overall operation of the gasifier.

The top cyclone valve is, in the opinion of MERC personnel, a "good" valve with very little leakage. Acoustic-emission data were taken at five points on the valve body and at two points on the gasifier structure near the valve. The measurement points on the valve are indicated in Fig. 23a-e. The measurement points on the nearby structure are indicated in Fig. 24a and b. The measurements taken with the 175-kHz resonance transducer are listed in Table V. The AET 201 processor and preamplifier combination were adjusted to amplify the signals detected by the transducer by 80 dB. The valves given in Table V are root-mean-square (rms) acoustic-emission outputs. The readings in the column labeled "noise" are rms voltages due to electrical system noise and airborne noise. Although the 175-kHz transducer is a shear-wave-type device, it did appear to detect sound waves (i.e., dilatation waves) at the high gain used. The values shown in Table V indicate that acoustic-emission signals could be detected on the valve and these signals are not simply general structure-borne noise. It is not clear that the signals can be attributed to leakage through the valve. MERC personnel[11] have suggested that the signals could be due to acoustic emissions generated by particles striking the cyclone.

The measurement locations for the top ash lockhopper valve are shown in Fig. 25a-e. The acoustic-emission measurements are summarized in Table VI. The system gain was again 30 dB. The measured values showed large fluctuations in contrast to the measurements on the top cyclone lockhopper valve. Again, the acoustic emissions detected in the vicinity of the valve are significantly higher than the background noise detected on a nearby structure.

The measurement locations for the north bottom coal-feed lockhopper valve are shown in Fig. 26a-c. Acoustic-emission measurements on this valve were made with 176- and 375-kHz transducers. The results of the measurements are shown in Table VII. Again, the signals fluctuated rapidly over a rather wide range. The amplitude of the signal produced by the 375-kHz transducer is substantially smaller than that produced by the 175-kHz transducer. If the signal is actually produced by gas leakage, it is in agreement with our laboratory studies, which show the emitted acoustic signals produced by turbulent flow through an orifice or leak decrease with an increase in frequency. However, the decrease can also be explained by the increase in attenuation with frequency of structure-borne noise.

Acoustic-emission measurements were also made at the Synthane Pilot Plant. The valves examined here were the north and south lower Petrocarb feed valves, which are located between the lockhoppers and the primary injection system. Although the audible noise level at the Morgantown and Synthane installations seems to be similar, much more difficulty was encountered at Synthane with stray airborne noise. The 175-kHz resonant transducer was particularly affected. With the system gain at 80 dB and the transducer simply exposed to the air, readings ranged from 0.170 V (the transducer held at arm length outside the structure) to 1.0 V (in the interior of the gasifier structure). A leak from a gasket below the south valve was audible; extraordinarily large readings were obtained from the flange areas near the leak, and it seems likely that the leak also produced a large amount of airborne high-frequency noise.

The measurement locations for the north valve are shown in Fig. 27a-e, and the results of the noise measurements for the 176, 375, and 750 kHz transducers are summarized in Table VIII. Again, as expected, the 175-kHz transducer is a more sensitive detector of structure-borne sound; according to Synthane personnel, it is likely that some leakage occurred in these valves, however, it is not certain at this time that leakage was, in fact, the source of the structure-borne sound detected.

The measurement locations on the south feed valve and nearby structural components are shown in Fig. 28a-e. On the south coal-feed valve, a gasket between the valve and the primary injection system was leaking. This type of leak is similar to a valve leak in that it involves a gas flow from high pressure to low pressure through a small orifice. Of course, the gasket leak is audible because the sound is free to radiate, but the structure-borne signals due to the gasket leak should be similar to those produced by an internal valve leak. The leak was near the location shown in Fig. 28c. The acoustic-emission measurements are summarized in Table IX. All three transducers were able to locate the leak near measurement location (c). However, the 175- and 375-kHz transducers also picked up considerable air and structure-borne noise, although the 375 kHz transducer was much less sensitive in this regard. The 750-kHz transducer seems totally unaffected by airborne noise. It was also sufficiently sensitive to identify the leak on the south valve; however, it is still uncertain whether it is sufficiently sensitive to detect the smallest leaks of interest.

These results suggest that to develop a leak-detection system for use in an operating gasification plant, 375-750 kHz is a desirable operating range; certainly, transducers operating at <175 kHz (e.g., low g-level accelerometers) seem unsuitable for such systems. Although the acoustic noise generated by a leak is broadbanded with frequencies ranging from 1 kHz to 1 MHz, most of the energy appears to be concentrated below 150 kHz, thus, an unavoidable trade off occurs between sensitivity and immunity to background noise. Additional signal processing can, to a certain extent, overcome this problem. To develop a workable system, additional tests will be needed on full-size valves with known leak rates. The MERC valve test facility has the capability to monitor flow rates through full-size valves, and MERC personnel have expressed their desire to cooperate in performing additional tests using their facility.

10

(2) Laboratory Studies. Progress will be reported in the next quarterly report.

Task D -- <u>Corrosion Behavior of Materials in Coal-conversion Processes</u>
  (K. Natesan and O. K. Chopra)

The objectives of this program are to (1) develop uniaxial tensile data on four selected commercial alloys upon exposure to simulated multicomponent gas environments, (2) experimentally evaluate the high-temperature corrosion behavior of iron- and nickel-base alloys in gas environments with a wide range of oxygen, sulfur, and carbon potentials, and (3) develop a systems approach based upon available thermodynamic and kinetic information so that possible corrosion problems in different coal-conversion processes can be evaluated.

The experimental program that involves generation of uniaxial tensile data on four selected alloys upon exposure to the multicomponent gas environments has been discussed in detail in an earlier report.[4] As a consequence of the severe corrosion rates that have been observed at high-temperatures ~1010°C (1850°F) in the IIT Research Institute program, the temperatures for the exposure of tensile specimens in the present program have been lowered to 750°C (1380°F), 871°C (1600°F), and 982°C (1800°F). Preliminary corrosion experiments were conducted at 875°C for 25- and 200-h durations using gas mixture No. 1, the composition of which is listed in Table X. The oxygen, sulfur, and carbon potentials that correspond to the selected gas mixture for a reaction temperature of 875°C were calculated using the computer program and are also listed in Table X. These experiments were conducted to establish the type and thickness of corrosion-product scale (oxide versus sulfide) that forms upon exposure to the selected complex gas mixture prior to the exposure of uniaxial tensile specimens for a 1000-h time period in the same environment. Apart from the four alloys selected for tensile property evaluation, four additional alloys were included in the corrosion experiments. The chemical compositions of the alloys are listed in Table XI. The experiments were conducted in a corrosion testing rig, the details of which were reported earlier.[5]

Figure 29 shows macroscopic photographs of the corrosion specimens after 25- and 200-h exposures to the gas environment at 875°C. The samples from both experiments were examined using optical metallography, and the phases present were identified using a scanning-electron microscope (SEM) equipped with an energy-dispersive x-ray analyzer. Extensive analyses were made on specimens of Type 310 stainless steel, Incoloy 800, Inconel 671, and U. S. Steel alloy 18-18-2 during this quarter. Figure 30 shows the x-ray image of the iron specimen and the Fe and S distribution in the scale/alloy interface region of the sample after a 26-h exposure. The scale is predominantly iron sulfide, which indicates that the sulfur potential established in these experiments was higher than that for the Fe/FeS equilibrium. A similar behavior was observed for iron exposed for 200 h at 875°C. Figures 31-34 are x-ray photographs showing the specimen image, metallic element (Cr, Ni, Fe, Si, and Al) distribution, and sulfur distribution in the scale/alloy interface regions of the samples of Type 310 stainless steel, Incoloy 800, Inconel 671, and U. S. Steel alloy 18-18-2, respectively, after a 25-h exposure to the gas environment at 875°C. The photographs clearly

indicate the presence of sulfur in the scale region in all the alloys, although the chromium content of the alloys ranges from 18 to 48 wt %. The thickness of the scale layer is in the range of 10 to 25 μm in these specimens after a 25-h exposure. Intergranular penetration of sulfur in the alloy regions is minimal in these specimens. Based upon the oxygen and sulfur potentials calculated for the gas composition listed in Table X, only the oxide layer should be observed in iron- and nickel-base alloys containing >18 wt % Cr upon exposure to this gas environment. Since the apparatus had been used earlier for experimental runs with high partial pressures of sulfur, it is possible that the sulfur from the reactor walls may be contributing to the sulfidation of the alloys. As a result, the reactor chamber was fired with hydrogen for 50 h at 875°C, and subsequently another experiment was made with the same alloys exposed to the same gas environment for 200 h.

Figures 35-37 show the x-ray specimen images, metallic element distributions, and the sulfur distribution in the scale/alloy interface regions of the samples of Type 310 stainless steel, Incoloy 800, and U. S. Steel alloy 18-18-2, respectively, after a 200-h exposure to a gas environment at 875°C. Figures 38 and 39 are SEM photographs of the scale/alloy regions in specimens of Inconel 671 and U. S. Steel alloy 18-18-2 after a 200-h exposure to the gas environment at 875°C. Figures 35-39 show that in all the alloys, except U. S. Steel alloy 18-18-2, the scales were predominantly chromium-rich oxide and sulfur was essentially absent, which indicates that the mode of interaction is oxidation rather than sulfidation in this particular environment. This observation is in excellent agreement with the calculated partial pressures for oxygen and sulfur in the gas mixture and the thermochemical diagrams for different Fe-Cr-Ni alloys. In the case of U. S. Steel alloy 18-18-2, the scale was predominantly chromium and iron sulfide (Fig. 39), and the alloy/scale interface had a large concentration of silicon. It seems that the silicon at the interface lowers the oxygen potential sufficiently to change the type of interaction from an oxidation to a sulfidation mode. Silicon enrichment at the scale/alloy interface was also observed in Type 310 stainless steel and Incoloy 800, but no deleterious effect due to silicon was observed in these alloys. The Silicon concentration in Type 310 stainless steel and Incoloy 800 is in the range of 0.35 to 0.40 wt % and is 2.05 wt % in U. S. Steel alloy 18-18-2. Since the two former alloys behave differently than the U. S. Steel alloy, it is essential to establish the role of alloy additions such as silicon on the protective scale formation upon exposure to multicomponent gas environments. During the next quarter, uniaxial tensile specimens of the selected alloys will be exposed for 1000 h to the gas mixture with the composition listed in Table X.

The experimental program is being continued to evaluate the corrosion behavior of iron- and nickel-base alloys in gas environments with a wide range of oxygen, sulfur, and carbon potentials. The composition of the alloys selected for this phase of the program is given in Table XI. Figure 40 shows the macroscopic photographs of specimens of different alloys that have been exposed for 25 h at 750°C to gas environments that contained the same sulfur potential (2.8×10^{-8} atm) but different oxygen potentials. The partial pressure of oxygen was varied from 1×10^{-20} to 4.2×10^{-23} atm (from left to right in Fig. 40). A macroscopic photograph of different specimens exposed for 25 h at 875°C to several oxygen pressures between 1.9×10^{-18} and 1.7×10^{-20} atm is shown in Fig. 41. The oxygen, sulfur, and

carbon potentials established in these experiments are listed in Table XII. It is evident from Figs 40 and 41 that the mode of interaction changes from oxidation to sulfidation as the oxygen potential decreases (from left to right in Figs. 40 and 41). Iron specimens formed iron sulfide scales in all instances, which indicates that the partial pressure of sulfur in these experiments was larger than that established by Fe/FeS equilibrium. At 875°C, the Inconel 671 specimen that was exposed to the lowest oxygen pressure showed the formation of liquid nickel sulfide upon exposure to the environment (the rightmost specimen of Inconel 671 in Fig. 41).

The samples of Type 310 stainless steel, after exposure to different gas environments listed in Table XII, were examined with the SEM equipped with an energy-dispersive x-ray analyzer. Figures 42a–c are photographs of cross sections of specimens exposed at 750°C and oxygen pressures of 1.0×10^{-20}, 2.4×10^{-21}, and 4.1×10^{-22} atm, respectively. The SEM photographs of a specimen exposed to an oxygen pressure of 4.2×10^{-23} atm are shown in Fig. 43 (identified as d). The sulfur partial pressure in these experiments was $\sim 2.8 \times 10^{-8}$ atm. Figure 42a and b shows that specimens develop predominantly Cr-rich oxide scales, the thicknesses of which were approximately 2 to 4 μm. The alloy specimens also developed some internal sulfide particles to a depth of 3 to 8 μm. The specimens in Figs. 42c and 43 developed (Cr,Fe) sulfide scales, the thicknesses of which were 50 and 210 μm, respectively. The internal sulfidation and intergranular penetration of sulfur were also significant in the specimens shown in Figs. 42c and 43. The thicknesses of the internally affected zones in these specimens were 40 and 150 μm, respectively.

Figure 44 shows SEM photographs of Type 310 stainless steel samples that have been exposed at 875°C for 25 h to mixed gas environments with the following partial pressures of oxygen: 1.9×10^{-18}, 5.5×10^{-19}, 2.4×10^{-19}, and 1.7×10^{-20} atm. The sulfur partial pressure in these experiments was $\sim 2.9 \times 10^{-7}$ atm. The figure shows that the specimens develop ~ 5-μm-thick Cr-rich oxide scales at all oxygen potentials, except at 1.7×10^{-20} atm where an ~ 210-μm-thick (Cr, Fe) sulfide scale was observed. The thickness of the internal sulfidation zone was in the range of 20 to 40 μm in specimens that developed oxide scale. The thickness of the internal sulfidation and intergranular penetration zone in the specimen exposed to the lowest oxygen pressure was ~ 170 μm. It is evident from these results that the chemical interaction between an alloy of a given chemical composition and the gas environment is strongly dependent on the oxygen and sulfur potentials that are prevalent in the environment. The results also show that the growth rates of the sulfide scales are larger than those of oxides, and the extent of intergranular penetration of sulfur is significantly greater when the alloys do not develop oxide scales. Additional experiments are being conducted to evaluate the kinetic aspects of scale formation and the influence of alloy chemistry on the interaction processes between materials and complex gas environments.

Steam is one of the major oxidizing species in multicomponent gas environments in different coal-gasification processes. The steam content in the gas mixtures can range from 14 vol % in the Battelle-Union Carbide process to 52 vol % in the Bi-Gas process.[12,13] As a result, it is essential

to establish the role of steam on the oxidation-sulfidation behavior of materials. This can be accomplished by the exposure of materials to gas mixtures with the same oxygen, sulfur, and carbon potentials that are established with and without steam in the gas mixtures. Such a comparison would also establish the degree to which a thermodynamic equilibrium is achieved at the test temperature by the reactions of different molecular gas species employed in the experiments. For this purpose, two experiments were conducted in which the same oxygen, sulfur, and carbon potentials were established by mixing various gas species of CO, CO_2, H_2, CH_4, H_2S, and H_2O. The established gas compositions are listed in Table XII (columns 7 and 10 indicated by the arrows at the bottom of the table). In one run, a steam content of 8.6 vol % was used, whereas no steam was used in the other run. Oxygen and sulfur partial pressures in both experiments were $\sim 5.5 \times 10^{-19}$ and $\sim 2.9 \times 10^{-7}$ atm, respectively, and the carbon activity was 0.070. Type 310 stainless steel specimens that were exposed for 25 h at 875°C in these two experiments were examined with SEM. X-ray images for the distribution of metallic elements and sulfur in the scale/alloy interface regions of the specimens were also obtained. Figures 45 and 46 show the specimen image and x-ray distribution of elements for the samples exposed in environments *without* steam and *with* steam, respectively. The figures show that the scales in both specimens are predominantly Cr-rich oxide and some internal sulfidation occurred. The thickness of the oxide layer is ~ 2 to 3 µm. Silicon enrichment at the scale/alloy interface is observed in both specimens. From these results, it can be concluded that steam is *not* an essential component to establish the corrosion behavior of an alloy as long as the same oxygen, sulfur, and carbon potentials are simulated by adjusting the relative amounts of different molecular gas species.

Task E -- Erosion Behavior of Materials in Coal-conversion Processes
       (W. J. Shack)

       To interpret and compare erosion data being generated in the field tests at Synthane and Bi-Gas with laboratory data, it is necessary to estimate the total flux of particles actually striking the wall. Similarly, when using experimental data to decide whether a specific material has adequate erosive-wear resistance in a particular application, knowledge of the flux of particles onto the material, their velocities, and the impingement angle is required. It is difficult to estimate these quantities in actual flow situations. During this quarter, some preliminary modeling studies were begun in order to study the dependence of the particle flux on the properties of the gas flow for geometries similar to the elbow in the Synthane main coal-feed line.

       A brief literature review of previous work in the two-phase flow of particles and gases was made. Much of this work (see, e.g., Refs. 14-17) is concerned with the calculation of quantities (pressure drops, saltation velocity, choking velocity, etc.) that are required for the overall design of pneumatic or hydraulic conveying systems and not with the detailed study of particle flow patterns necessary to determine erosive-wear patterns. A rather sophisticated treatment of particle-flow interactions is available for low Reynolds number flows (see, e.g., Ref. 18), but this theory is inapplicable to the high Reynolds number flows typically found in coal-gasification plants.

14

Similarly, models have been developed to describe the behavior of finely
dispersed gas-particle systems; these are useful in studies of air pollution[19]
and aerosol systems[20] but of little relevance to the flows encountered in coal-
gasification systems.

The problem of analyzing fluid-particle flows is greatly simplified
if it is assumed the particles do not affect the fluid-flow field but that
the fluid is responsible for the motion of the particle. This "one way"
coupling is in reality valid only if the particle loading is small, but may be
a useful approximation when analyzing local flow fields. This approach was
originally developed[21,22] to describe water droplet impact and icing of air-
craft, but was also used in Ref. 23 to study the interaction of particle-fluid
flow and erosive wear. Models have been developed that describe a genuine
"two way" particle-fluid interaction.[24,25] The formulation in Ref. 24 is es-
pecially effective, because it is amenable to numerical solution by the well-
known "tank and tube" approach developed by Spalding and co-workers.[26] Thus,
stable numerical solutions can be obtained even for large Reynolds numbers.
The model developed in Ref. 24 has been used to analyze the flow field in an
axial-inlet peripheral-discharge cyclone separator.[27]

Because of its simplicity, it was decided to first examine fluid-
particle interactions using the uncoupled particle-flow model. In this case,
the flow pattern is calculated ignoring the presence of the particles, and
the particle trajectories can then be calculated by considering the fluid
loadings on the particle. The equations of motion for the particle can be
written

$$m \frac{dV_x}{dt} = -\rho \frac{C_D A}{2} |\underset{\sim}{V} - \underset{\sim}{U}| (V_x - U_x) \qquad (1)$$

and

$$m \frac{dV_y}{dt} = -\rho \frac{C_D A}{2} |\underset{\sim}{V} - \underset{\sim}{U}| (V_y - U_y). \qquad (2)$$

Here V_x, V_y and U_x, U_y and the x,y components of the particle and fluid
velocities, respectively; m is the mass of the particle; ρ is the fluid
density; C_D is the drag coefficient for the particle; A is the projected area
of the particle; and $|\underset{\sim}{V} - \underset{\sim}{U}|$ is the absolute magnitude of the vector difference
between the particle velocity and the fluid velocity, where

$$|\underset{\sim}{V} - \underset{\sim}{U}| = \left[\left(V_x - U_x \right)^2 + \left(V_y - U_y \right)^2 \right]^{1/2}. \qquad (3)$$

The drag coefficient C_D is a function of the Reynolds Number R

$$R = \frac{\rho |\underset{\sim}{V} - \underset{\sim}{U}| d}{\mu}, \qquad (4)$$

where d is a typical particle diameter, and μ is the viscosity of the fluid. The drag coefficient can then be calculated from the empirical relation

$$C_D = 24(1 + 0.197R^{0.63} + 0.00026R^{1.38})/R \qquad (5)$$

given in Ref. 22. From eqs. (1)-(5), it can be shown that the characteristic "lag" time, i.e., the time it takes for a particle placed in a fluid stream to acquire the fluid velocity, is

$$t_L = \frac{1}{18}(\rho_p d^2)/\mu, \qquad (6)$$

where ρ_p is the density of the particle. This can be compared with the transit time t_T for fluid particles. For example, for an elbow,

$$t_T = \pi r/4U_o, \qquad (7)$$

where r is the radius of the elbow, and U_o is a typical fluid velocity. The ratio of these two times yields a dimensionless group (an "erosion number")

$$E = t_T/t_L = (9\pi\mu r)/(\rho_d U_o d^2), \qquad (8)$$

which can be used to characterize the fraction of the fluid particles that impact onto the wall. If E >> 1, little particle impact and scour occurs; if E << 1, virtually all the particles carried by the fluid stream will impact the wall. Unfortunately, it is impossible to obtain explicitly the function f(E), which describes the fraction of particles scouring the wall in terms of E. However, by actually carrying out the numerical calculations, it should be possible to develop simple equations for f(E) for some practical geometries such as the 90° elbow and the 45° sweepline geometry. Such design formulas will be presented in the next quarterly.

The effect of particle size on the fraction is illustrated by the particle trajectories shown in Fig. 47a-c, which were calculated by numerical integration of Eqs. (1) and (2). The flow conditions and geometry are similar to those in the Synthane main coal-feed line. The particle diameters are 10 μ (Fig. 47a), 100 μ (Fig. 47b), and 1000 μ (Fig. 47c). The influence of particle size on the fraction of particles actually impacting the pipe wall is readily apparent.

In the next quarter, (a) more extensive calculations will be carried out to develop simple formulas for use by designers to estimate the fraction of the particles actually striking the pipe walls, (b) the fluid-particle model will be coupled with the erosive-wear equations developed in Ref. 4 to predict the wear patterns for the Synthane and Bi-Gas main coal field lines, and (c)

16

work will begin on a more sophisticated fully coupled fluid-particle model that can be used to check the validity of the simpler analyses and to analyze more complicated flow situations such as the "blocked-tee" geometry utilized at Bi-Gas.

Task F -- Component Performance and Failure Analysis *(S. Danyluk, G. M. Dragel, and M. D. Gorman)*

The activity during the quarter involved the examination of components from the Morgantown Energy Research Center high-pressure gas producer (rabble arm), the HYGAS pilot plant (alonized coupons), and the Synthane pilot plant (steam line). Final reports summarizing the results of the investigations of these components will be issued in the coming quarter. A summary of these analyses is given below. Three final reports have been issued: "EBV Ball-valve Stem Failure -- Synthane Coal-gasification Pilot Plant," "Analysis of the Gate-Valve Failure -- Grand Forks Energy Research Center Fixed-bed Slagging Gasifier Pilot Plant," and "Failure Analysis of the Thermocouple Assembly in the HYGAS Coal Pretreatment Vessel."

1. Analysis of Cracks in the ERDA-MERC Rabble Arm

A vertical water-cooled stirrer and rabble arm from the Energy Research and Development Administration -- Morgantown Energy Research Center (ERDA-MERC) developed cracks at weld fusion lines and at the OD of the carbon steel pipe that is used in the stirrer construction. A schematic of the stirred-bed gasifier is shown in Fig. 48. The stirrer (agitator) is rotated and moved up and down to mix air, steam, and coal and to minimize ash and coal agglomeration. A schematic of the lowest section of the rabble arm is shown in Fig. 49. The arm is assembled by welding carbon steel pipe and fitting it to the central shaft.

Cracks developed because of stress corrosion and possibly crevice corrosion. The corrosion scale cracked, detached from the base metal, and did not provide protection against subsequent attack. A series of photographs of an as-polished crack is shown in Fig. 50. These photographs show the cracked corrosion scale and the blunted crack tip representative of pitting corrosion. A series of photographs showing the electroetched crack morphology is shown in Fig. 51. The crack-tip morphology suggests corrosion attack. Electron-microprobe analysis showed that the corrosion scale was rich in sulfur, which probably participated in the corrosion process. Slag inclusions were observed in the weld metal but were not related to the cracking. The causes of the cracking are as follows: local surface inhomogeneities such as the heat-affected-zone next to the weld bead; loss of passivity due to mechanical rupture of the protective oxide coating; residual stresses due to weld shrinkage; and stresses induced at the OD of the rabble arm due to rotation.

A recommendation was made to change the construction design of the stirrer and not weld the pipes together. If welding is necessary, then the arm should be annealed to remove the welding residual stresses. Also, an austenitic stainless steel with a chromium content of >17% would resist the high-temperature corrosion better than the low-carbon steel.

2. Alonized Coupons from the HYGAS Pilot Plant

Coupons of alonized Type 316 stainless steel and Type 446 stainless steel were exposed to the HYGAS ash-agglomerating gasifier (AAG) environment for ∿0.13 Ms (36 h) and 1.04 Ms (288 h). The approximate bed temperature was 1038°C (1900°F) and the product gas composition was 31% CO, 7.7% CO_2, 15% H_2, and 46.3% N_2. The approximate sulfur content of the feed is 3% FMC char and 0.5% coke. The intent was to examine the effeciveness of alonizing in inhibiting corrosion. After removal from the gasifier, cross sections of the coupons were polished and examined by optical microscopy and with the electron microprobe to measure the extent of the penetration of corrosion scale. In addition, specimens were machined from the coupons and fractured in an ultra-high vacuum system and examined by Auger electron spectroscopy. These data are used to examine the extent of grain-boundary penetration by sulfides, grain-boundary segregation, and the effects of sulfur on grain-boundary embrittlement. The samples that were fractured in the Auger spectroscopy system were retrieved and subjected to scanning-electron microscopy to determine the fracture mode and morphology of the fracture surface.

Optical photographs and electron microprobe data from the alonized Type 316 stainless steel are presented in Figs. 52 and 53. These data represent exposures of ∿0.13 Ms (sample removed after Run 61) and ∿1.04 Ms (sample removed after Run 67). The optical photographs in these two figures show the extent of corrosion product buildup as a function of exposure. Significantly, more penetration of the corrosion product has occurred in the sample that was exposed for a longer period of time. Also, grain-boundary penetration by sulfur has occurred. Electron microprobe data show that nickel is depleted and sulfur and aluminum are enriched at the OD surface of the coupons.

The results of exposing a Type 446 martensitic stainless steel for ∿0.13 Ms to the HYGAS gasifier environment are shown in Fig. 54. This steel was not alonized. The optical photograph shows the corrosion scale had not penetrated as deeply into the sample as had occurred in the alonized Type 316 stainless steel. The electron-microprobe data show that the corrosion scale is enriched in sulfur and some aluminum and silicon are also present. Iron is depleted from the scale except for a thin layer at the OD of the corrosion scale, and a slight enrichment of nickel was observed. Chromium is enriched in the corrosion scale, depleted from the base metal, and a gradient in chromium concentration was found, with the highest concentration being adjacent to the base metal.

The coupons were machined, notched, and inserted into a scanning Auger electron spectroscopy system. The geometry of the machined specimens is shown in Fig. 55. Care was taken to preserve one portion of the surface that had the corrosion scale. The samples were fractured in an ultrahigh vacuum environment, and the derivative Auger spectra (dN/dF) were recorded as a function of energy. The derivative Auger spectra taken from the center of the alonized Type 316 stainless steel specimen that was exposed for 1.04 Ms and from the corrosion scale are shown in Figs. 56 and 57. The positive and negative excursions represent electron transitions and are used to identify the chemical makeup of the top monolayers of surface atoms. Figure 56 shows that chromium, iron, nickel, and a carbide comprise the central region of the fracture surface. Figure 57 shows that sulfur, carbon, oxygen, and aluminum compose the corrosion scale. Similar results were obtained on the Type 446 stainless steel.

The samples were retrieved and subjected to SEM investigation to determine the mode of fracture. Figure 58 shows a series of photographs of the Type 316 stainless steel. The photograph with the lowest magnification shows that the fracture mode is intergranular, and the successive photographs show one grain from which the Auger spectra were recorded. An oxide scale is observed. A higher magnification photograph of the corrosion scale and the interface between the corrosion scale and base metal is shown in Fig. 59. The morphology of these two regions is different.

SEM photographs of fractured Type 446 stainless steel are shown in Fig. 60. The fracture mode was transgranular brittle-cleavage fracture. Cleavage steps are readily seen on the higher magnification micrographs.

Another SEM micrograph showing the corrosion scale and the interface between the scale and base metal is shown in Fig. 61. The transgranular nature of the fracture surface is again readily visible.

3. Ballooned Pipe from the Synthane Pilot Plant

A 10.16-cm (4-in.) ID Schedule 40 carbon-molybdenum steel pipe was ballooned on the elbow side of a 5.08-cm (2-in.) letdown valve PCV-338. The piping carries steam at 404°C (760°F) and 4.8 MPa (700 psi). A partial schematic of the piping showing the elbow, bulged pipe, and letdown valve is shown in Fig. 62. Steam on the up side of the letdown valve is at 421°C (790°F) and 7.9 MPa. The cause for the bulging has not been determined. The following preliminary data has been accumulated:

(a) The maximum stresses in the pipe, assuming the stress can be calculated using $\sigma = Pr/t$, range from 44-72 MPa (6400-10,500 psi), but the handbook values of yield stress are 207 MPa (30 ksi) with a tensile strength of 448 MPa (65 ksi) at 427°C (800°F). The calculated stresses are much lower than the handbook values.

(b) The pipe OD diameter increased from 11.28 (4.44-in.) to 11.68 cm (4.60-in.).

(c) A chemical analysis of the pipe showed the following concentrations (wt%): total carbon 0.11-0.10, chromium 1.26, molybdenum 0.43, sulfur 0.012, nickel 0.08, and manganese 0.47.

Hardness testing, tensile testing, and optical and SEM analyses will be performed in the coming quarter.

REFERENCES

1. Materials Science Division Coal Technology Fifth Quarterly Report, October–December, 1975, Argonne National Laboratory, ANL-76-22.

2. Materials Science Division Coal Technology Seventh Quarterly Report, April–June, 1976, Argonne National Laboratory, ANL-76-111.

3. Materials Science Division Coal Technology Eighth Quarterly Report, July–September, 1976, Argonne National Laboratory, ANL-76-125.

4. Materials Science Division Coal Technology Ninth Quarterly Report, October–December, 1976, Argonne National Laboratory, ANL-77-5.

5. Materials Science Division Coal Technology Sixth Quarterly Report, January–March, 1976, Argonne National Laboratory, ANL-76-60.

6. J. G. A. Bitter, Wear 6, 169-190 (1963).

7. W. P. Orchard, HYGAS, to W. A. Ellingson, private communication (October 1976).

8. G. C. Robinson, C. R. Reese, and E. A. La Roche, Jr., "Determination of Thermally Induced Acoustic Emissions of Ceramics," Amer. Ceram. Bull., 53, 482-485 and 488 (1974).

9. M. Arrington, and B. M. Evans, "Acoustic Emission Testing of High Alumina Cement Concrete," NDT International, 10(2), 81-87 (April 1977).

10. J. J. Schuldies, "The Acoustic Emission Response of Mechanically Stressed Ceramics,: Mater. Eval., Vol. XXXI(10), 209-213 (1973).

11. J. F. Gardner, MERC, to W. J. Shack, personal communication (March 1977).

12. A. J. MacNab, Workshop on Materials Problems and Research Opportunities in Coal Conversion, Vol. II, Ohio State University, Columbus, Ohio, 1974, p. 33.

13. K. Natesan and O. K. Chopra, "Corrosion Behavior of Materials for Coal-gasification Applications," Proc. Symp. on Properties of High Temperature Alloys, The Electrochemical Society, Princeton, New Jersey, 77-1, 493-510 (1977).

14. F. A. Zenz and D. F. Othmar, Fluidization and Fluid Particle Systems, Reinhold, 1960.

15. R. G. Boothroyd, Flowing Gas-solids Suspensions, Chapman and Hall, London, 1971.

16. H. E. Rose and R. A. Duckworth, "Transport of Solid Particles in Liquids and Gases," The Engineer, 227(5903,5904,5905), 392-396, 430-433, and 478-483, (March 14, 21, 28, 1969).

17. W. Yang and D. L. Keairns, "Estimating the Acceleration Pressure Drop and the Particle Acceleration Length in Vertical and Horizontal Pneumatic Transport Lines," Pneumontransport 3, Third International Conference on the Pneumatic Transport of Solids in Pipes, University of Bath, U.K., April 7-9, 1976.

18. R. G. Cox and S. G. Mason, "Suspended Particles in Fluid Flow through Tubes " Annual Review of Fluid Mechanis, 3, 291-317 (1971).

19. J. A. Fay, "Buoyant Plumes and Wakes," Annual Review of Fluid Mechanics, 5, 151-160 (1972).

20. G. M. Hidy and J. R. Brock, *The Dynamics of Aerocolloidal Systems*, Pergamon, New York, 1970.

21. G. I. Taylor, "Notes on Possible Equipment and Techniques for Experiments on Icing of Aircraft," R&M 2024, ARC Tech. Rept. HMSO, London, 1940.

22. I. Langmuir and K. Blodgett, "Mathematical Investigation of Water Droplet Trajectories," U. S. Army Air Force Tech. Rept. 5418, 1946.

23. G. P. Tilly, "Erosion Caused by Airborne Particles," Wear, 14, 63-79 (1969).

24. A. Hamed and W. Tabakoff, "Numerical Method for Solution of Particulate Flow Equations," AIAA J., 13, 715-716 (1975).

25. C. T. Crowe and D. E. Stock, "A Computer Solution for Two-Dimensional Fluid-particle Flows," Int. J. For Num. Method in Eng., 10, 185-196 (1976).

26. A. D. Gosman, W. M. Pun, A. K. Runchal, D. B. Spalding, and M. Wolfstein, *Heat and Mass Transfer in Recirculating Flows*, Academic Press, New York, 1969.

27. C. T. Crowe and D. T. Pratt, "Analysis of the Flow Field in Cyclone Separators," Computers and Fluids, 2, 249-260 (1974).

TABLE I.   Initial Composition of Slag in
Corrosion Test Run 4

		Weight %	
Components		Initial	Corrected at 160 h
SiO_2	(S)	34	38
Al_2O_3	(A)	14.5	17
Fe_2O_3	(F)	22	11
CaO	(C)	21	24
MgO	(M)	5.1	6.0
Na_2O	(N)	1.3	1.5
K_2O	(K)	1.3	1.5
TiO_2	(T)	0.8	1.0
. . . .			
B/A Ratio[a]		1.03	0.79

[a] B/A = (F + C + M + N + K)/(S + A + T).

TABLE II. Coating Materials and Substrates Used in the
3.6 Ms Exposure to High-velocity Char at 980°C

Coating Materials	Substrates
Al_2O_3	Type 304 SS
	Incoloy 800
	Type 310 SS
$MgO-ZrO_2$	Type 304 SS
	Incoloy 800
	Type 310 SS
ZrO_2	Type 310 SS
Cr_2O_3	Type 310 SS
$Al_2O_3-Cr_2O_3$	Type 310 SS

TABLE III. Parameters Used in Heat-transfer Calculations

| Case | Cavity Size,[a] mm | | Thermal Conductivity, W/m-°K | | Convective Coefficient, W/-°K | Refractory Size, mm | Steel Shell Size, mm |
	Depth	Half Width	k_1	k_2			
1	6.5∿70 (6.5,13)	25-125 (50)	0.663	46.69	1.441	76 x 152	6.5 x 152
2	19.0∿70	25-125	0.663	46.69	2.882	76 x 152	6.5 x 152
3	19.0∿70	25-125	0.519	46.69	1.441	76 x 152	6.5 x 152
4	19.0∿70	25-125	0.519	46.69	2.882	76 x 152	6.5 x 152

[a]Numbers in parentheses represent spatial increments.

24

TABLE IV. Heating Schedules Followed for
Samples Examined This Quarter
(All Samples of KAOTAB)

1. Heat from room temperature to 120°C in 8 h

2. Furnace cool to room temperature

3. Heat from room temperature to 500°C in 8 h

4. Furnace cool to room temperature

5. Heat to 1000°C in 24 h

6. Furnace cool to room temperature

TABLE V. Acoustic-emission Measurements on the Top Cyclone
Lockhopper Valve

Valve-body Location	Noise Level, V	Structure-borne Signal and Noise, V
(a)	0.166	0.230
(b)	0.166	0.196
(c)	0.166	0.315
(d)	0.166	0.195
(e)	0.166	0.178
Nearby Structure (a)	0.166	0.171

TABLE VI. Acoustic-emission Measurements on the Top
Ash Lockhopper Valve

Valve-body Location	Noise Level, V	Structure-borne Signal and Noise, V
(a)	0.166	0.180-0.400
(b)	0.162	0.180-0.400
(c)	0.162	0.653
Nearby Structure		
(d)	0.163	0.180-0.500
(e)	0.163	0.220

TABLE VII. Acoustic-emission Measurements on the
Bottom Coal-feed Lockhopper Valve

Valve-body Location	Noise Level, V	Structure-borne Signal and Noise, V
175-kHz Transducer		
(a)	0.170	0.375-0.875
(b)	0.170	0.225-0.430
(c)	0.170	0.220-0.460
375-kHz Transducer		
(a)	0.153	0.186-0.480
(b)	0.152	0.153-0.186
(c)	0.152	0.153-0.350

TABLE VIII. Acoustic-emission Measurements on the North
Lower Petrocarb Feed Valve

Valve-body Location	Noise Level, V	Structure-borne Signal and Noise, V
175-kHz Transducer		
(a)	0.171-0.240	0.200
(b)	0.171-0.270	0.365
(c)	0.170-0.260	0.360
(d)	0.171-0.250	0.250
(e)	0.171-0.240	0.48
375-kHz Transducer		
(a)	0.154	0.154
(b)	0.154	0.174
(c)	0.154	0.155
(d)	0.154	0.161
(e)	0.154	0.174
750-kHz Transducer		
(a)	0.128	0.128
(b)	0.128	0.129
(c)	0.138	0.128
(d)	0.128	0.128
(e)	0.128	0.128

TABLE IX. Acoustic-emission Measurements on the South Lower Petrocarb Feed Valve and Nearby Structural Components

Valve-body Location	Noise Level, V	Structure-borne Signal and Noise, V
175-kHz Transducer		
(a)	0.4-1.0	1.2
(b)	0.4-1.0	2.8
(c)	0.4-1.0	4.3
(d)	0.4-1.0	1.3
(e)	0.4-1.0	1.3
375-kHz Transducer		
(a)	0.2-0.5	0.6
(b)	0.2-0.5	2.0
(c)	0.2-0.5	3.0
(d)	0.2-0.5	0.3
(e)	0.2-0.5	0.3
750-kHz Transducer		
(a)	0.128	0.128
(b)	0.128	0.133
(c)	0.128	0.580
(d)	0.128	0.135
(e)	0.128	0.130

TABLE X. Gas Environment Used for Preliminary
Corrosion Experiments at 875°C

Gas Species	Vol %
CO	11.7
CO_2	15.4
H_2	12.9
H_2O	48.9
H_2S	1.0
CH_4	10.0

. . . .

$$P_{O_2} = 3 \times 10^{-17} \text{ atm}$$

$$P_{S_2} = 1.0 \times 10^{-7} \text{ atm}$$

$$a_c = 0.008$$

TABLE XI. Chemical Composition (wt %) of Alloys in Corrosion Experiments

Alloy	Fe	Cr	Ni	C	S	Mn	Si	Other
Incoloy 800[a]	46.0	21	32.5	0.05	0.008	0.75	0.35	0.38 Al, 0.38 Ti
Inconel 671[a]	–	48	50	0.05	–	–	–	0.35 Ti
Type 310 SS[a]	Bal[b]	25	20	0.25	–	1.5	0.4	–
U. S. Steel Alloy[a]	Bal[b]	18.5	17.8	0.06	0.011	1.25	2.05	–
Type 304 SS	Bal[b]	19	10	0.06	–	1.5	0.4	–
RA 333	18	25	45	0.05	0.015	1.5	1.25	3.0 W, 3.0 Co, 3.0 Mo
Alloy 406	Bal[b]	13.1	0.36	0.11	0.007	0.44	0.46	4.48 Al
Iron	Bal[b]	–	–	0.012	0.025	0.017	–	–

[a]Will be preexposed to gas mixtures and subsequently tested in uniaxial tension.

[b]Bal indicates balance.

TABLE XII. Gas Compositions (vol %) Used in the Evaluation of Material Behavior at 750 and 875°C

Gas Species	750°C (No Steam)				875°C (No Steam)				875°C with steam
	1	2	3	4	1	2	3	4	
CO	28.4	15.5	5.1	1.0	16.4	8.6	5.9	1.53	18.4
CO_2	56.8	30.9	10.3	2.0	32.8	17.2	11.8	3.1	8.1
H_2	5.2	47.6	81.5	95.1	44.5	70.1	79.0	93.3	61.0
CH_4	9.5	5.2	1.7	0.33	5.5	2.9	2.0	0.51	2.9
H_2S	0.09	0.81	1.40	1.64	0.77	1.21	1.36	1.60	1.5
H_2O	–	–	–	–	–	–	–	–	8.6
P_{O_2} (atm)	1.0×10^{-20}	2.4×10^{-21}	4.1×10^{-22}	4.2×10^{-23}	1.9×10^{-18}	5.5×10^{-19}	2.4×10^{-19}	1.7×10^{-20}	5.4×10^{-19}
P_{S_2} (atm)	2.8×10^{-8}	2.7×10^{-8}	3.1×10^{-8}	2.9×10^{-8}	2.8×10^{-7}	2.9×10^{-7}	2.9×10^{-7}	2.7×10^{-7}	2.6×10^{-7}
a_c	0.25	0.348	0.348	0.20	0.056	0.070	0.076	0.082	0.070

Fig. 1. Top and Side Views of the New Bottom Section of the
Slag-corrosion Furnace. Dimensions are in inches. ANL
Neg. No. 306-77-47.
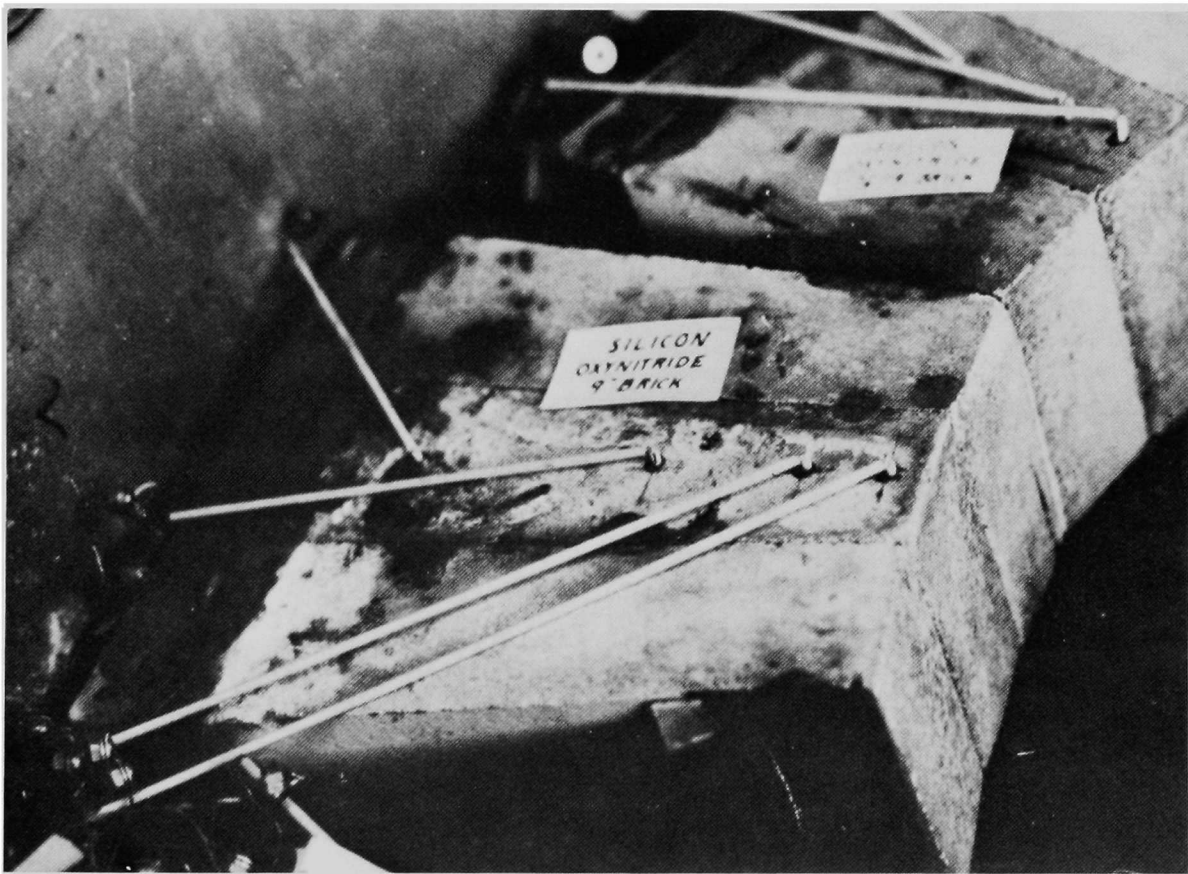
Fig. 2. Thermocouple Positions in a Full Length (228.6 mm) Brick.
Neg. No. MSD-64010.
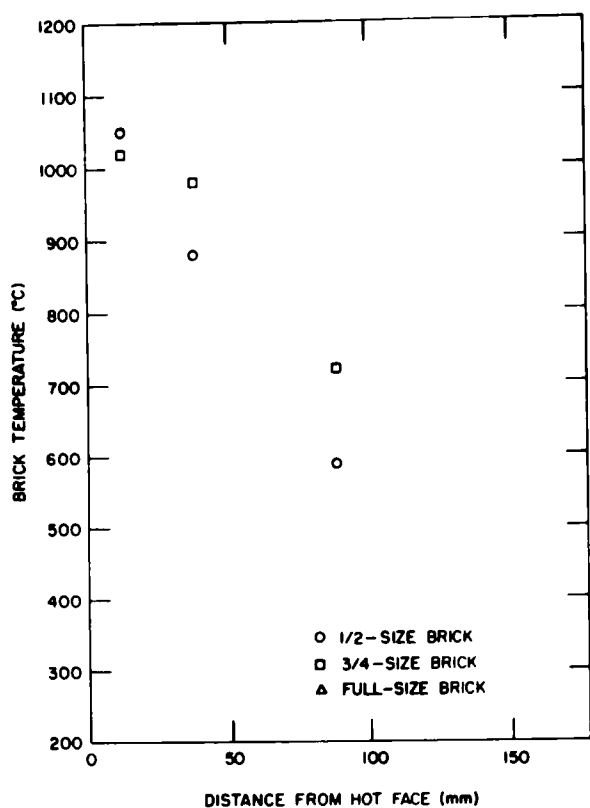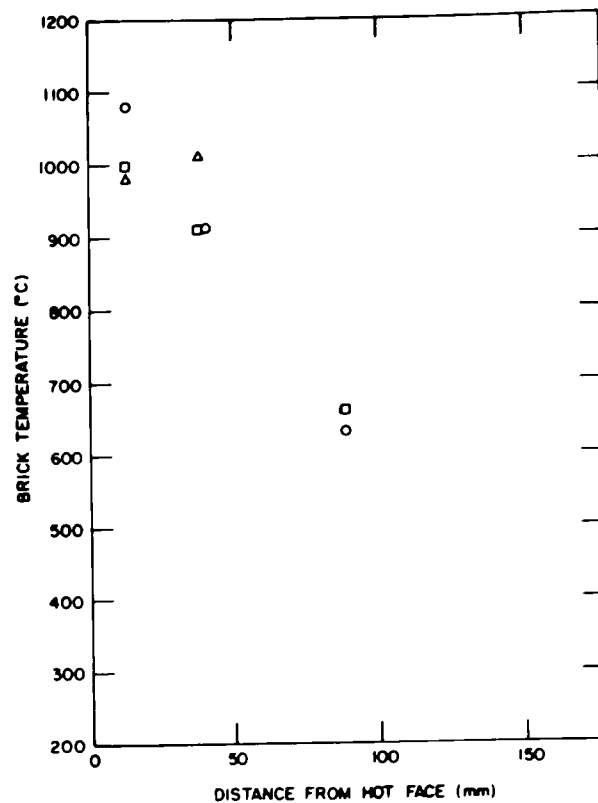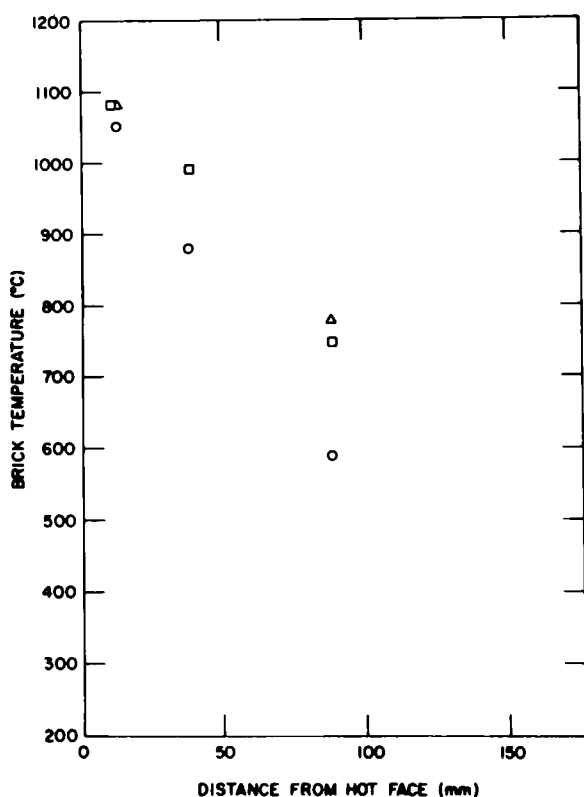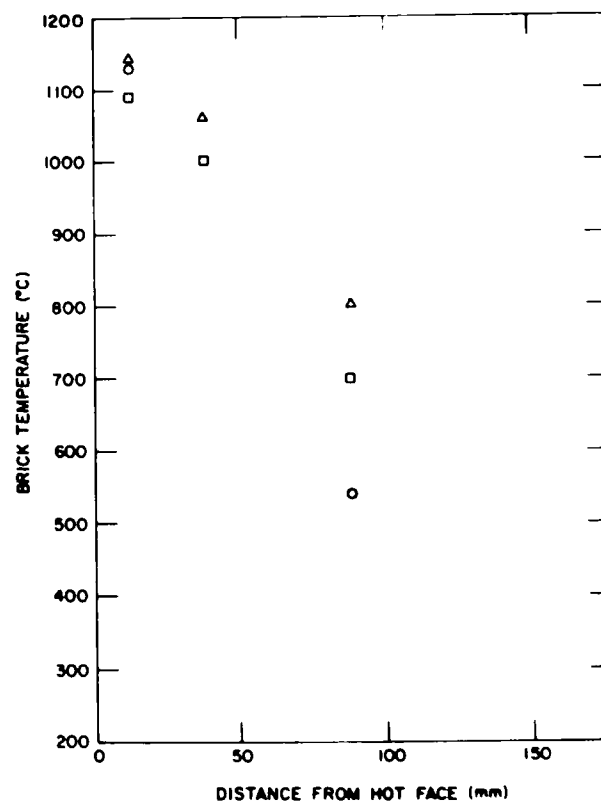
Fig. 3. Temperatures in Bricks at Beginning of Test at Four Locations in Full-
length Bricks and at Three Locations in 3/4- and 1/2-length Bricks. (Lack
of data points indicates thermocouple failed.) (a) Nitride-bonded silicon
carbide, (b) silicate-bonded silicon carbide, (c) oxynitride-bonded silicon
carbide, and (d) silicon oxynitride. ANL Neg. No. 306-77-277.

34
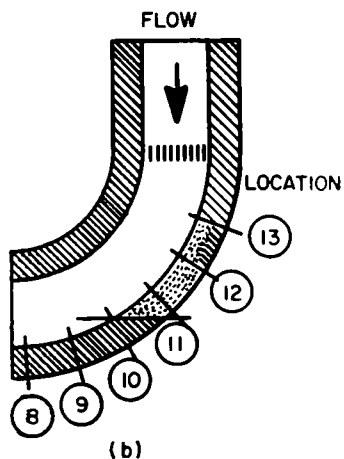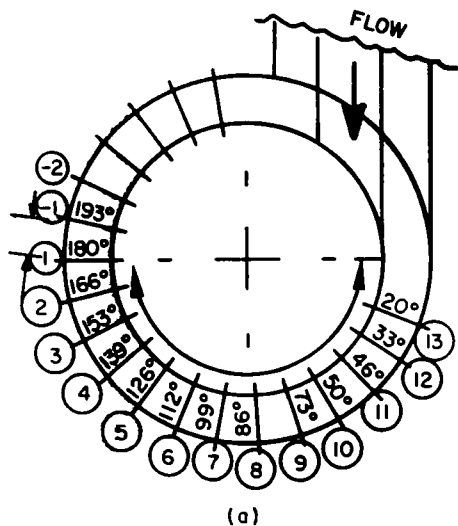
Fig. 4. (a) Azimuthal Distribution of Measurements Location along the Inlet Centerline of the HYGAS Cyclone and (b) Assumed Erosion Pattern Based on Elbow Studies. ANL Neg. No. 306-77-177.
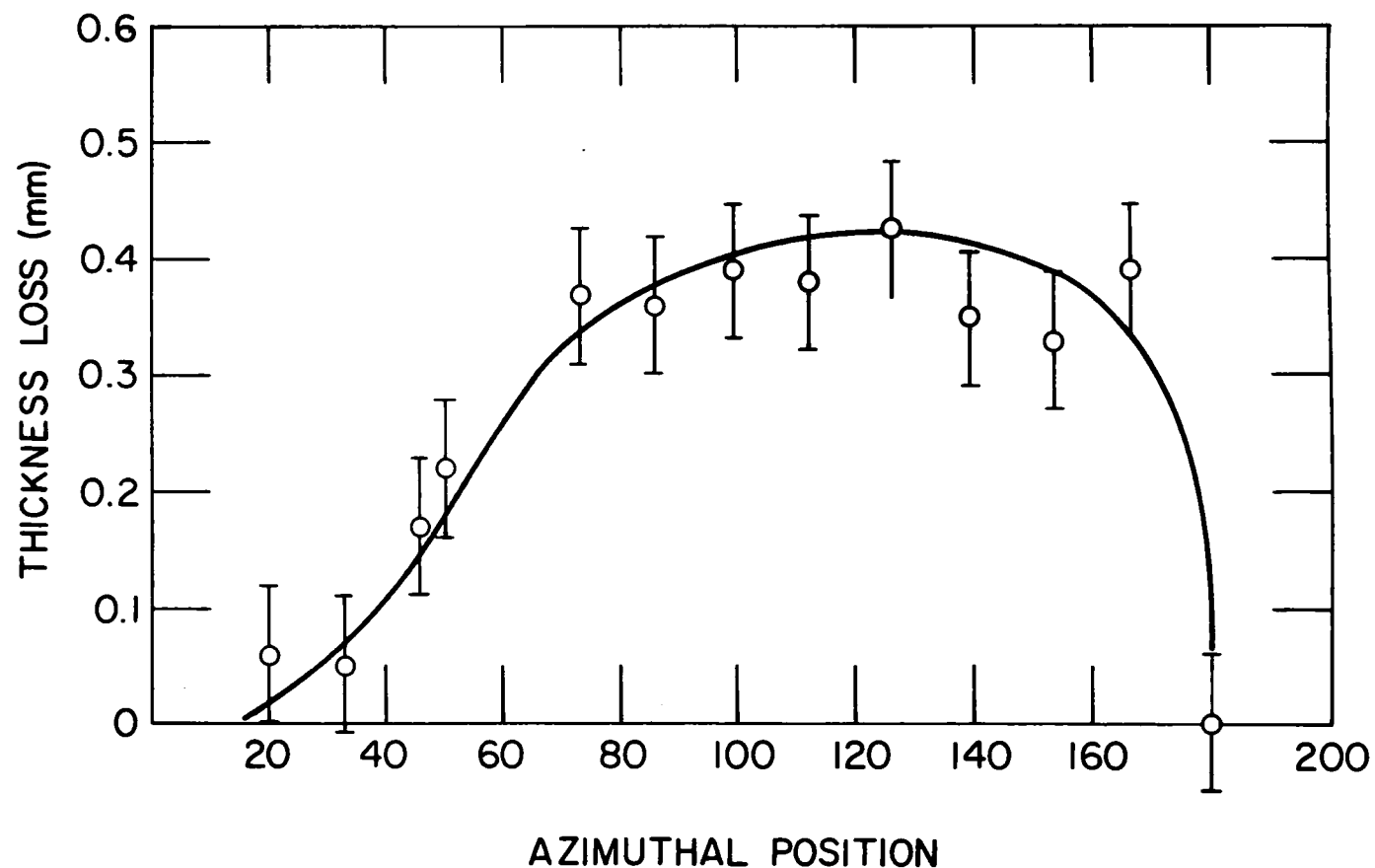
Fig. 5. Azimuthal Distribution of Wear along the Inlet Centerline of the HYGAS Cyclone. ANL Neg. No. 306-77-178.

35
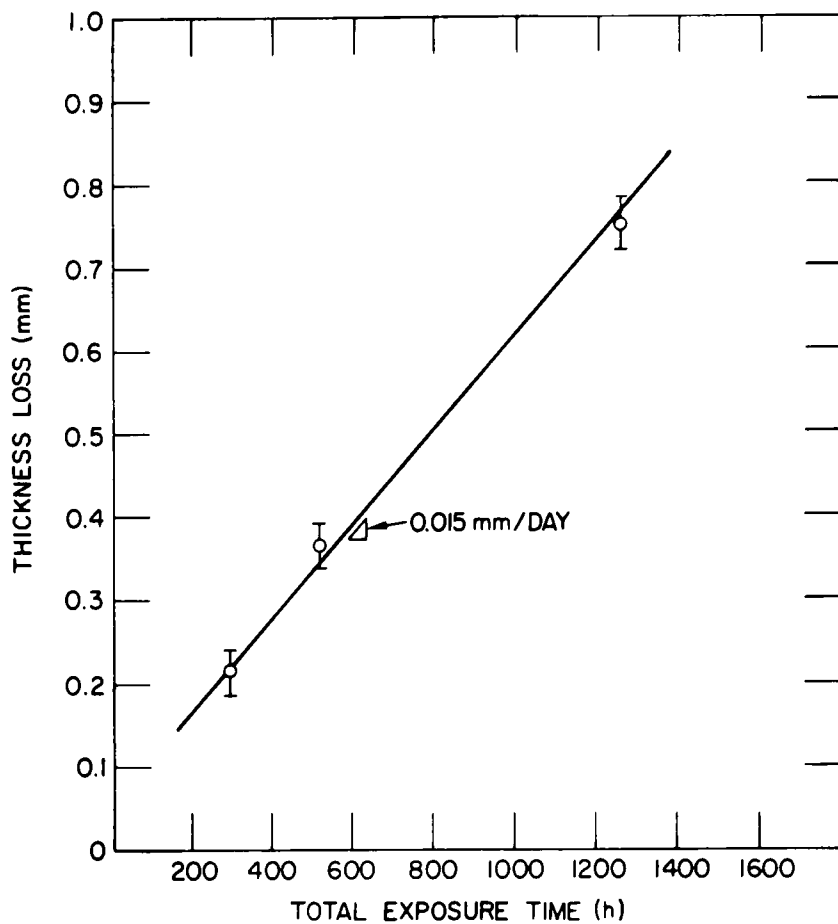
Fig. 6. Average Wear Rate along the Inlet Centerline of the HYGAS Cyclone as a Function of the Number of Hours of Operation. ANL Neg. No. 306-77-172.
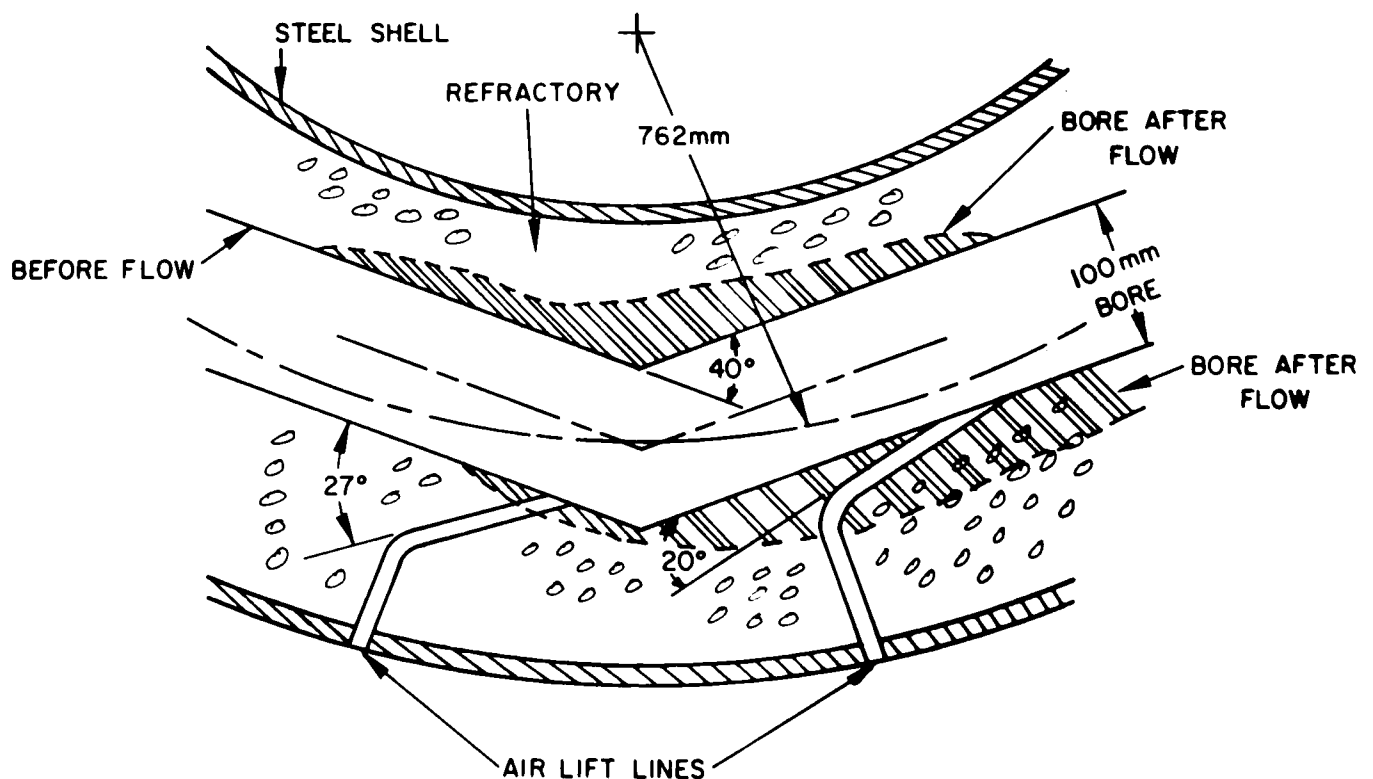
Fig. 7. Erosive Wear of Refractory-lined Transfer Line After 200-h Exposure. ANL Neg. No. 306-77-168.

Fig. 8. Schematic of the Ash 502 Direction Change Transfer Lines. ANL
Neg. No. 306-77-182.
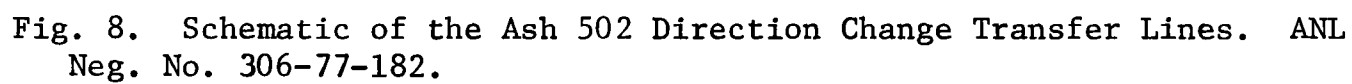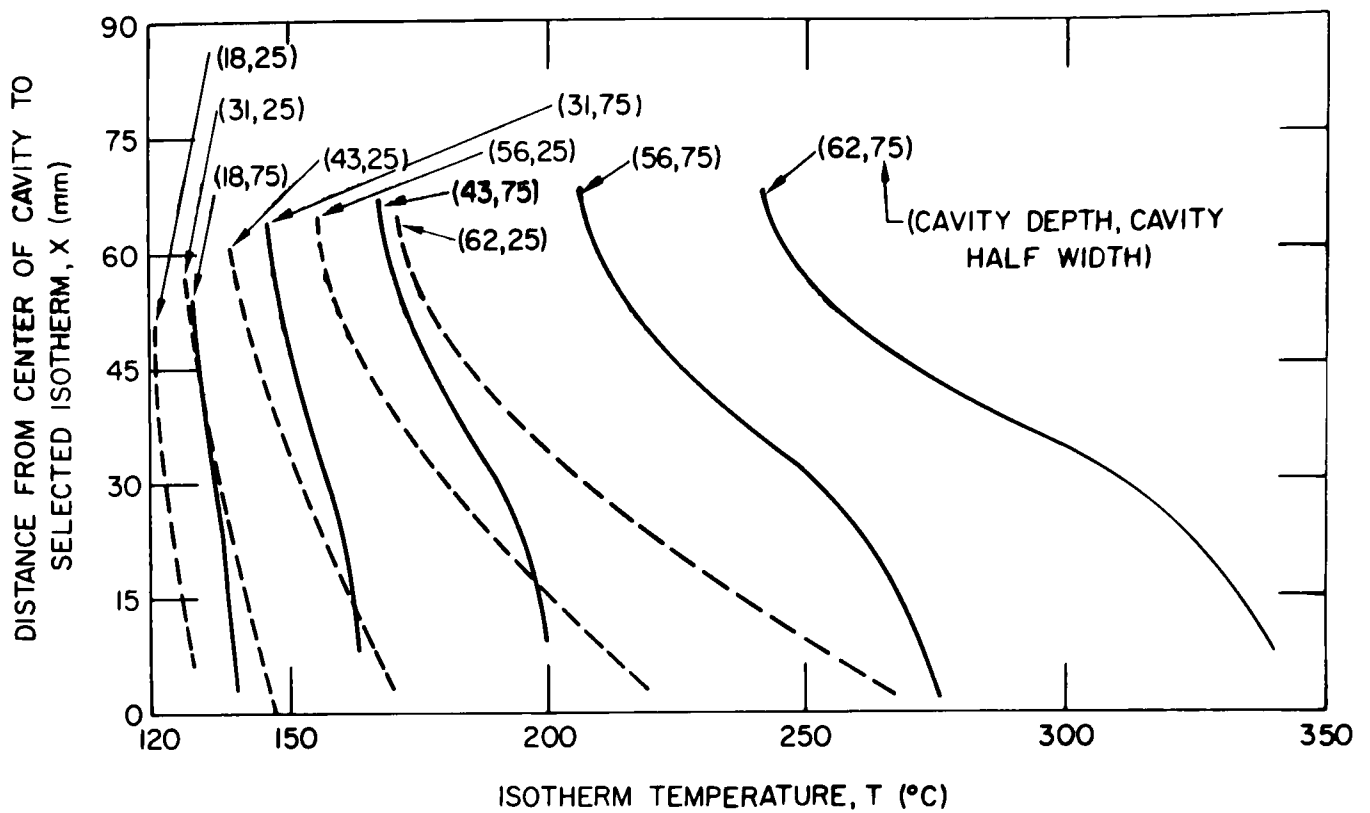
Fig. 9. Isothermal Distance from Center Line of a Synthesized Cavity in a 76-mm-thick Refractory Bonded to a 6.5-mm-thick Steel Plate. Dashed and solid lines indicate cavity half widths of 25 and 75 mm, respectively. ANL Neg. No. 306-77-173.
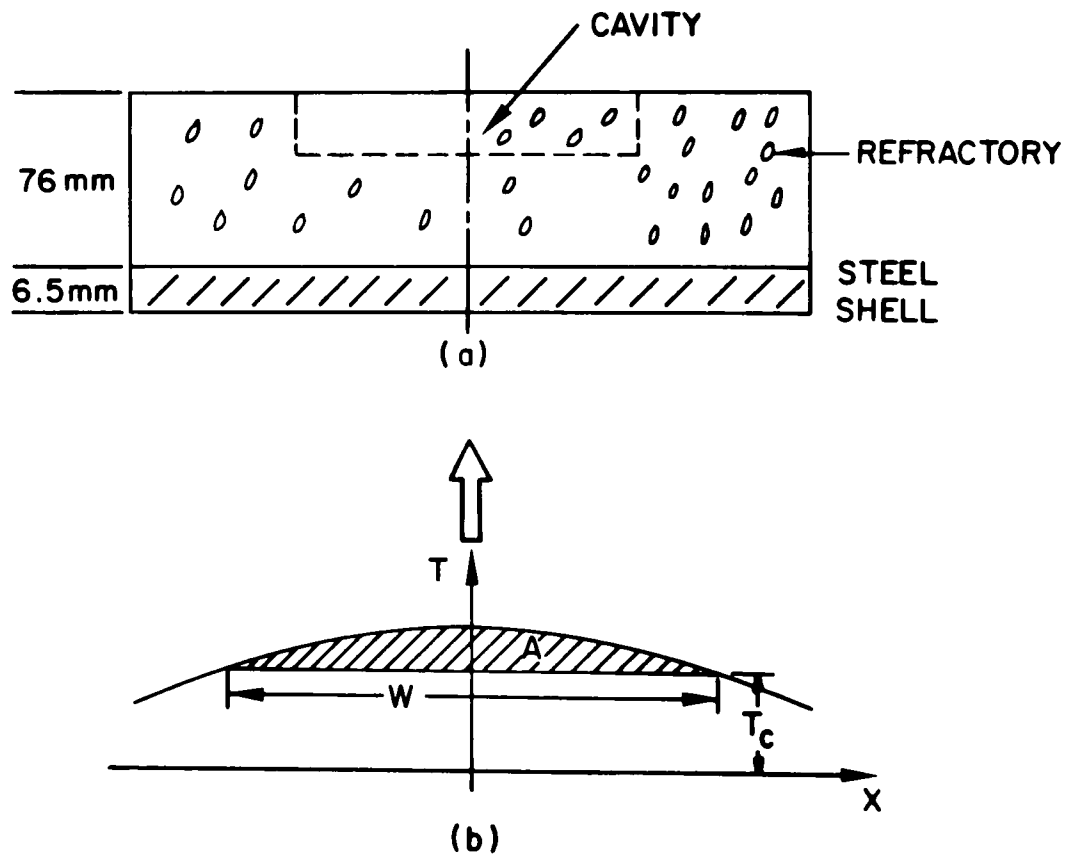
Fig. 10. Schematic of (a) Refractory-steel Lamination with Rectangular Cavity Defect and (b) Thermal Profile Observed in a Single Line Scan across the Cavity Defect. ANL Neg. No. 306-77-179.

38
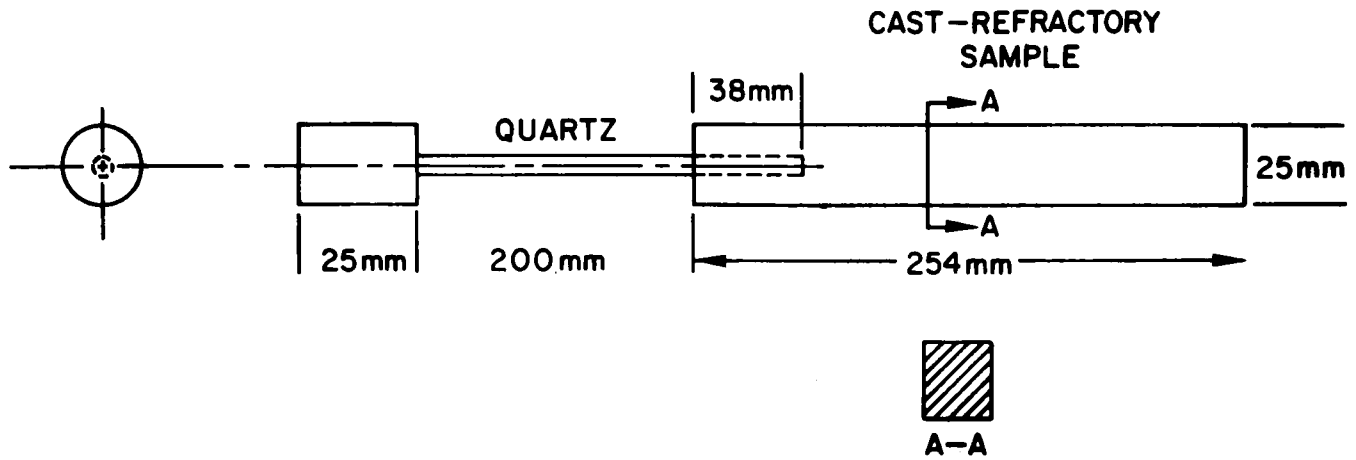
Fig. 11. Schematic of Sample and Embedded Acoustic Waveguide. ANL Neg. No. 306-77-169.
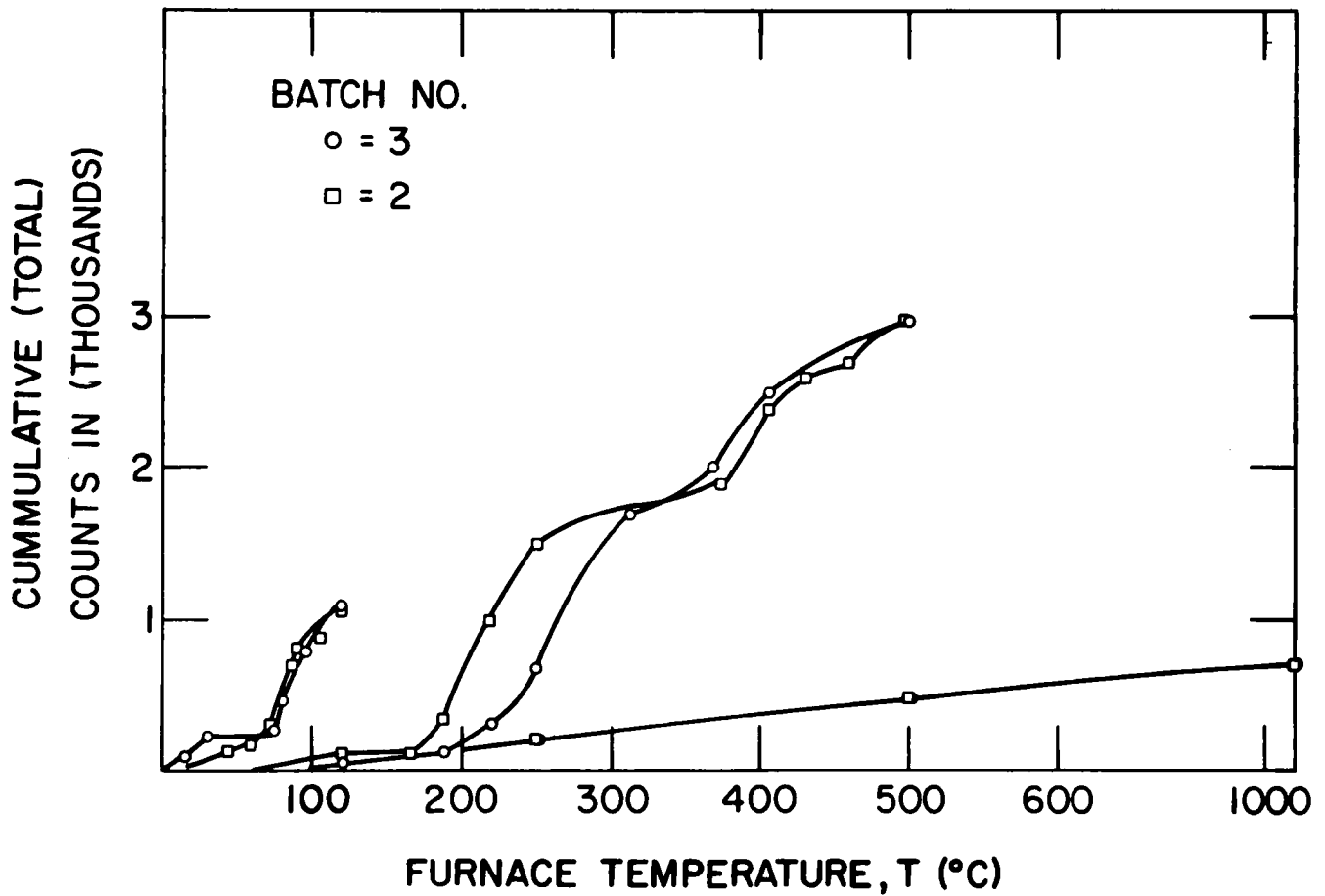
Fig. 12. Total Acoustic-emission Counts as a Function of Temperature for Three Heating Cycles on the Same Sample. ANL Neg. No. 306-77-181.
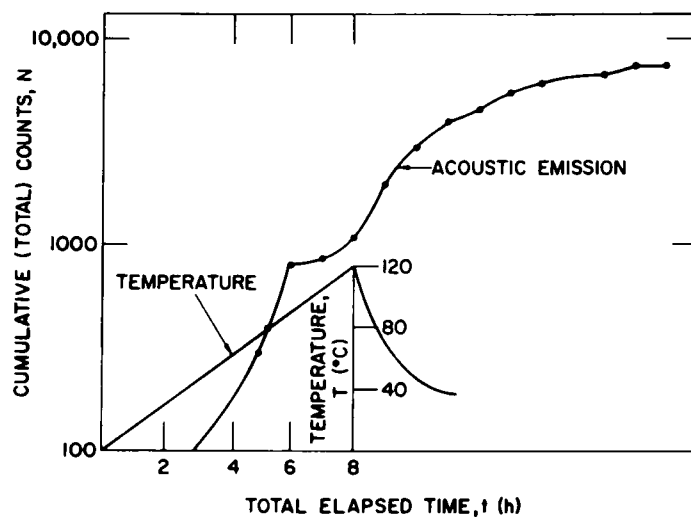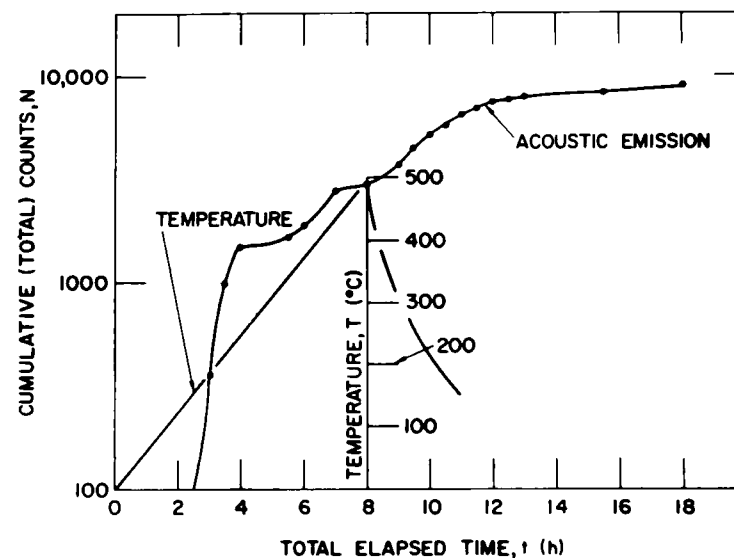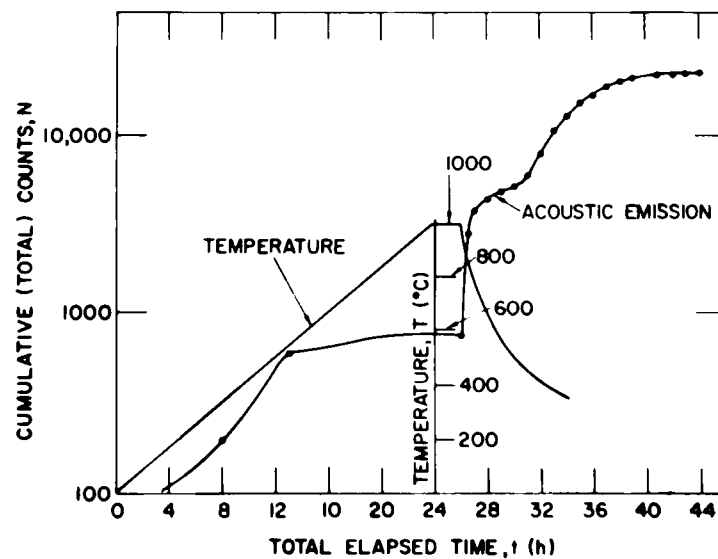
Fig. 13.   Total Acoustic-emission Counts as a Function of Time for (a) the 120°C
Linear Heating Ramp, (b) the 500°C Linear Heating Ramp, and (c) the 1000°C
Linear Heating Ramp, all with Furnace Cooling.   ANL Neg. No. 306-77-276.

TRANSVERSE SECTION

AXIAL SECTION
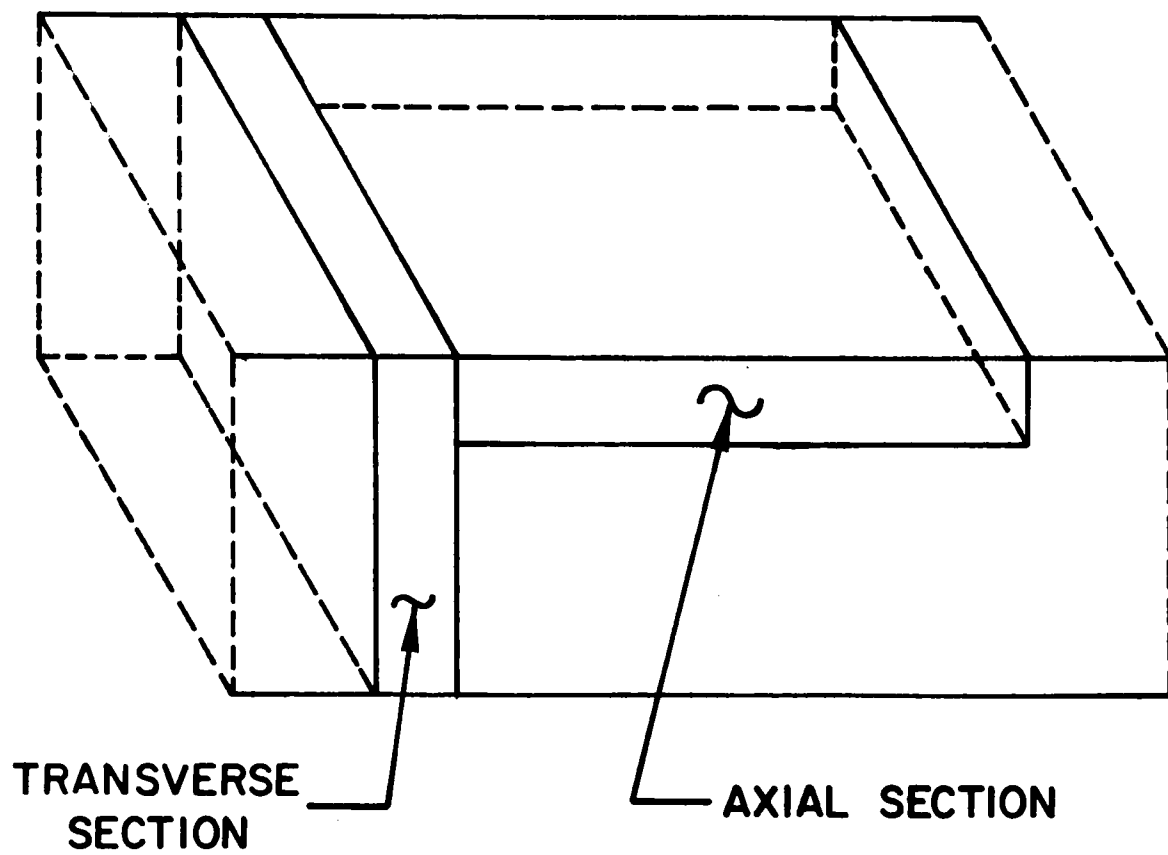
Fig. 14. Schematic Showing Metallographic Sample Locations. ANL Neg. No. 306-77-170.
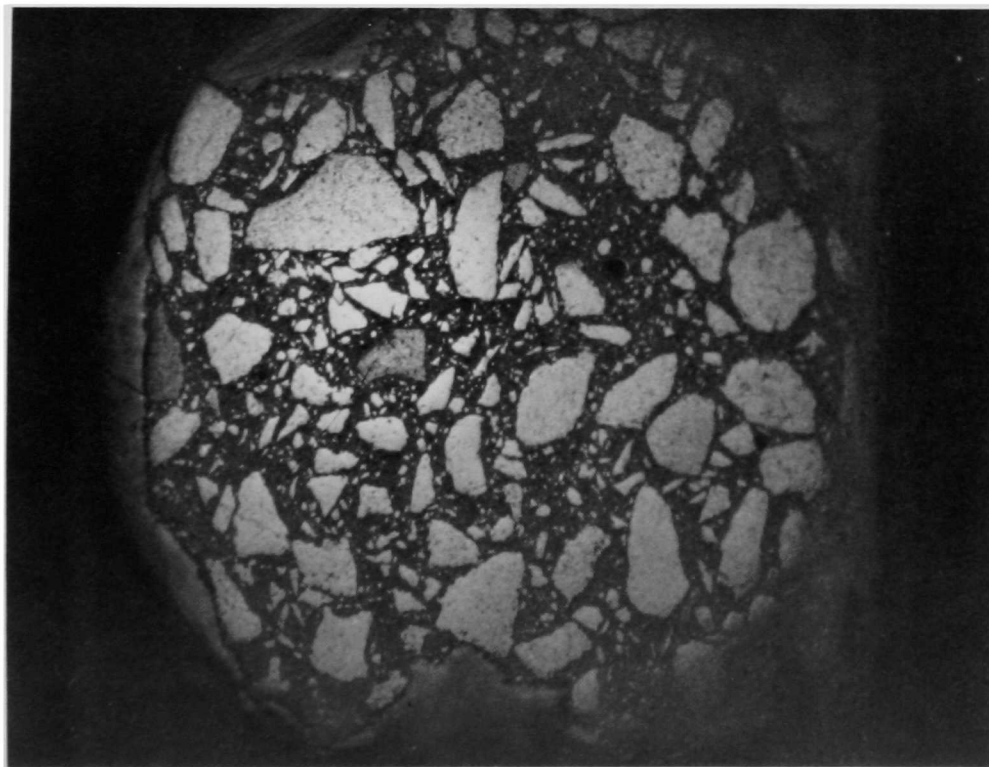
Fig. 15. Transverse Metallographic Sample. ANL Neg. No. 306-77-187.
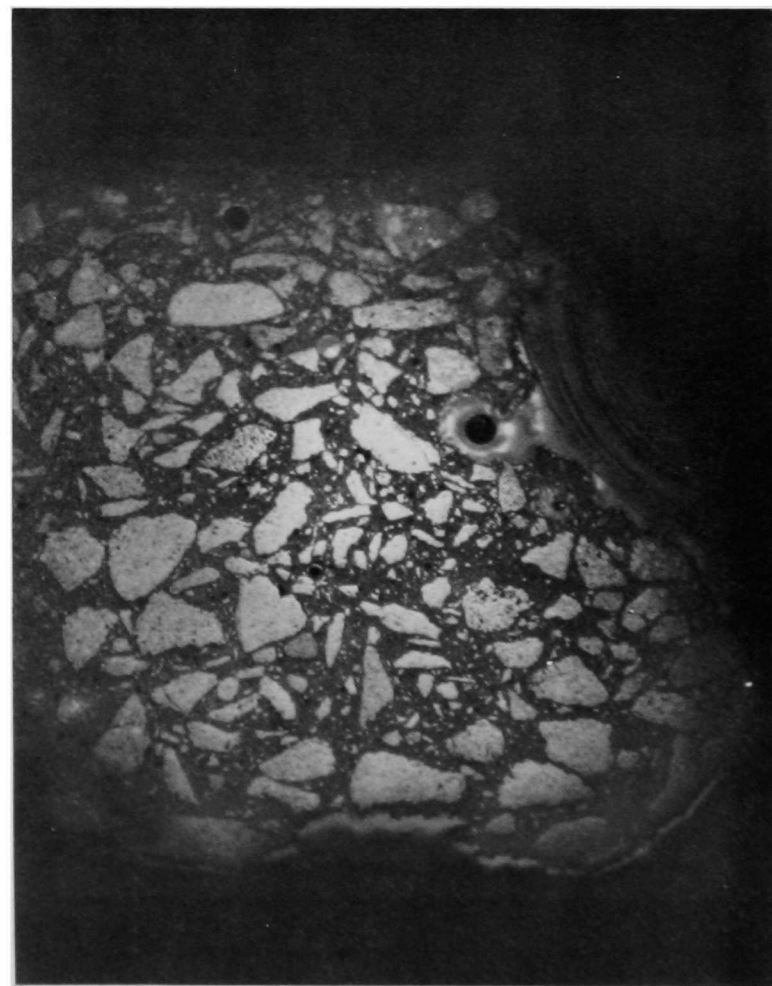
Fig. 16. Axial Metallographic Sample. ANL Neg. No. 306-77-186.
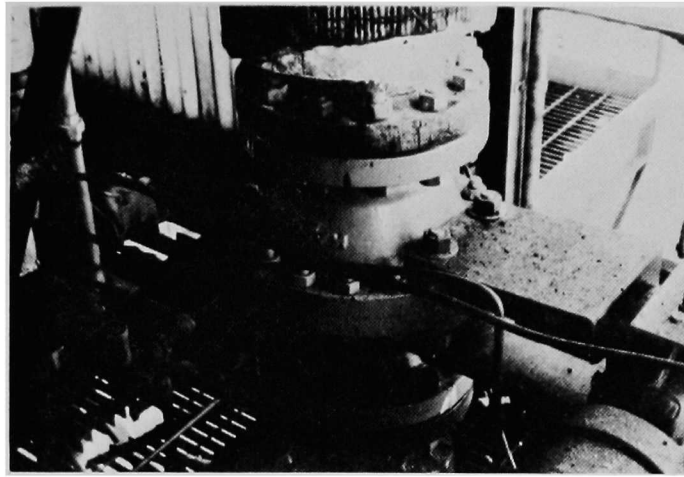
(a)
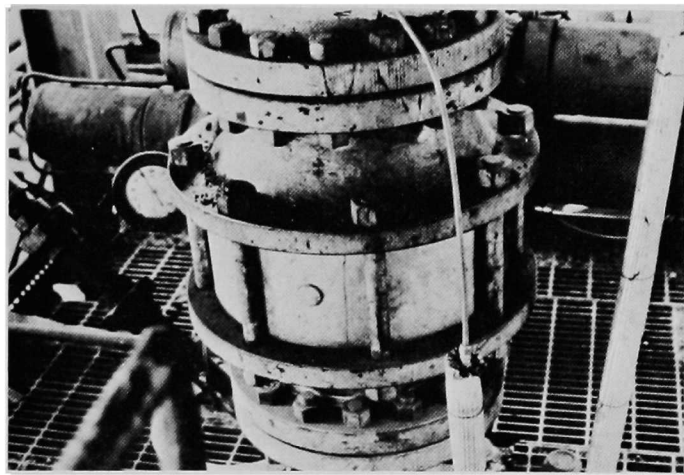
(b)

(c)

Fig. 17. Valves at MERC Low-Btu Gasifier.
  (a) Top cyclone lockhopper valve,
  (b) top ash lockhopper valve, and
  (c) north bottom coal-feed lockhopper
  valve. ANL Neg. No. 306-77-269.
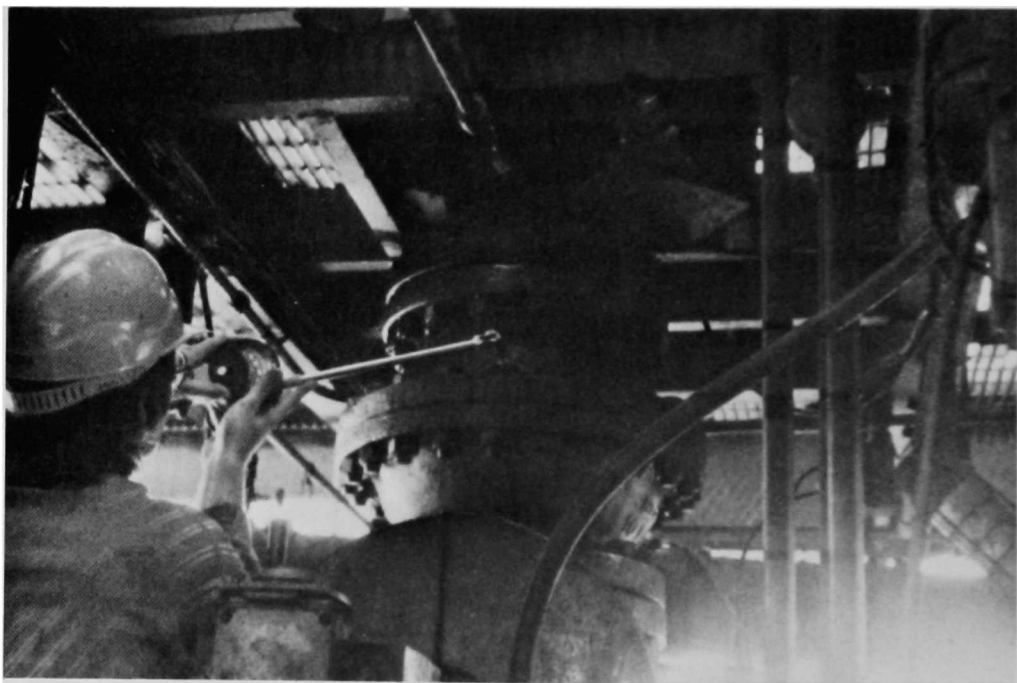
Fig. 18.   Measurement of Reference Temperatures Using a
    Contact Pyrometer.   ANL Neg. No. 306-77-185.
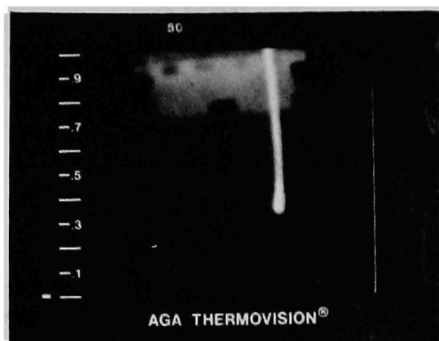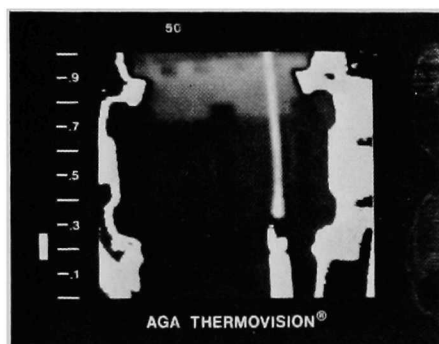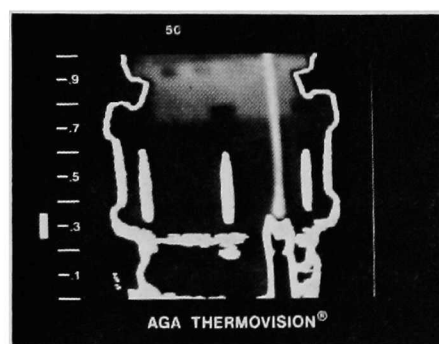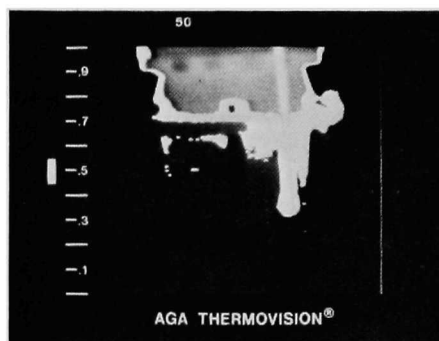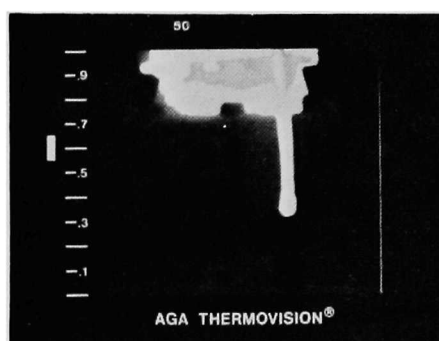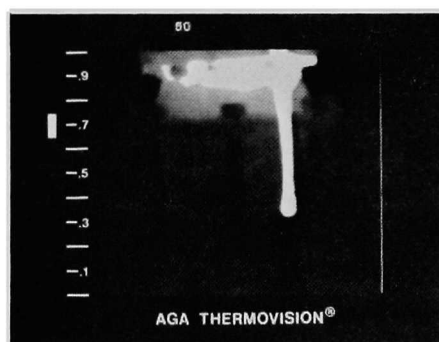
Fig. 19. Thermal Profile Sequence of the Top Ash Lockhopper
Valve (Thermovision Range = 50). (a) Thermal picture,
(b) T = 53°C isothermal area, (c) T = 55°C isothermal area,
(d) T = 57°C isothermal area, (e) T = 59°C isothermal area,
(f) T = 62°C isothermal area, and (g) T = 64°C Isothermal
area. ANL Neg. No. 306-77-270.
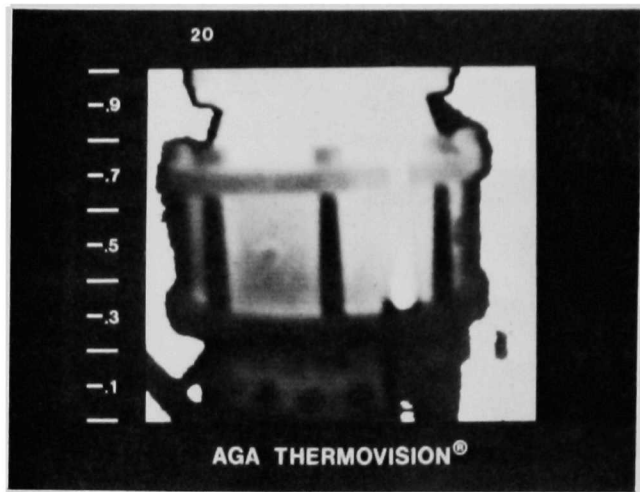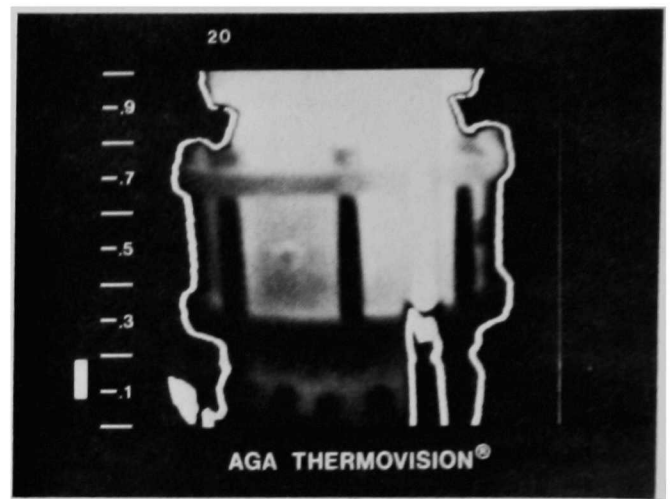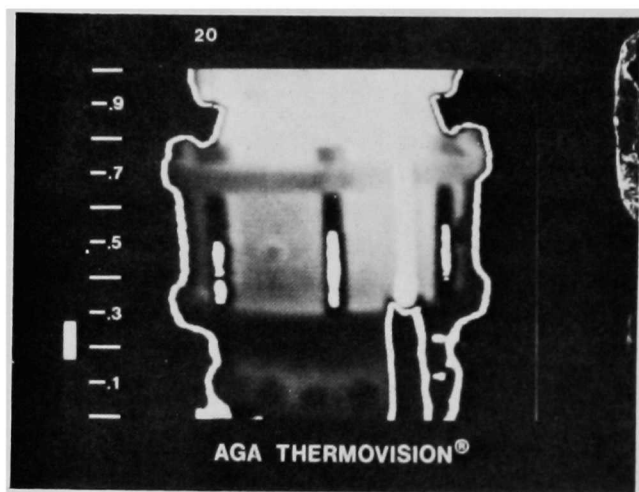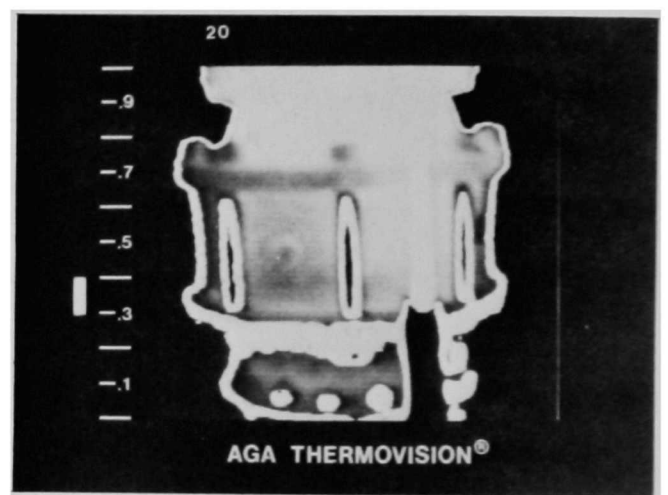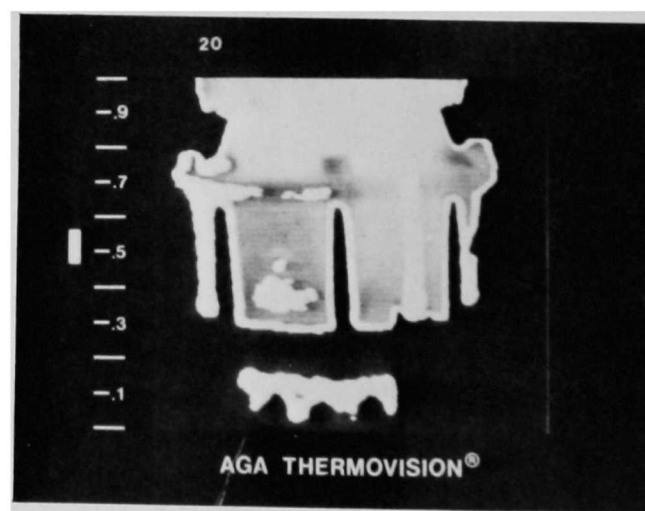
Fig. 20. Thermal Profile Sequence of the Top Ash Lockhopper Valve (Thermo-vision Range = 20). (a) Thermal picture, (b) T = 54°C isothermal area, (c) T = 55°C isothermal area, (d) T = 56°C isothermal area, and (e) T = 57°C isothermal area. ANL Neg. No. 306-77-272.
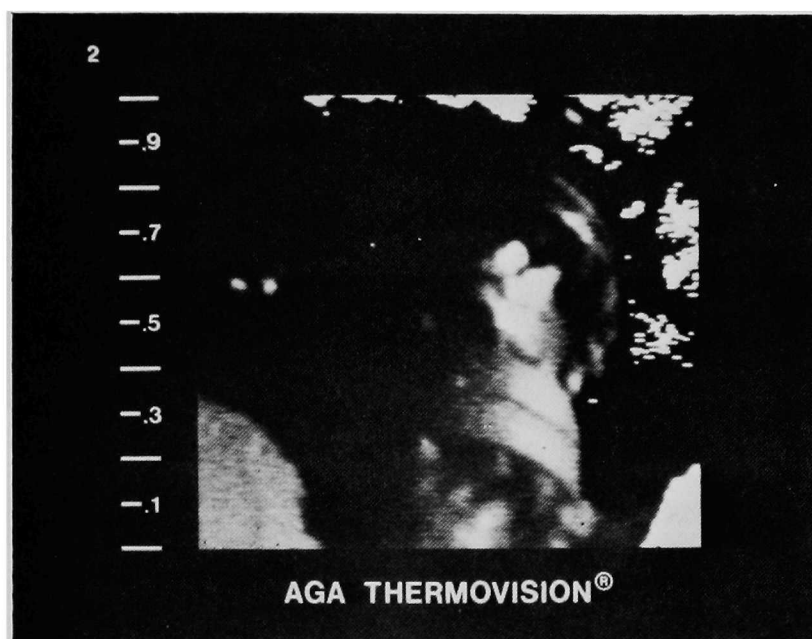
(a)
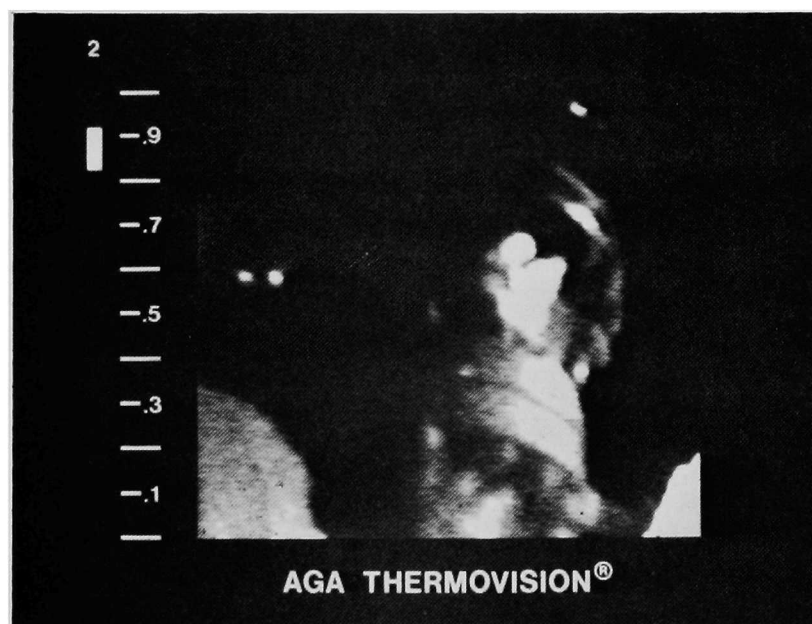
(b)

Fig. 21. Thermal Profile Sequence of the North
Bottom Coal-feed Lockhopper Valve. (a) Thermal
picture and (b) T = 37°C "hot spot." ANL Neg.
No. 306-77-268.
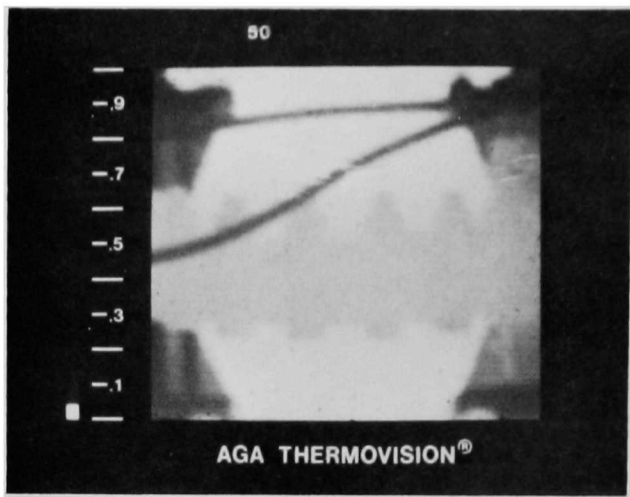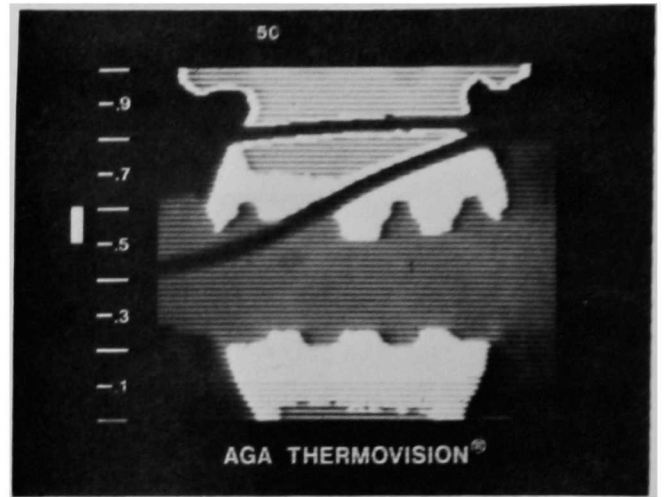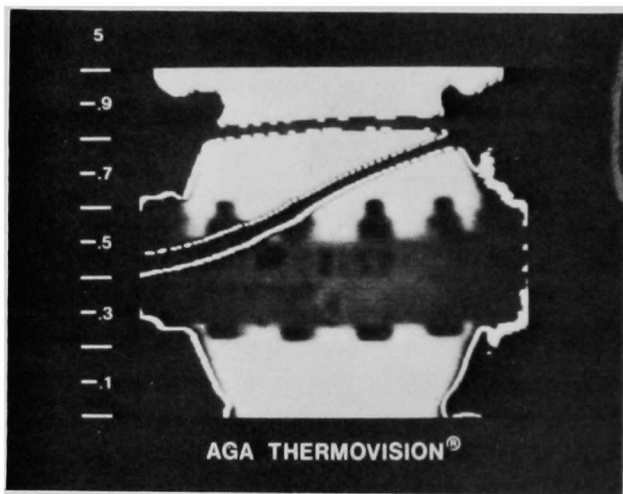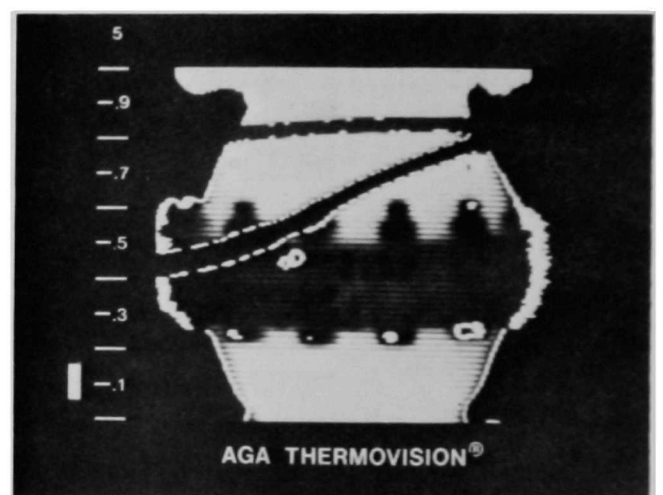
Fig. 22. Thermal Profile Sequence of Top Cyclone Lockhopper Valve. (a) Thermal picture (thermovision range = 50), (b) T = 60°C isothermal area, (c) thermal picture (thermovision range = 5), (d) T ≃ 58.5°C isothermal area, and (e) T = 59°C isothermal area. ANL Neg. No. 306-77-267.

(a)

(b)

(c)

(d)

(e)
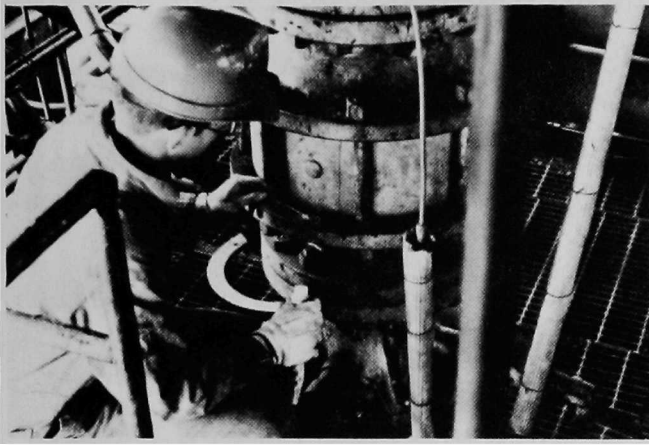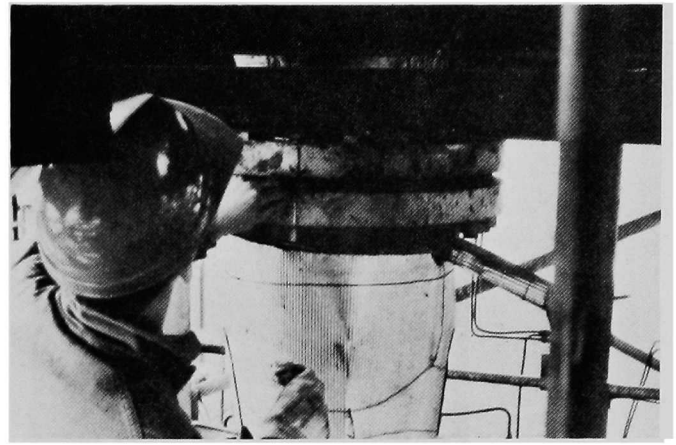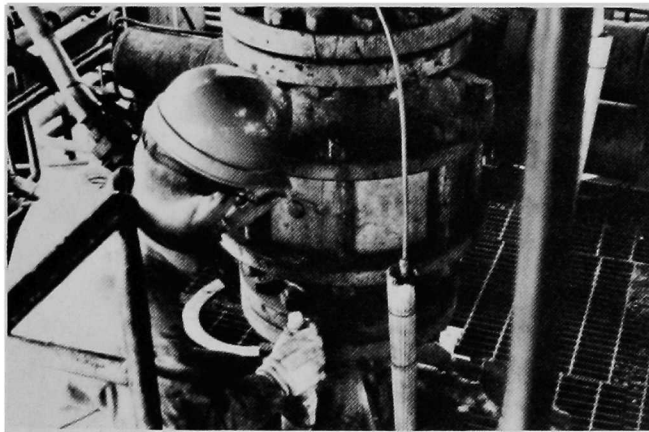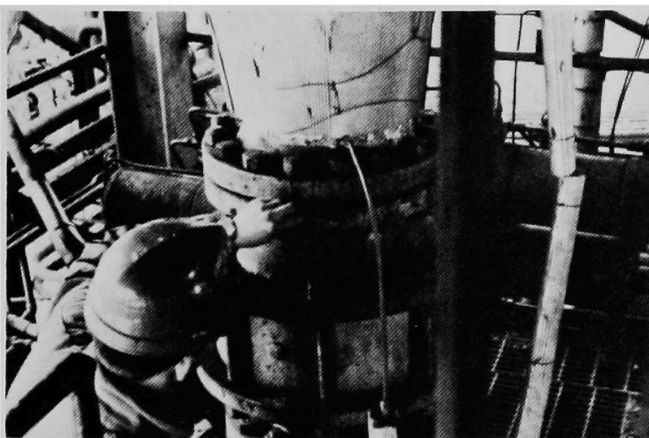
Fig. 23. Acoustic-emission Measurement Locations on the MERC Top Cyclone
Lockhopper Valve. ANL Neg. No. 306-77-265.
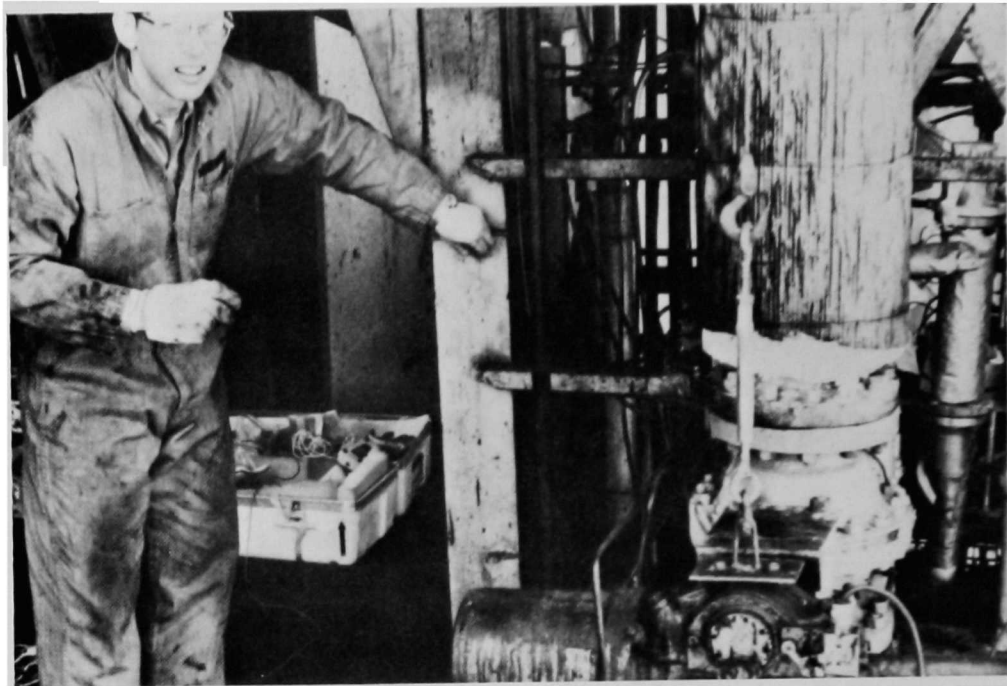
(a)
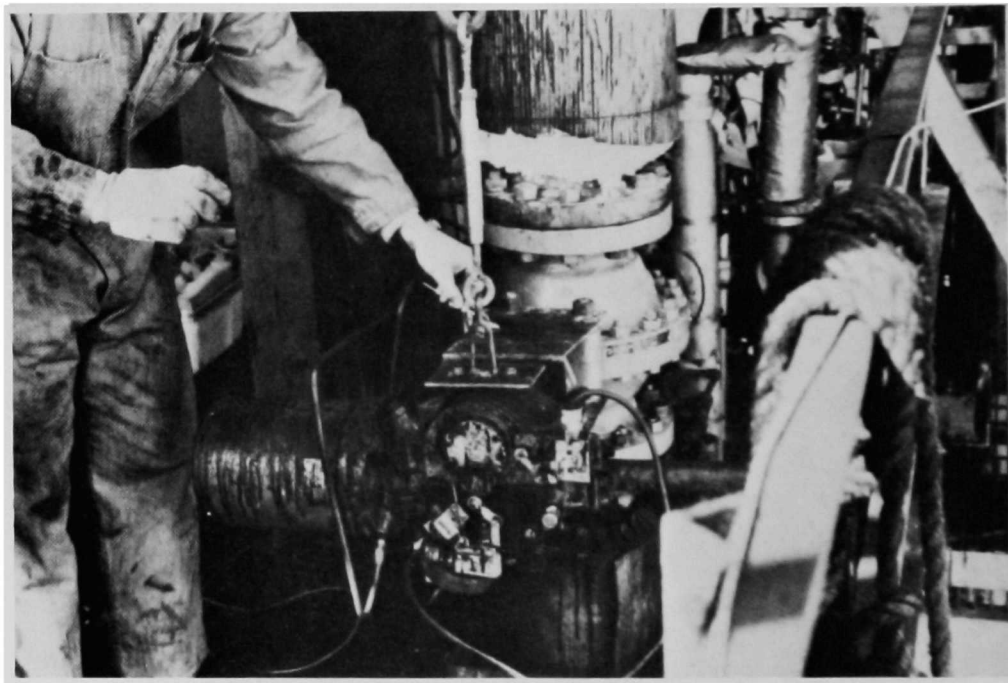
(b)

Fig. 24. Acoustic-emission Measurement Locations on Struc-
ture Near Cyclone Lockhopper Valve. ANL Neg. No. 306-77-
275.

(a)

(b)

(c)

(d)

(e)
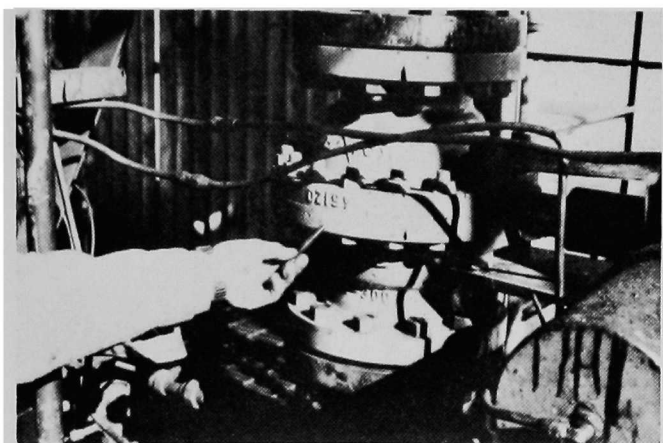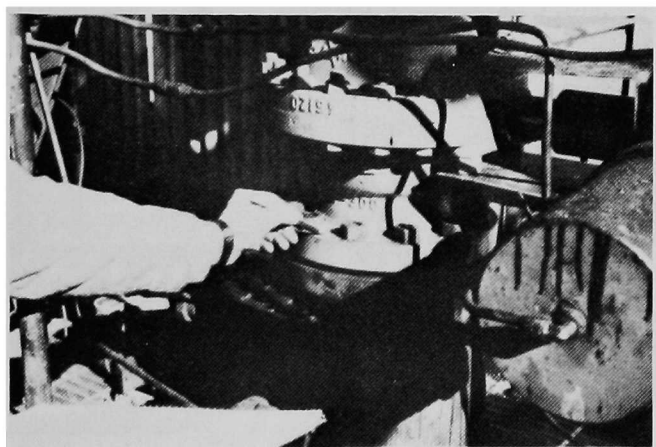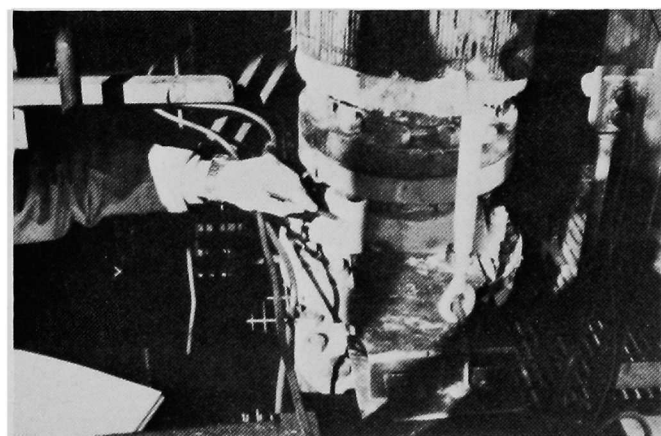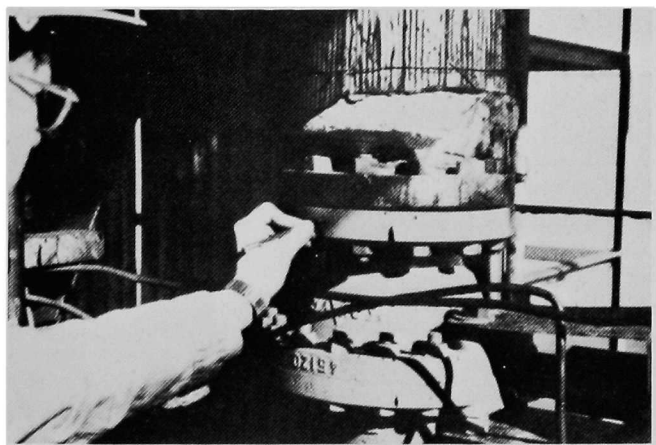
Fig. 25. Acoustic-emission Measurement Locations on the MERC Top Ash Lock-
hopper Valve. ANL Neg. No. 306-77-274.

(a)

(b)

(c)

Fig. 26. Acoustic-emission Measurement
Locations for the MERC North Bottom
Coal-feed Lockhopper Valve. ANL
Neg. No. 306-77-271.

52

(a)   (b)   (c)   (d)   (e)
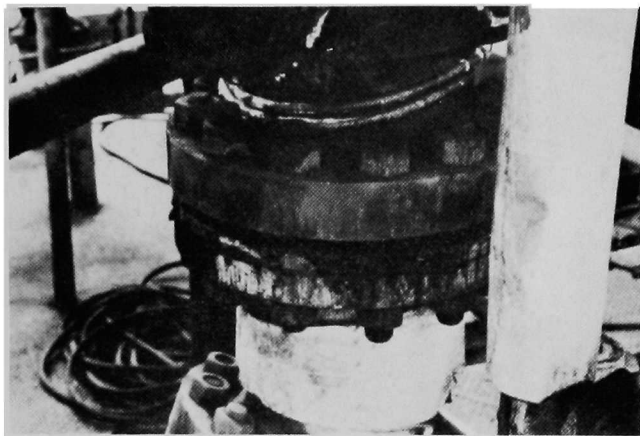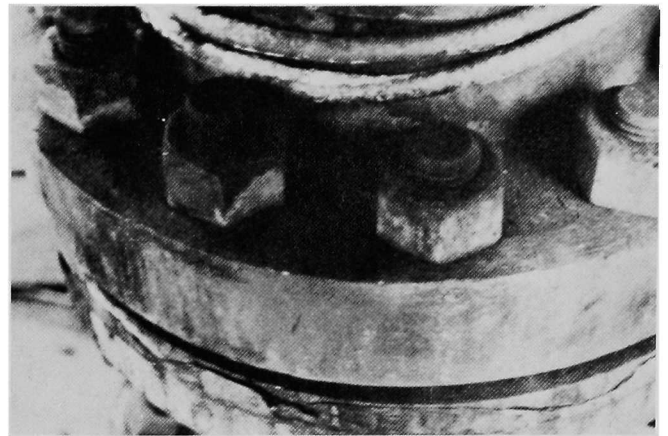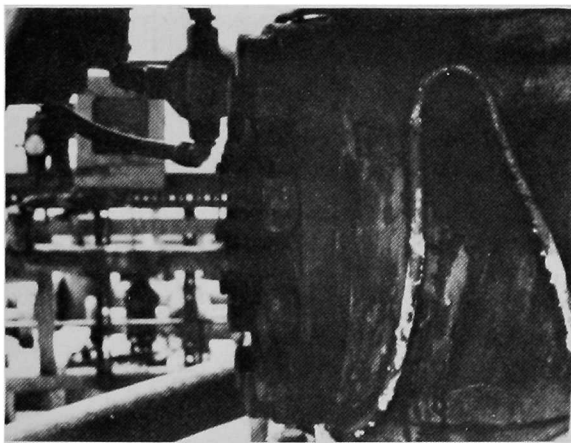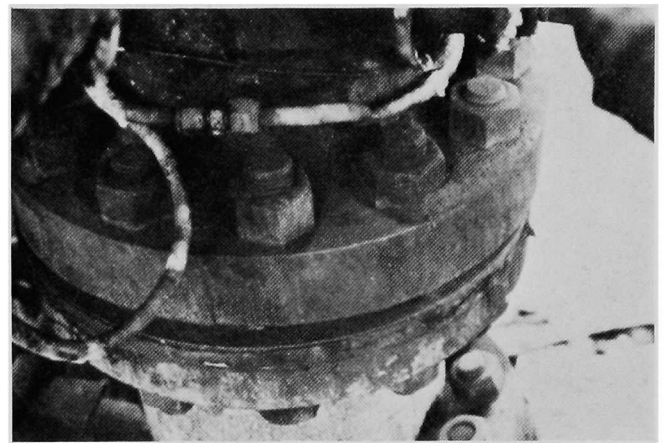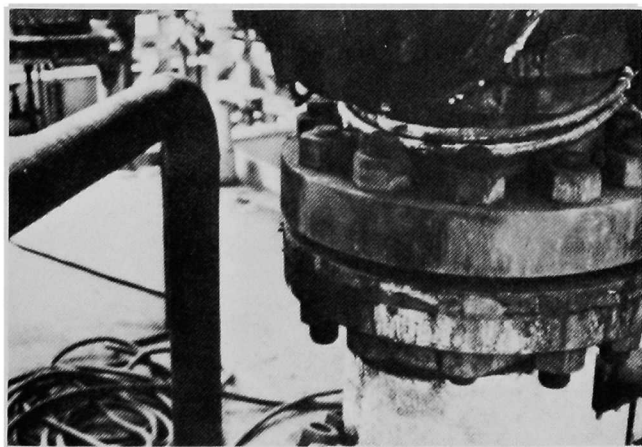
Fig. 27. Acoustic-emission Measurement Locations for the Synthane North Lower Petrocarb Feed Valves. ANL Neg. No. 306-77-266.

53

(a)

(b)

(c)
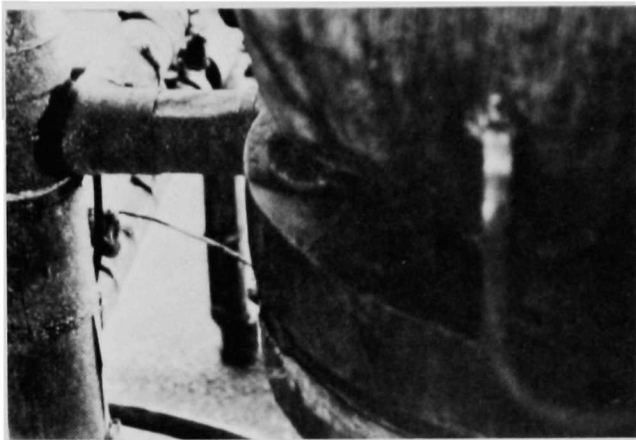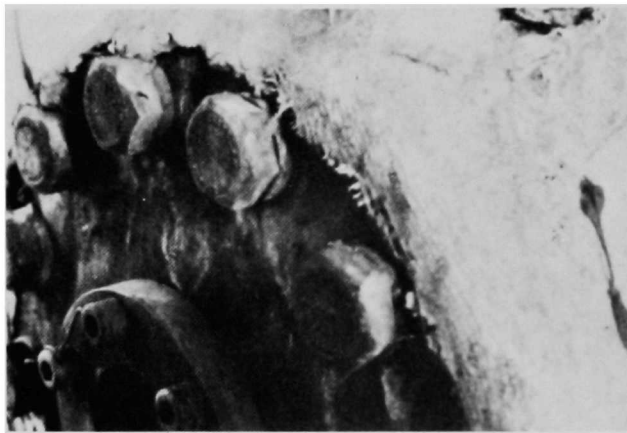
(d)

(e)

Fig. 28. Acoustic-emission Measurement Locations for the Synthane South Lower Petrocarb Feed Valves and Nearby Structure. ANL Neg. No. 306-77-273.

800 304 SS Iron 18-18-2 25 h

310 SS RA 333 671 406

310 SS 800 671 18-18-2 200 h

304 SS RA 333 406 Iron
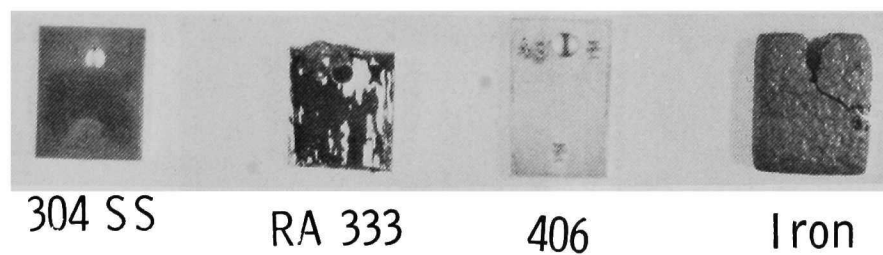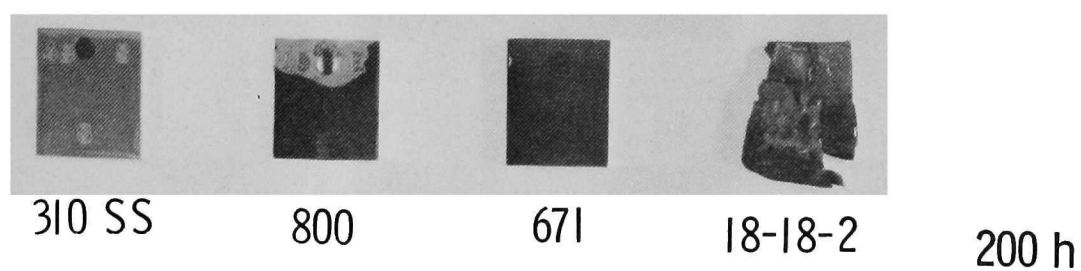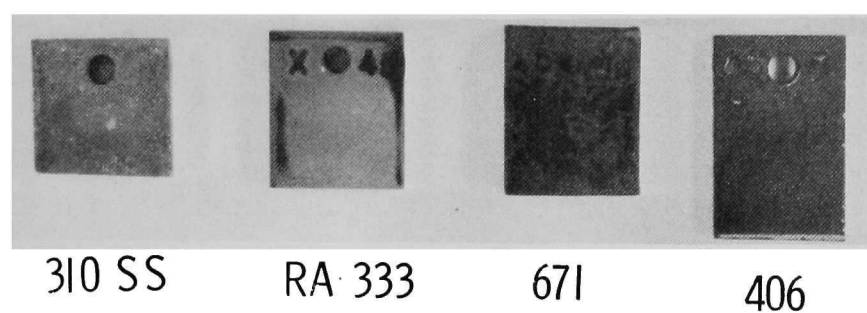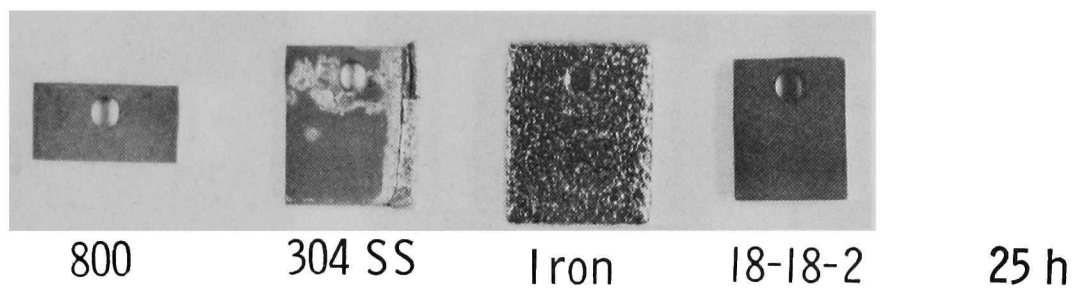
Fig. 29. Macroscopic Photographs of Specimens That Have Been Exposed to Multicomponent Gas Environment at 875°C for 25 h (Top) and 200 h (Bottom).
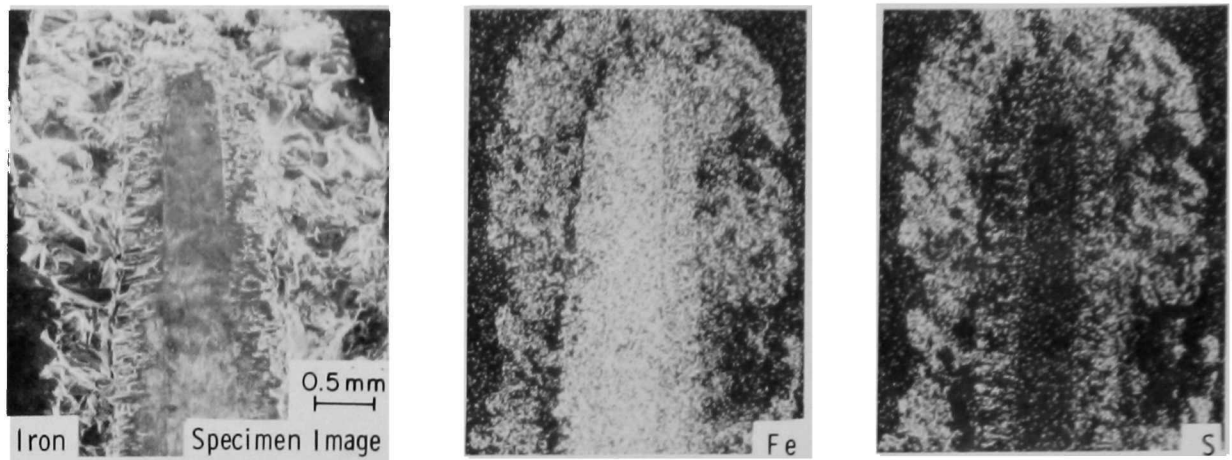
Fig. 30. X-ray Specimen Image and the Fe and S Distributions for an Iron Specimen Exposed to a Complex Gas Mixture at 875°C for 25 h.
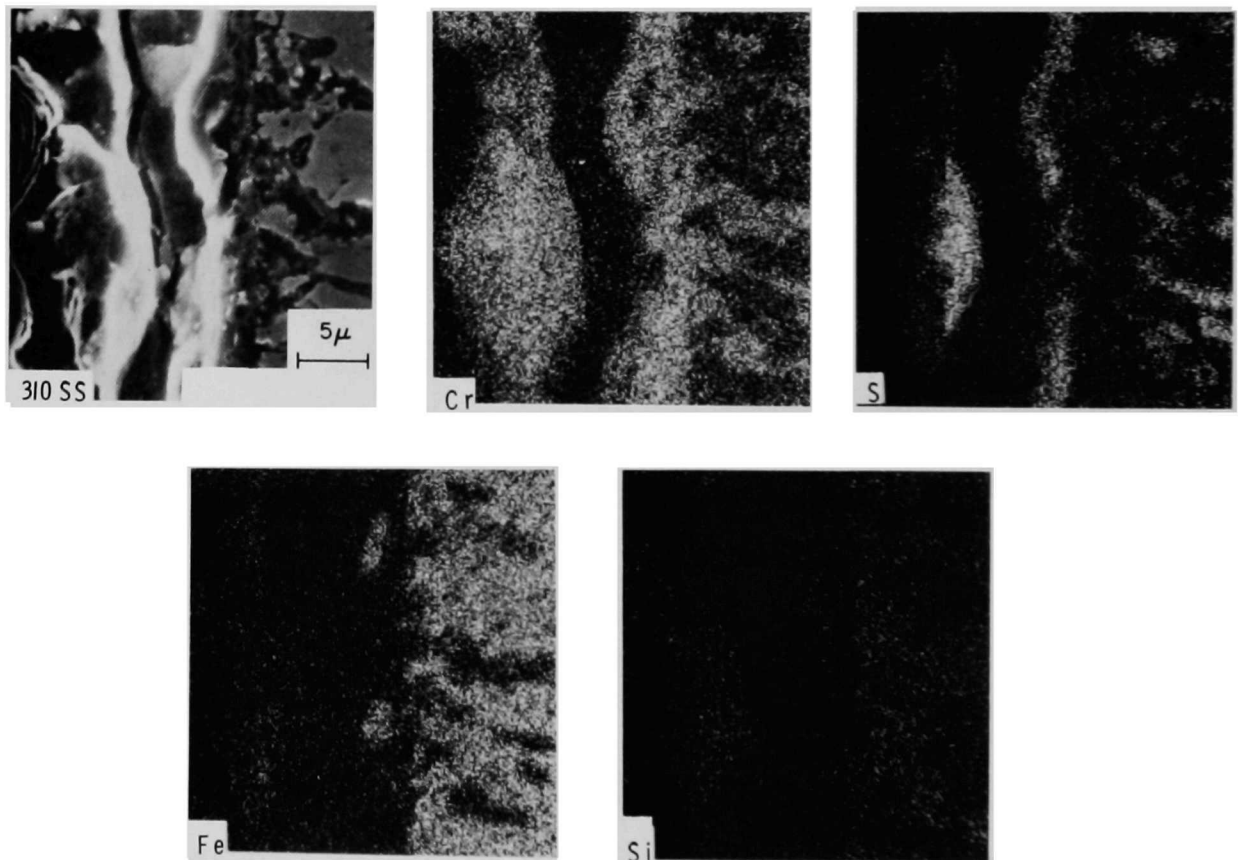
Fig. 31. X-ray Specimen Image and Cr, S, Fe, and Si Distributions in Type 310 Stainless Steel Exposed to the Gas Mixture Listed in Table X for 25 h at 875°C. In the distribution photographs, the light region indicates a high concentration of the respective elements.
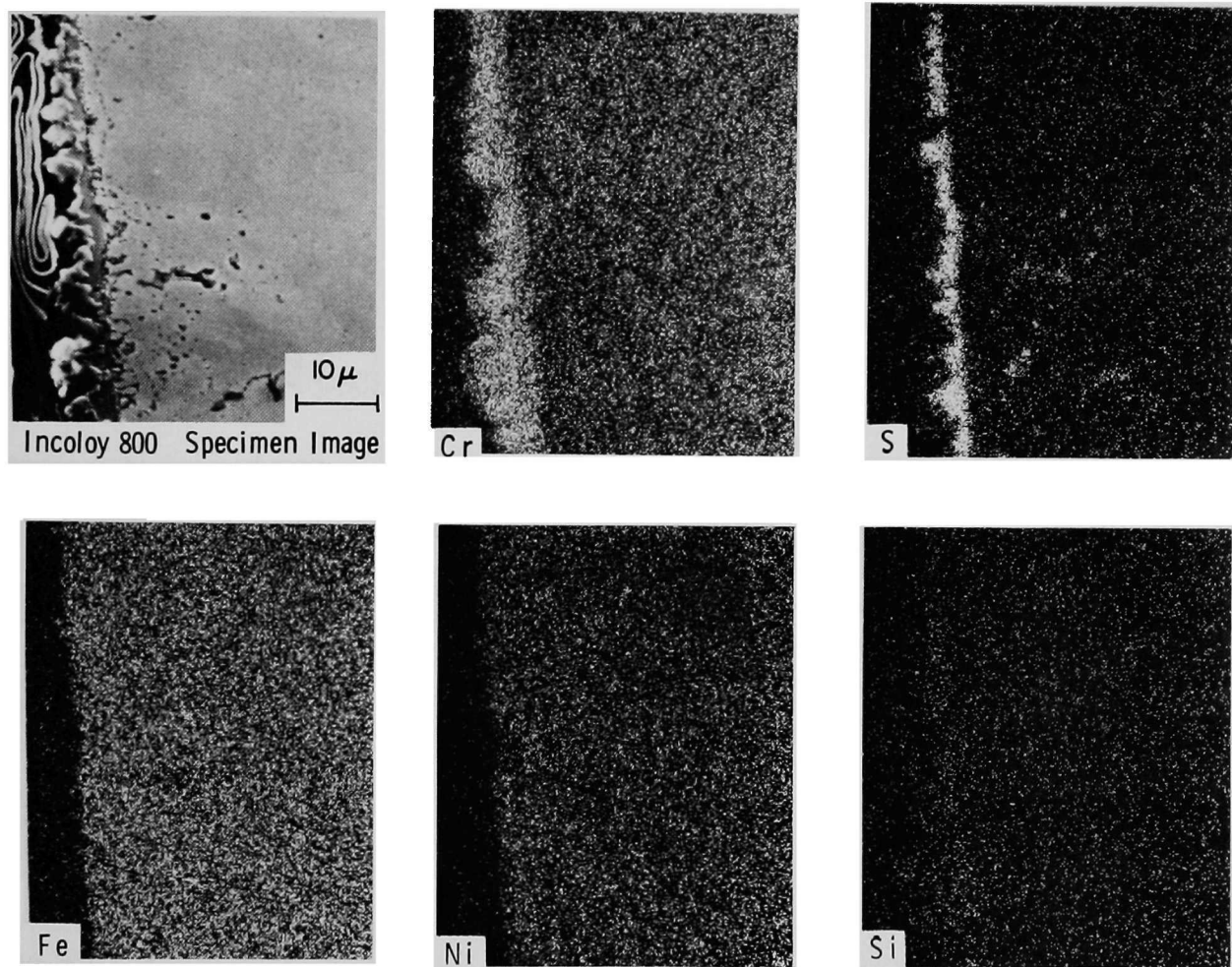
Fig. 32. X-ray Specimen Image and Cr, S, Fe, Ni, and Si Distributions
in Incoloy 800 Exposed to the Gas Mixture Listed in Table X for
25 h at 875°C. In the distribution photographs, the light region
indicates a high concentration of the respective elements.
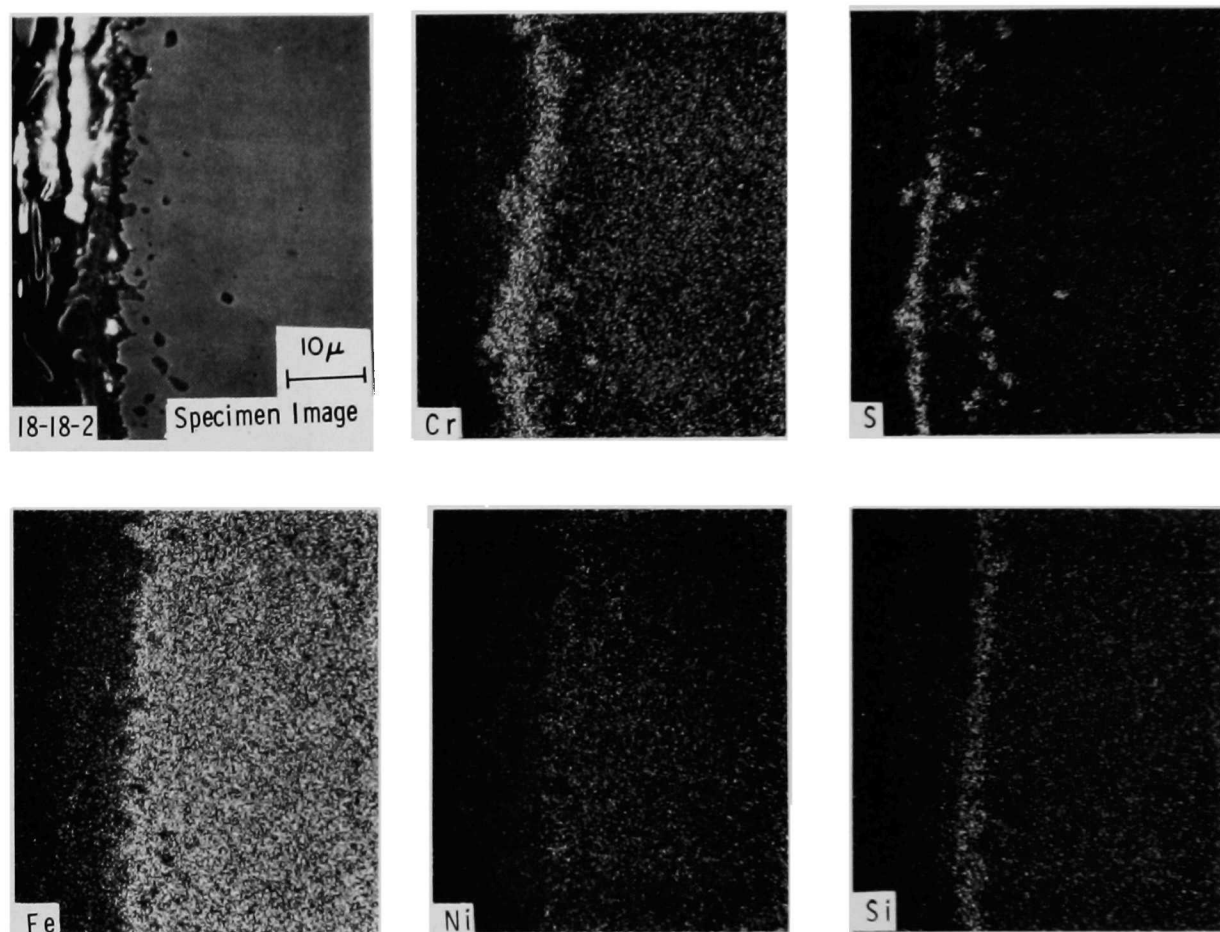
Fig. 33.   X-ray Specimen Image and Cr, S, Fe, Ni, and Si Distributions
    in U. S. Steel Alloy 18-18-2 Exposed to the Gas Mixture Listed in
    Table X for 25 h at 875°C.   In the distribution photographs, the
    light region indicates a high concentration of the respective
    elements.
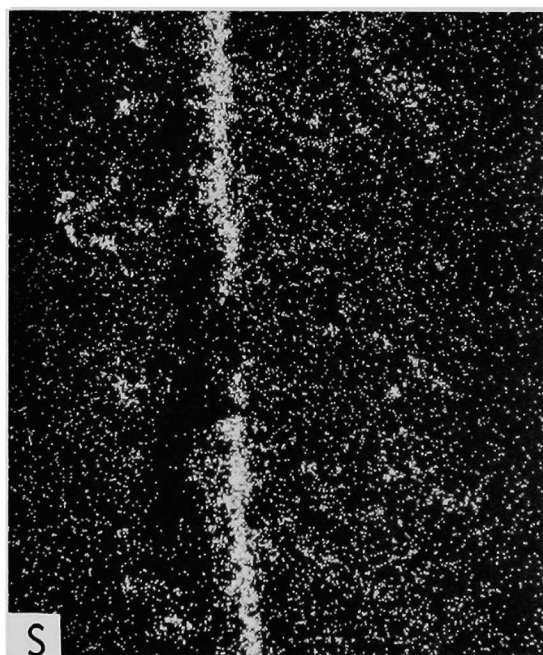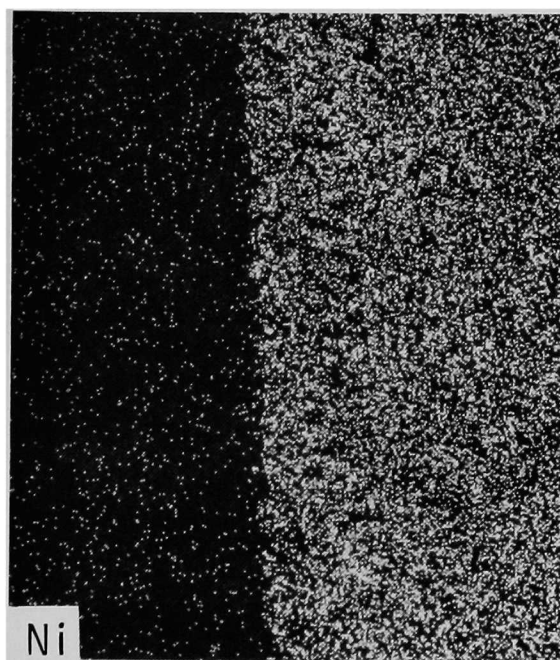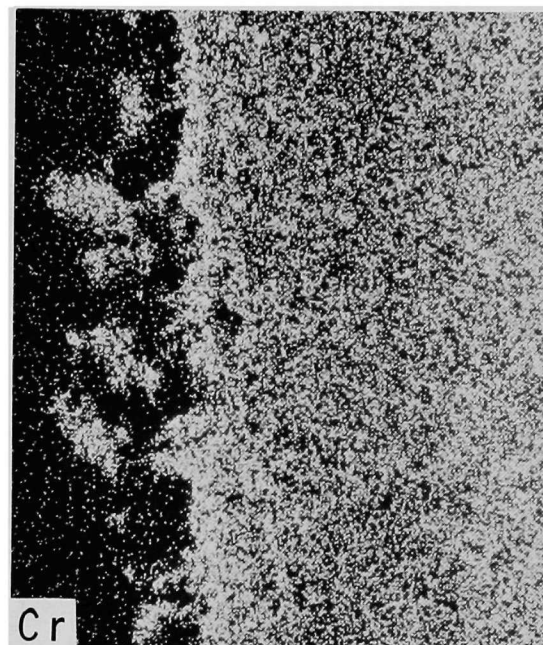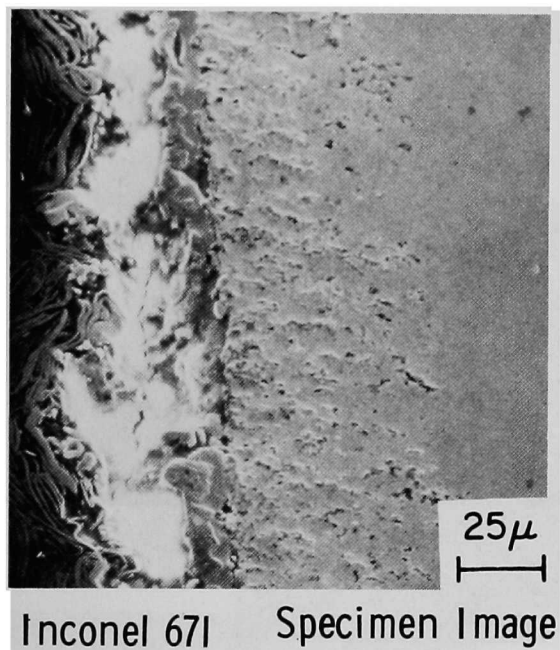
Fig. 34. X-ray Specimen Image and Cr, Ni, and S Distributions in
Inconel 671 Exposed to the Gas Mixture Listed in Table X for
25 h at 875°C. In the distribution photographs, the light
region indicates a high concentration of the respective elements.
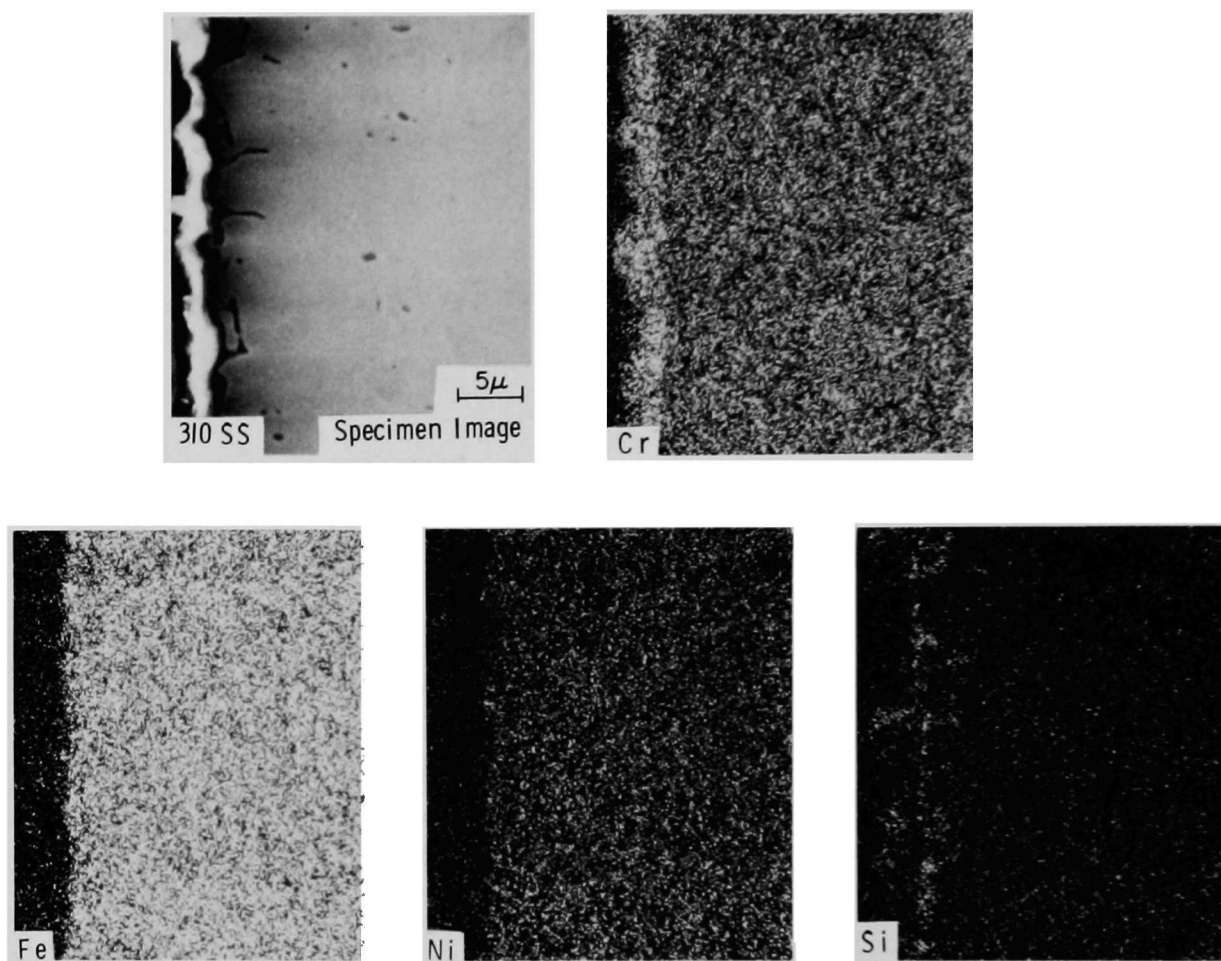
Fig. 35. X-ray Specimen Image and Cr, Fe, Ni, and Si Distributions
in Type 310 Stainless Steel Exposed to the Gas Mixture Listed in
Table X for 200 h at 875°C. Sulfur was absent in this specimen.
In the distribution photographs, the light region indicates a
high concentration of the respective elements.
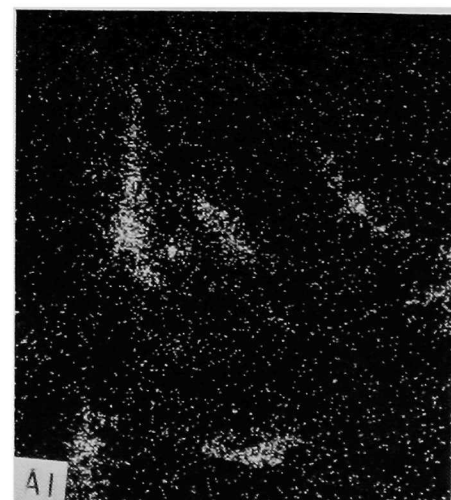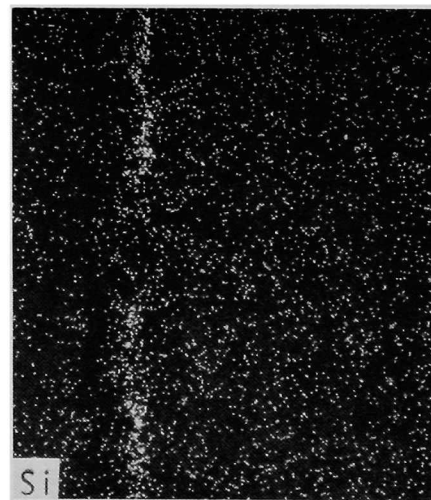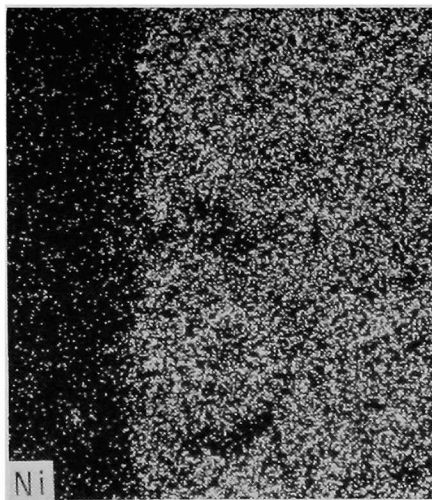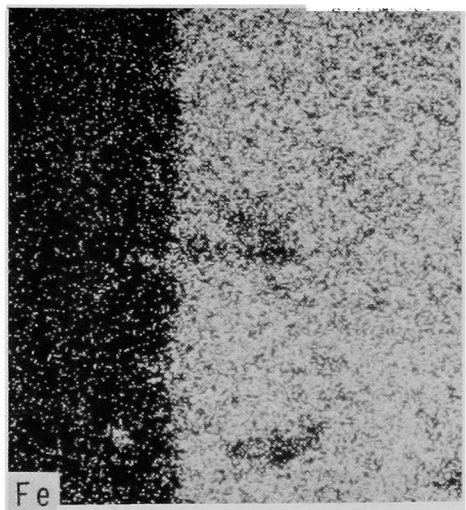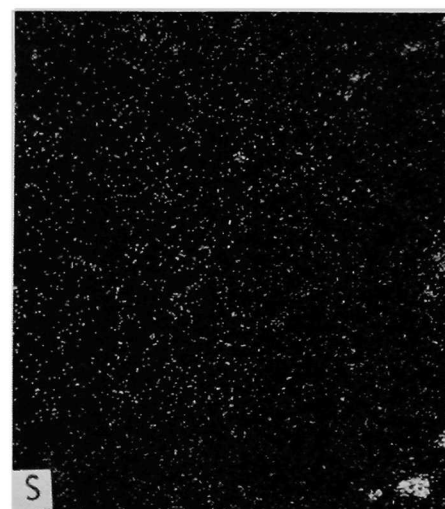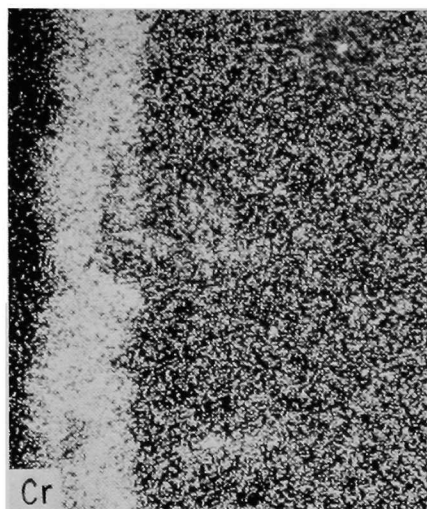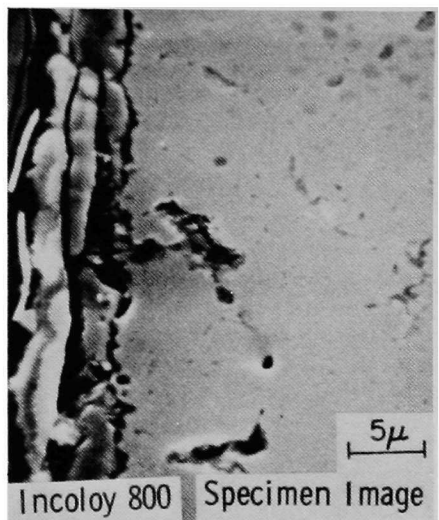
Fig. 36. X-ray Specimen Image and Cr, S, Fe, Ni, Si, and Al Distributions in Incoloy 800 Exposed to the Gas Mixture Listed in Table X for 200 h at 875°C. In the distribution photographs, the light region indicates a high concentration of the respective elements.
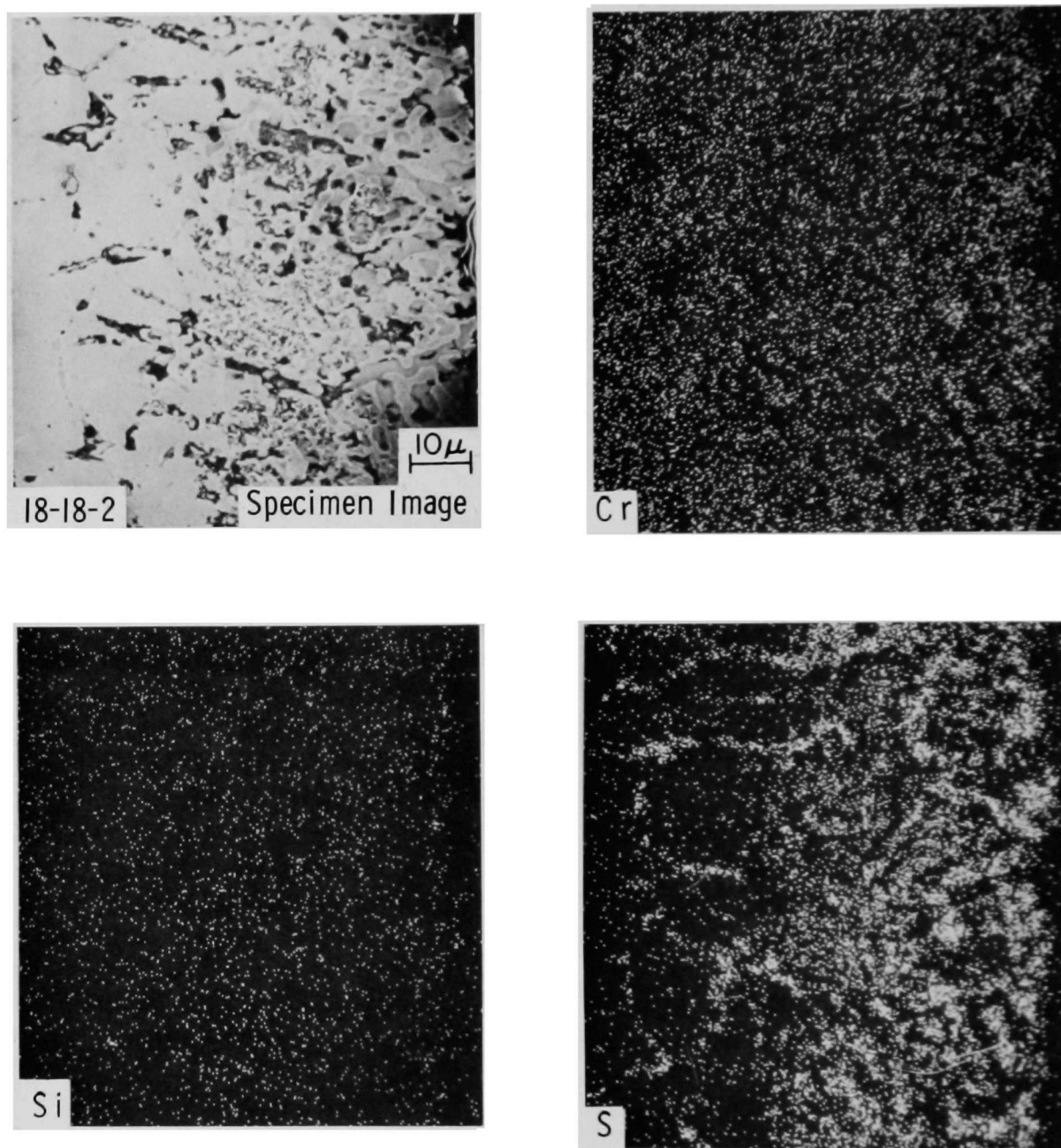
Fig. 37. X-ray Specimen Image and Cr, Si, and S Distributions in
the Alloy Regions of U. S. Steel Alloy 18-18-2 Exposed to the
Gas Mixture Listed in Table X for 200 h at 875°C. In the distri-
bution photographs, the light region indicates a high concentra-
tion of the respective elements.
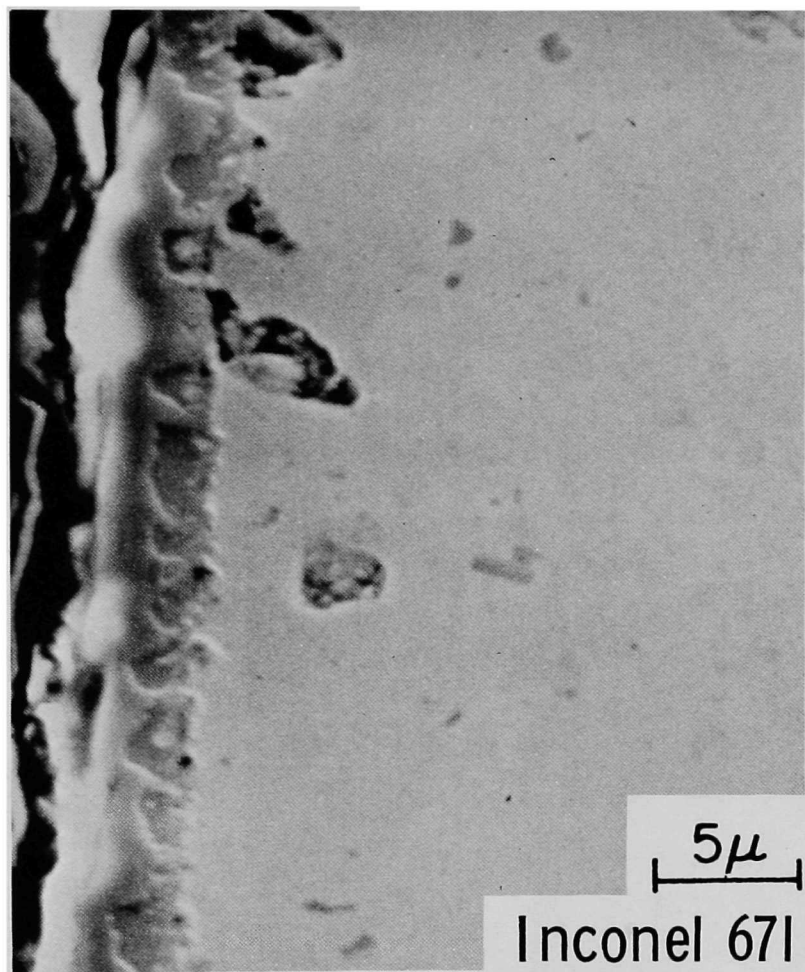
Fig. 38. SEM Photograph of Inconel 671 Specimen
Exposed to the Gas Mixture Listed in Table X
for 200 h at 875°C. The scale is predomi-
nantly Cr-rich oxide, and no S was detected.
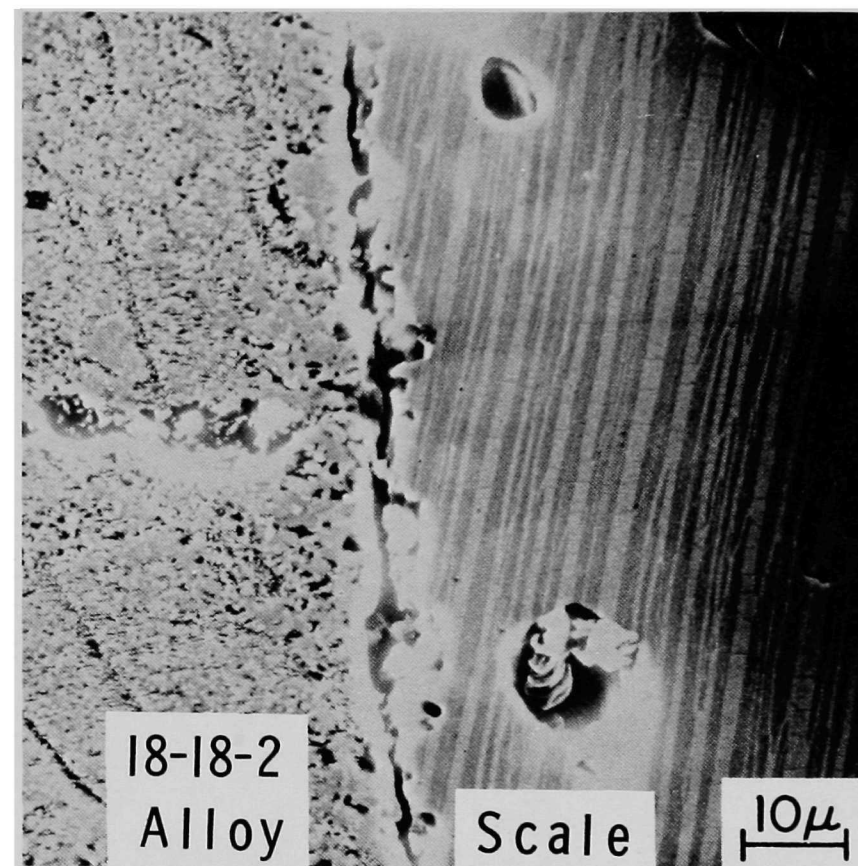
Fig. 39. SEM Photograph of Scale/Alloy Inter-
face Regions of U. S. Steel Alloy 18-18-2
Exposed to the Gas Mixture Listed in Table X
for 200 h at 875°C. The striated region of
the scale consisted of Cr sulfide and Fe
sulfide.

800

304 SS

310 SS

Iron

RA 333

671
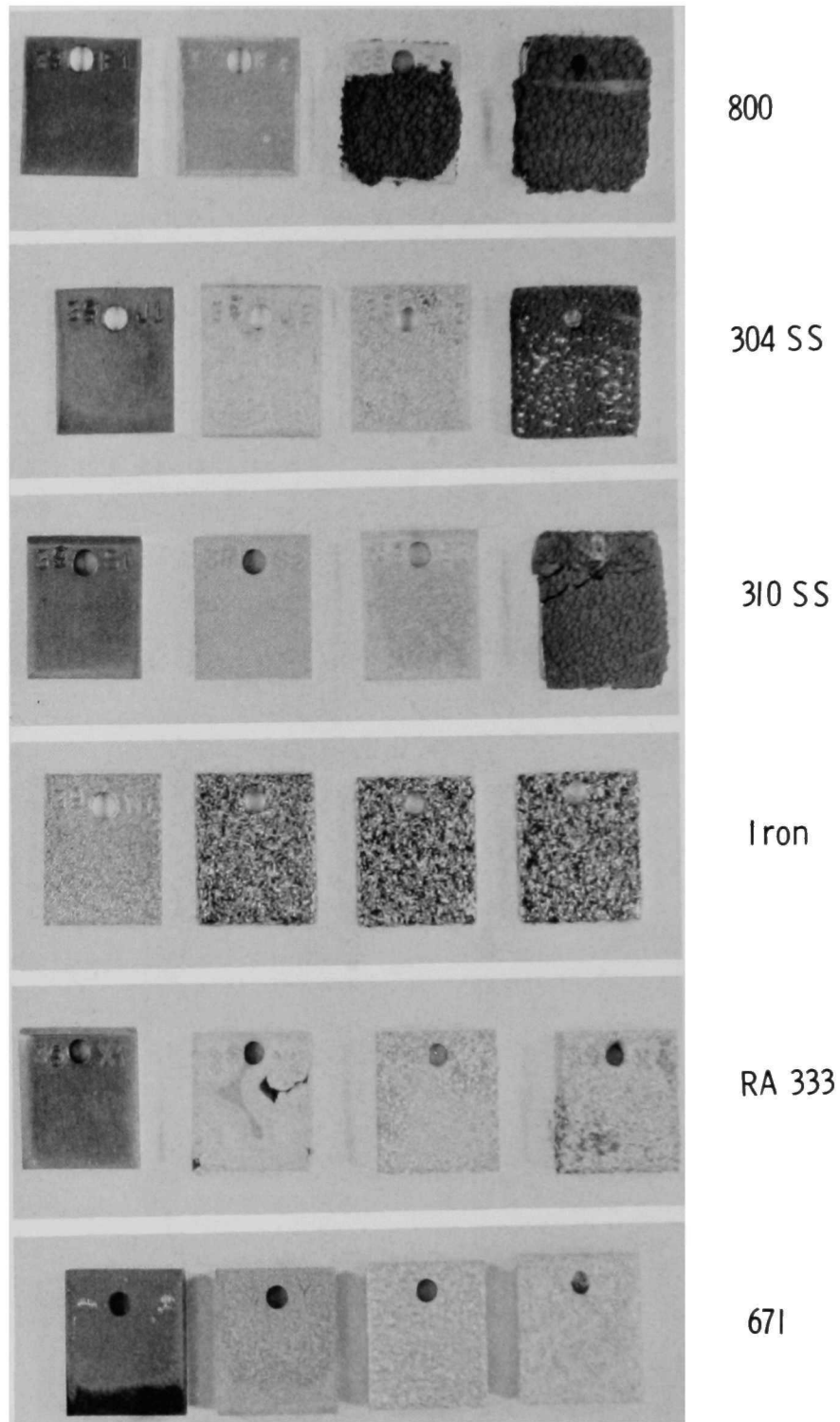
750 C 25 h

Fig. 40. Macroscopic Photographs of Different Alloy
Specimens after 25-h Exposure at 750°C to the Gas
Mixtures Listed in Table XII. The oxygen partial
pressures for these specimens from left to right
are 1.0×10^{-20}, 2.4×10^{-21}, 4.1×10^{-22}, and
4.2×10^{-23} atm.

800

304 SS

310 SS

Iron

RA 333

671
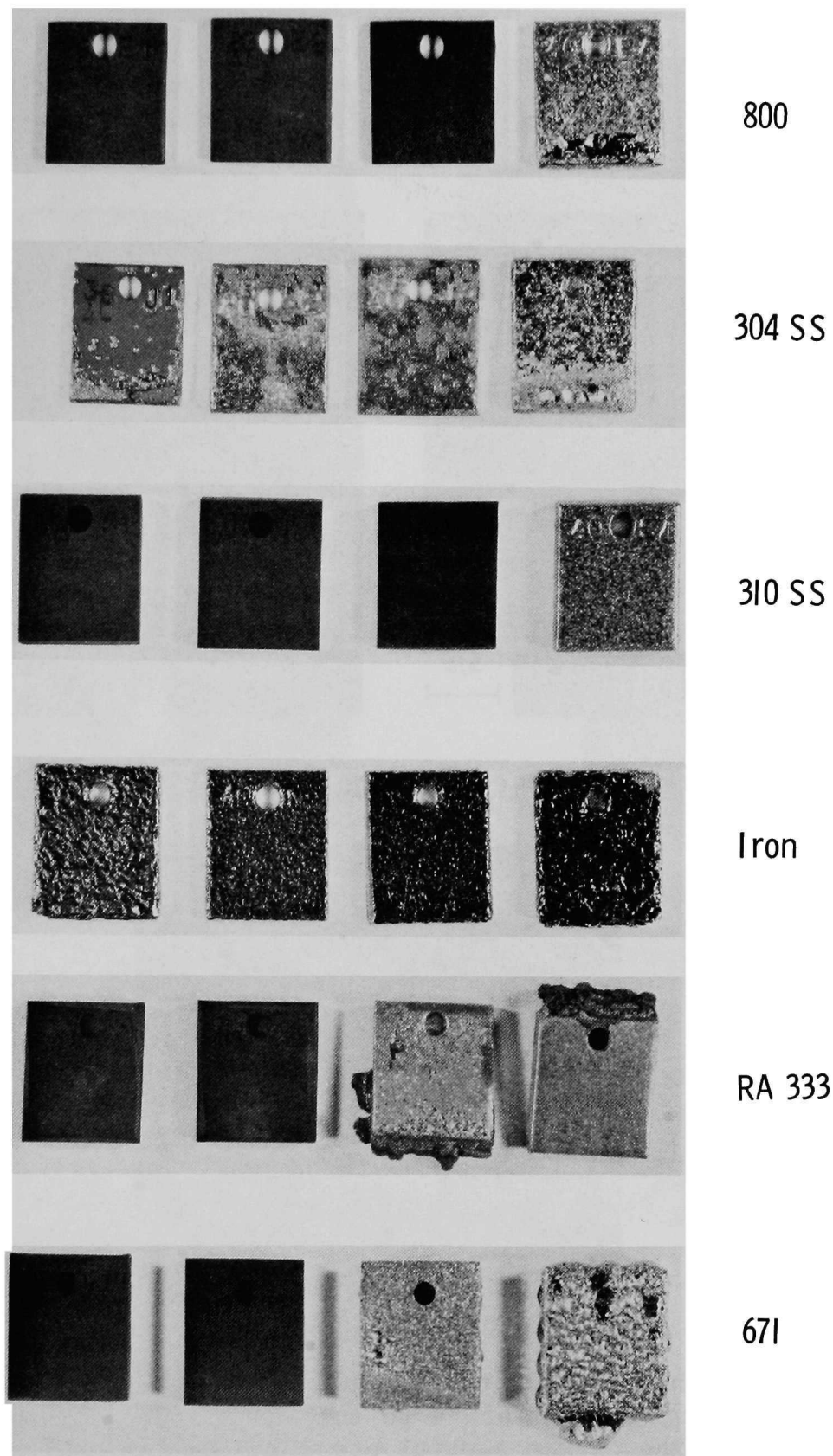
875 C 25 h

Fig. 41. Macroscopic Photographs of Different Alloy
Specimens after 25-h Exposure at 875°C to the Gas
Mixtures Listed in Table XII. The oxygen partial
pressures for these specimens from left to right
are 1.9×10^{-18}, 5.5×10^{-19}, 2.4×10^{-19}, and
1.7×10^{-20} atm.
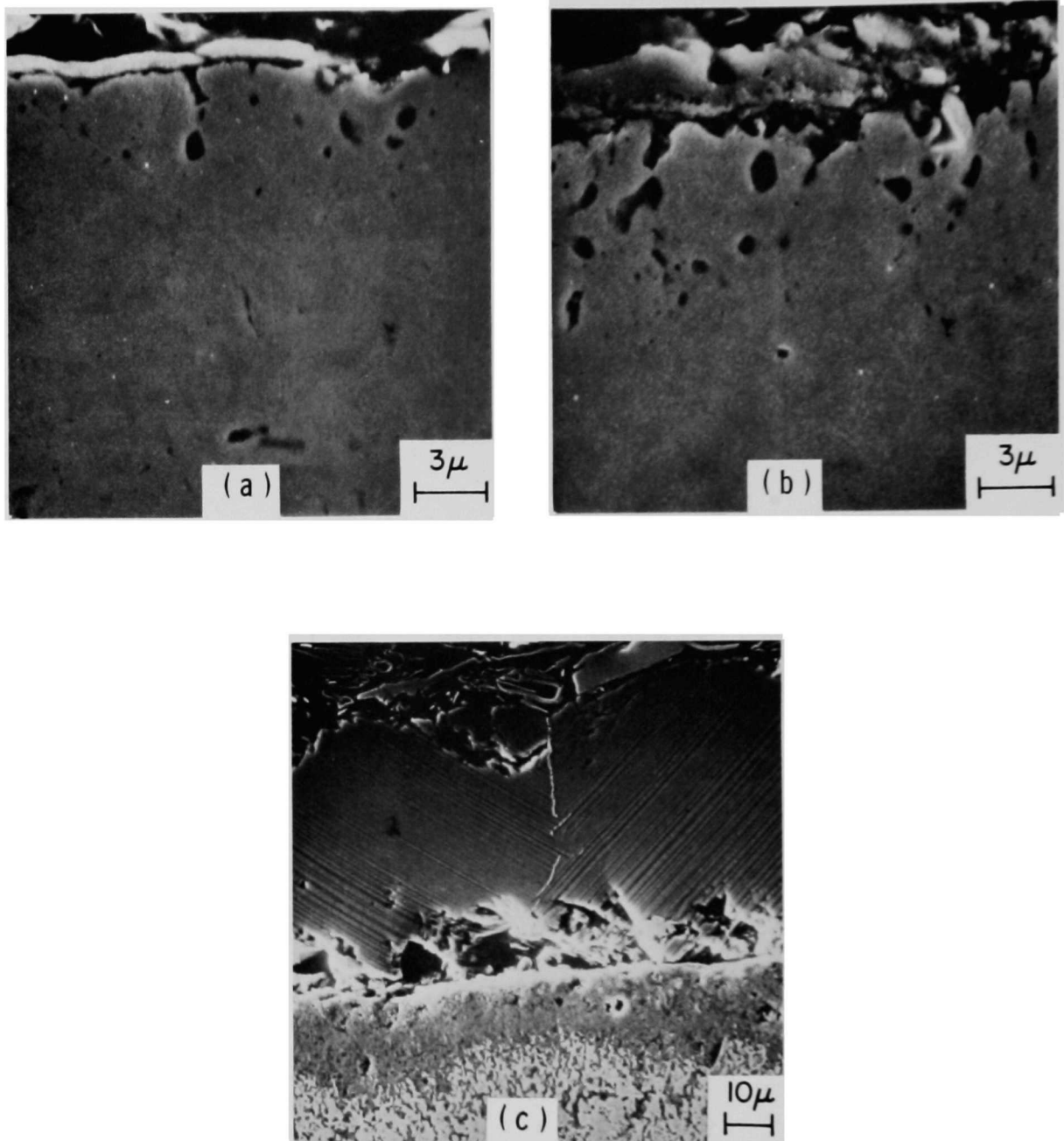
Fig. 42. SEM Photographs of Type 310 Stainless Steel Specimens after 25-h Exposure at 750°C to the Gas Mixtures Listed in Table XII. The oxygen partial pressures in (a), (b), and (c) were 1.0×10^{-20}, 2.4×10^{-21}, and 4.1×10^{-22} atm, respectively.
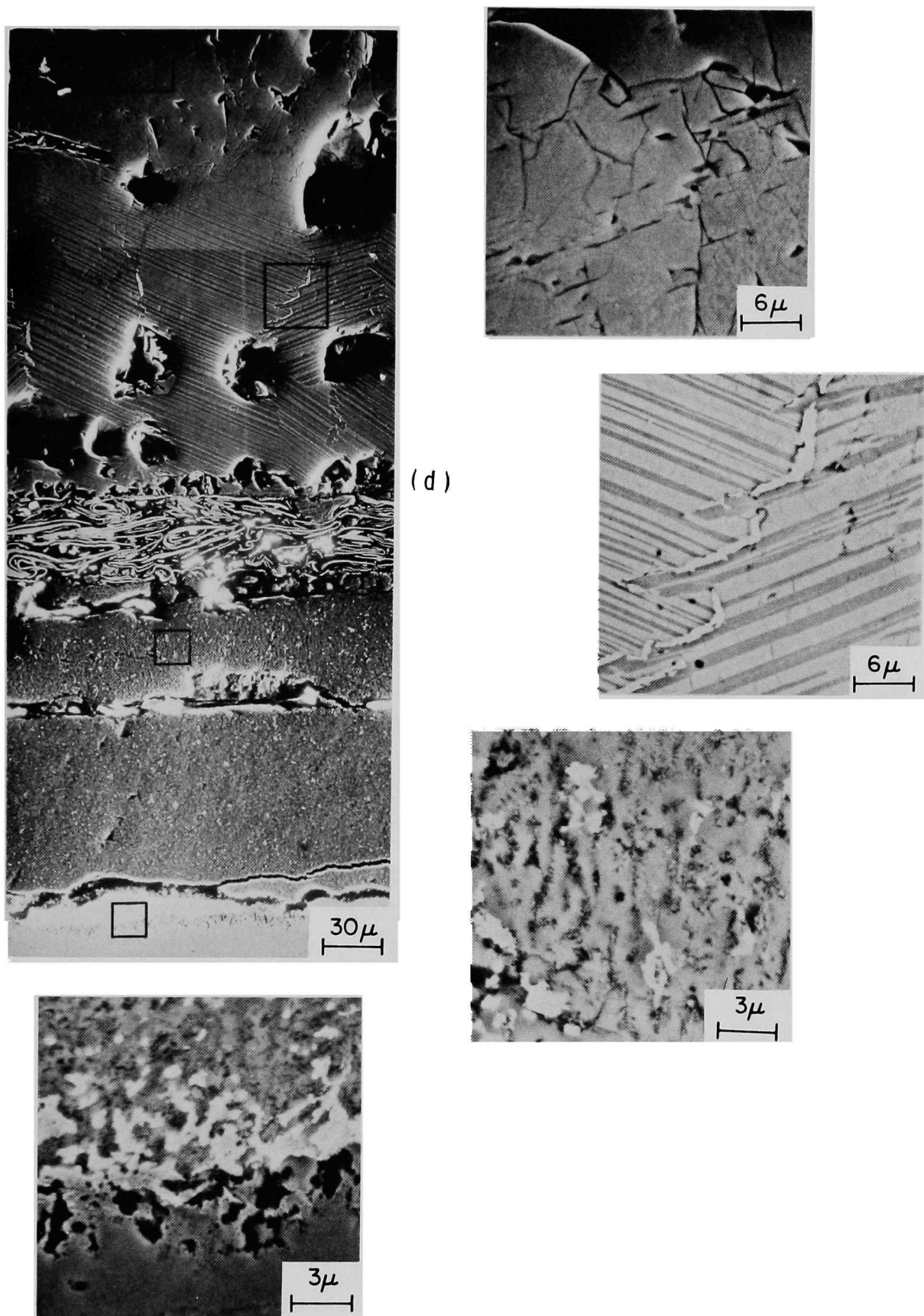
Fig. 43. SEM Photograph of Type 310 Stainless Steel Specimen after
25-h Exposure at 750°C to the Gas Mixture Listed in Table XII.
The oxygen partial pressure during this experiment was 4.2×10^{-23}
atm. Different square-marked regions were magnified to show the
details of the scale and scale/alloy interface.
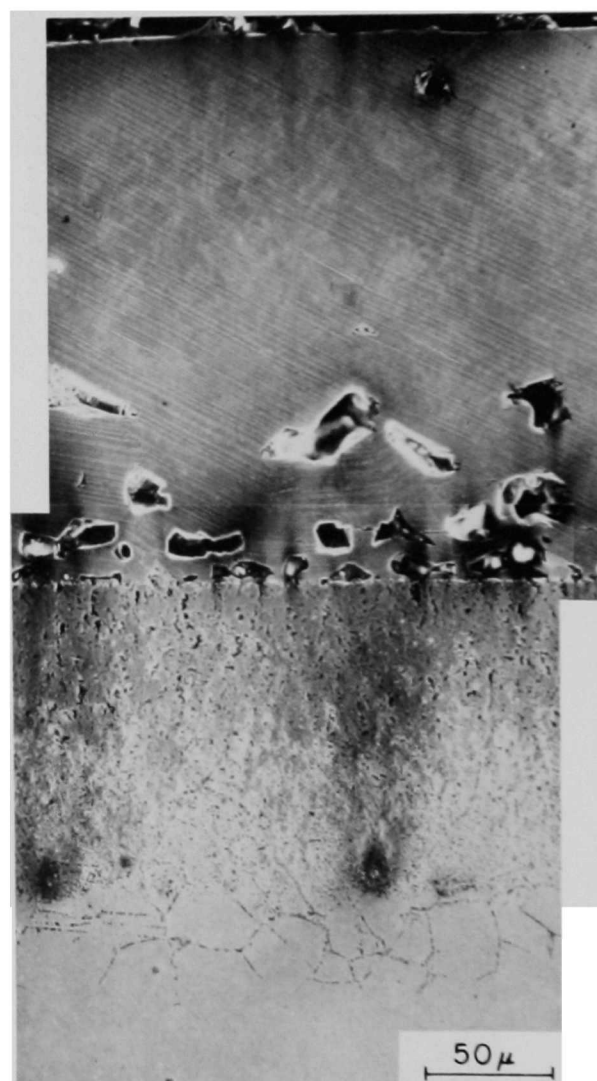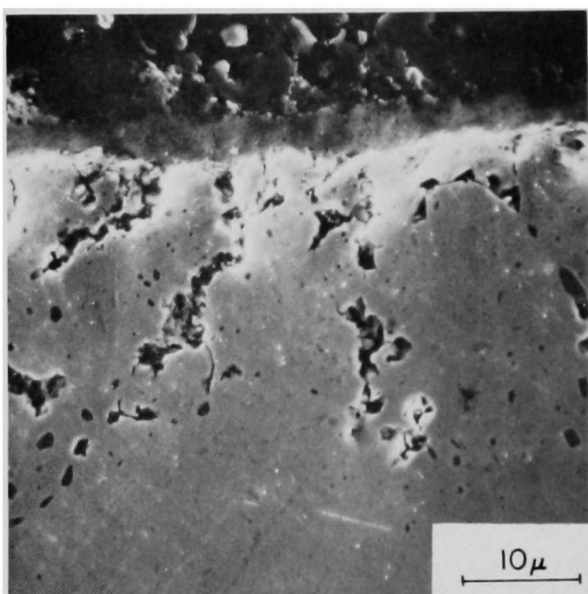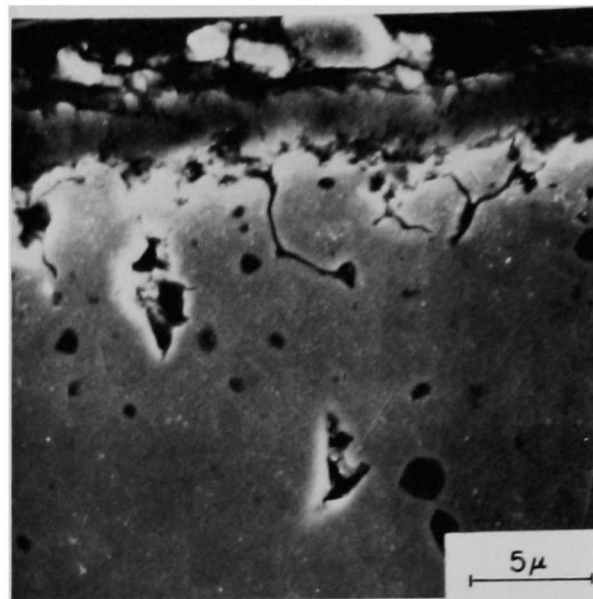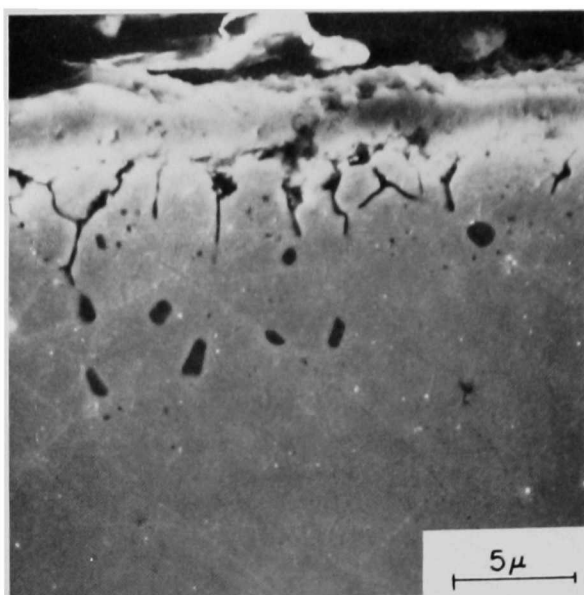
Fig. 44. SEM Photographs of Type 310 Stainless Steel Specimens
after 25-h Exposure at 875°C to the Gas Mixtures Listed in
Table XII. The oxygen partial pressures in these experiments
are as follows: top left, 1.9×10^{-18} atm; top right,
5.5×10^{-19} atm; bottom left, 2.4×10^{-19} atm; and bottom
right, 1.7×10^{-20} atm.
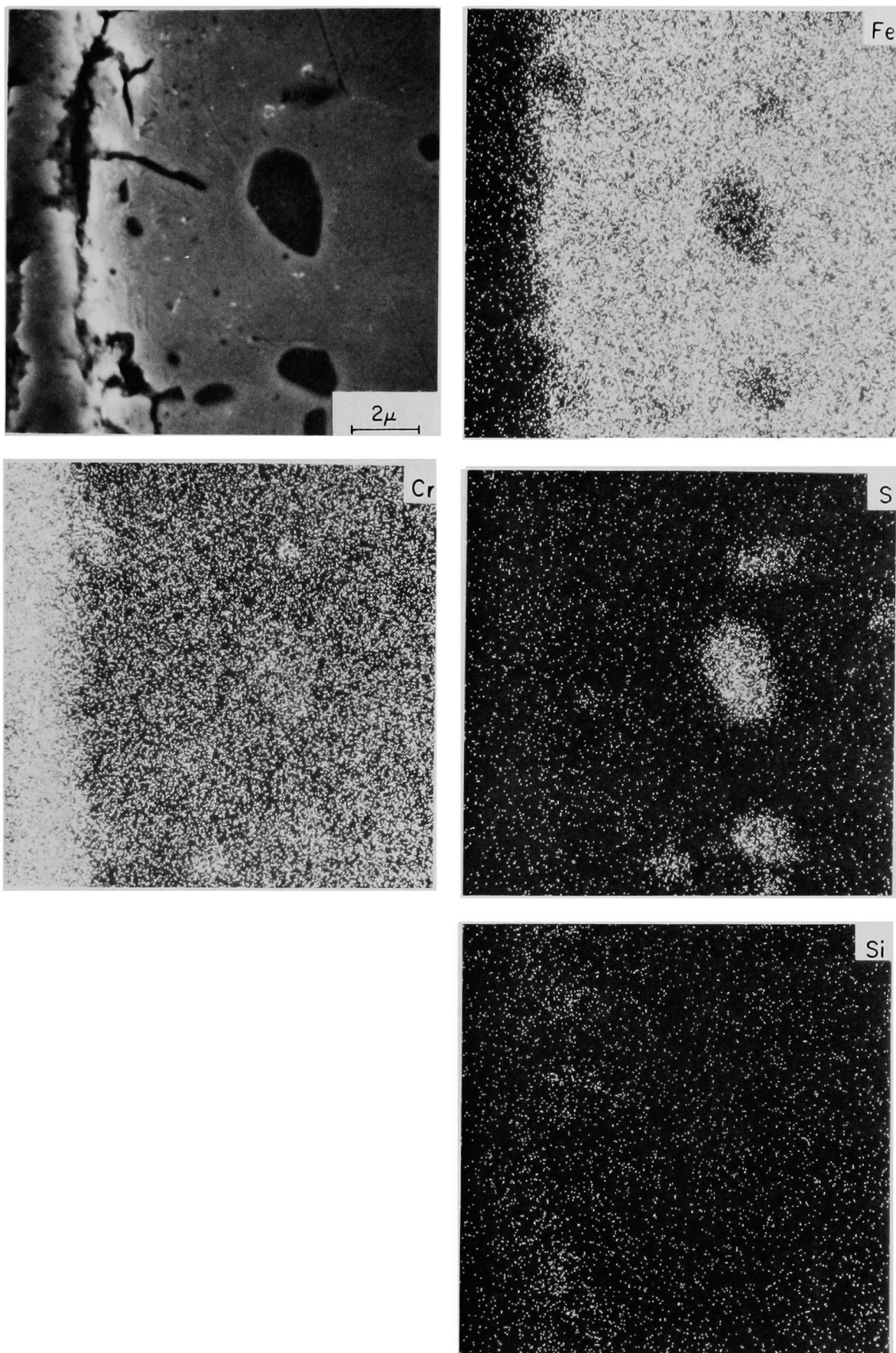
Fig. 45. X-ray Specimen Image and Fe, Cr, S, and Si Distributions in Type 310 Stainless Steel after 25-h Exposure at 875°C to the Gas Mixture *without Steam* Listed in Table XII (Identified by an Arrow). In the distribution photographs, the light region indicates a high concentration of the respective elements.
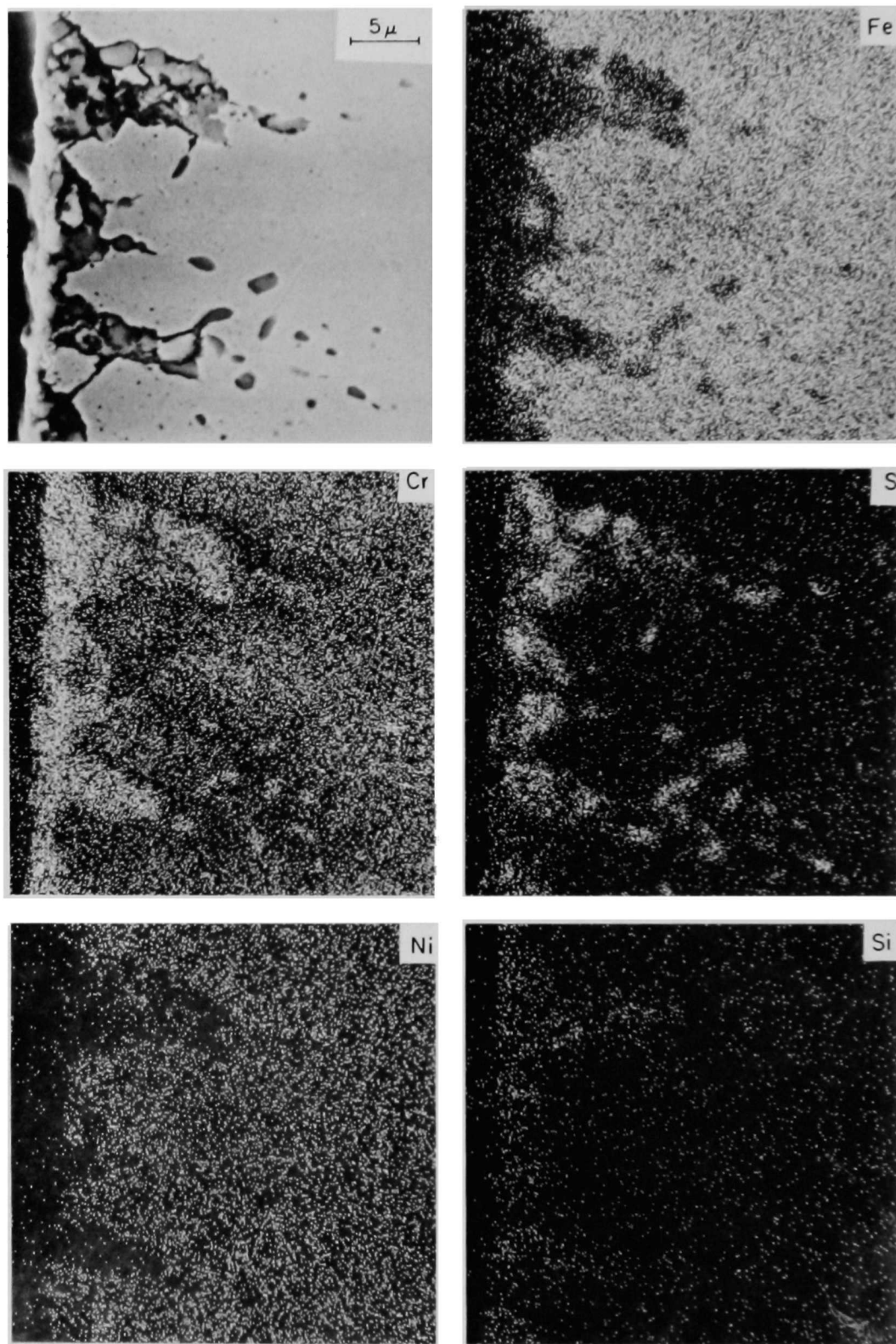
Fig. 46. X-ray Specimen Image and Fe, Cr, S, Ni, and Si Distri-
butions in Type 310 Stainless Steel after 25-h Exposure at 875°C
to the Gas Mixture *with Steam* Listed in Table XII. In the
distribution photographs, the light region indicates a high
concentration of the respective elements.
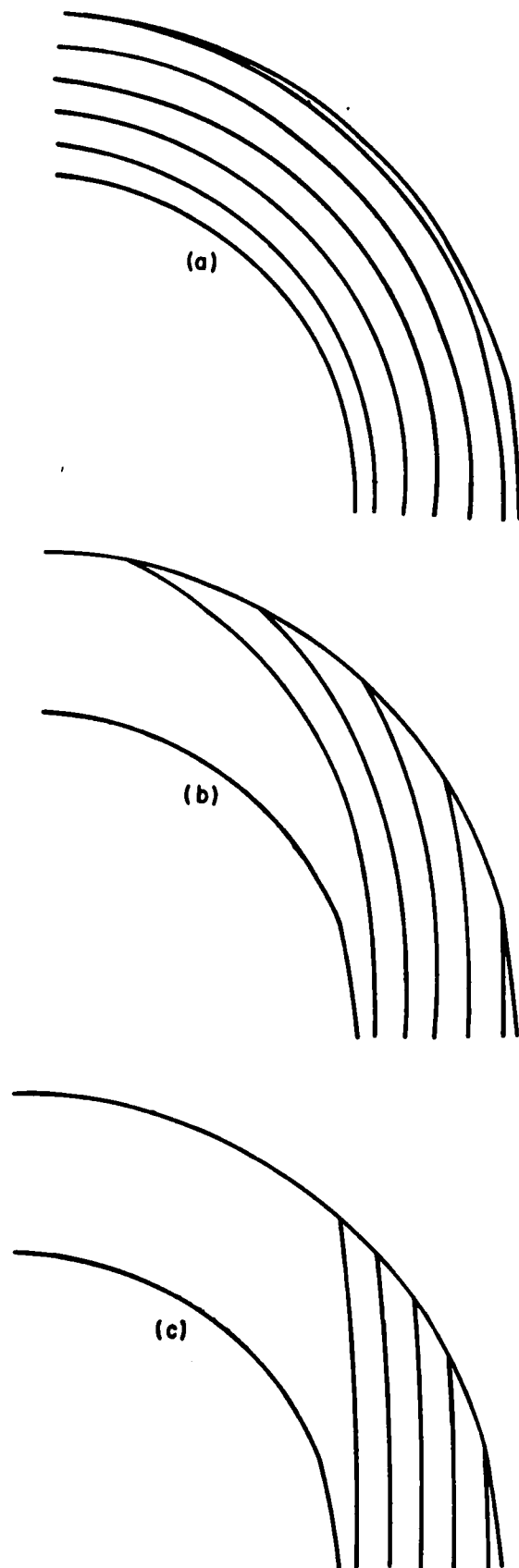
Fig. 47. Particle Trajectories in a
90° Elbow. Flow conditions:
U_o = 6 m/s, kinematic viscosity =
6 x 10^{-7} m^2/s, and fluid density =
54 kg/m^3. The particle density =
3.1 x 10^3 kg/m^3 and the particle
diameters are (a) 10 μ, (b) 100 μ,
and (c) 1000 μ. ANL Neg. No. 306-
77-190.

71
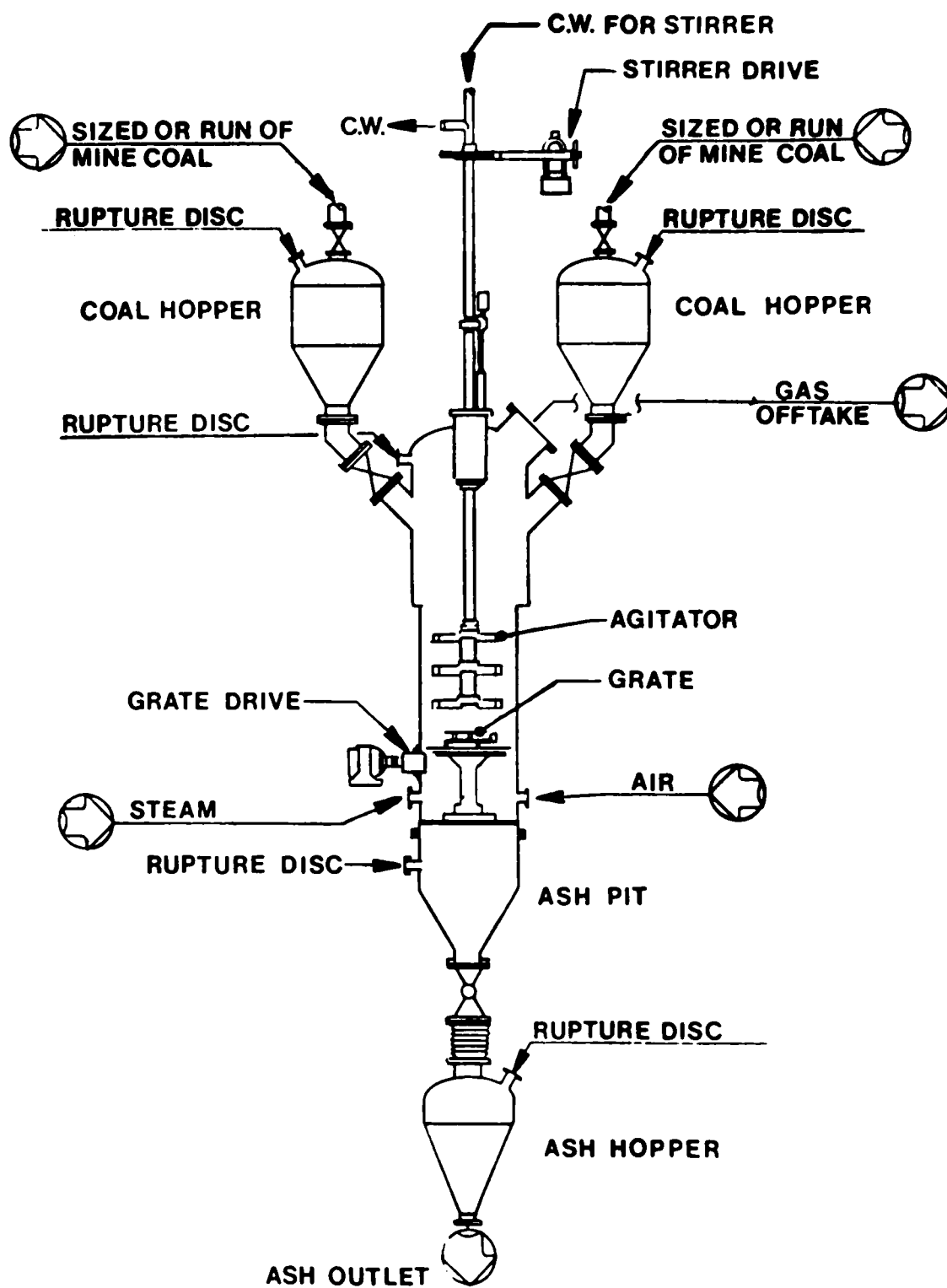
Fig. 48. ERDA-MERC Stirred-bed Gasifier. ANL Neg. No. 306-77-175.

WATER
FLOW

WELD METAL

7.62 cm (3-in.) OD
2.54 cm (I-in.) ID
CARBON STEEL

WELD METAL

CROSS SECTIONAL
VIEW
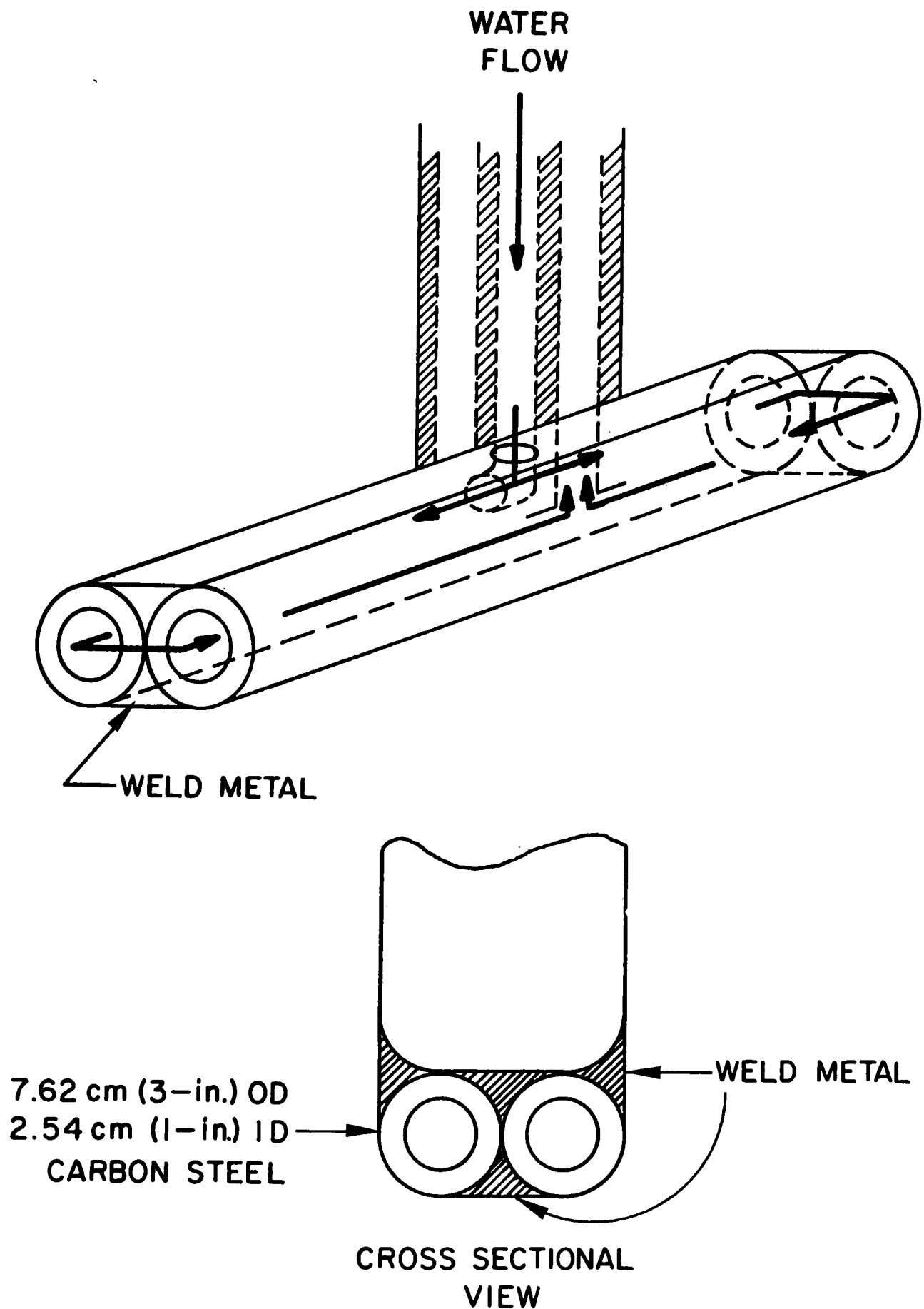
Fig. 49. Schematic of the Rabble Arm. ANL Neg. No. 306-77-183.
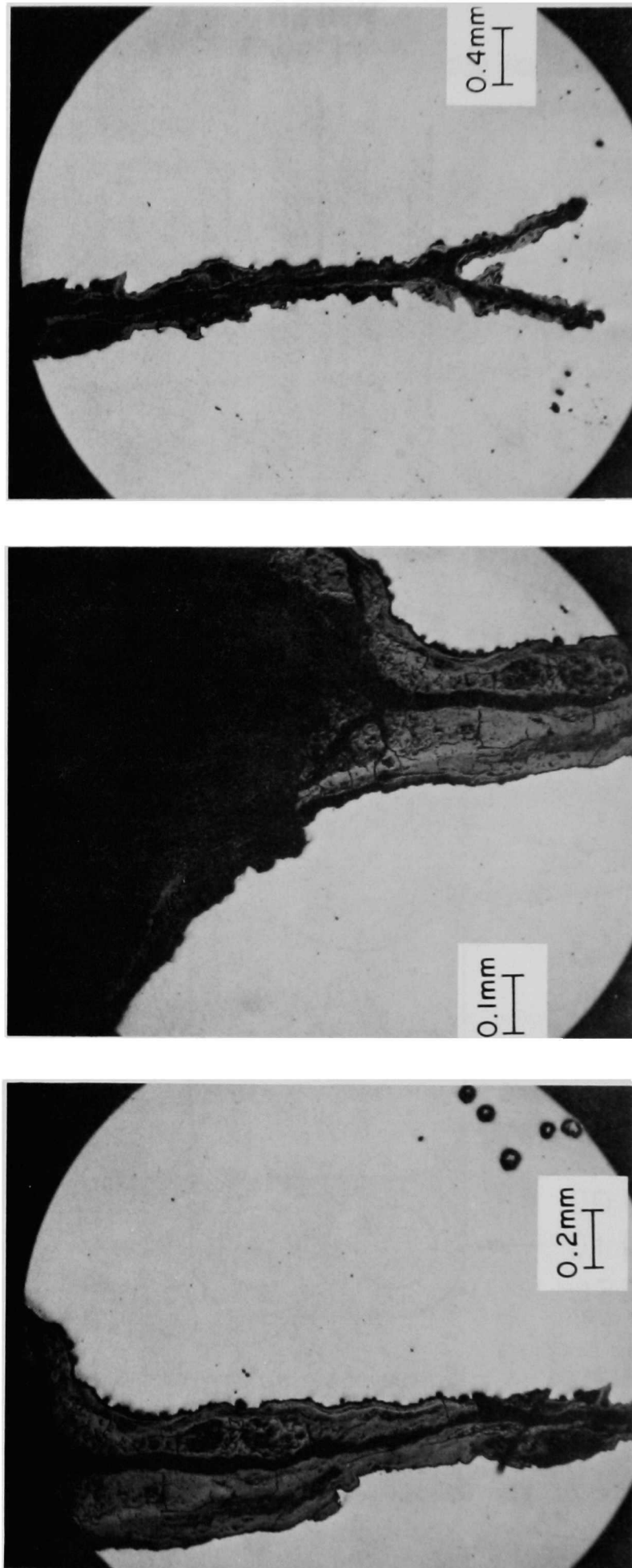
Fig. 50. Photographs of the Cracked Corrosion Scale and the Crack Tip. ANL Neg. No. 306-77-199.

74
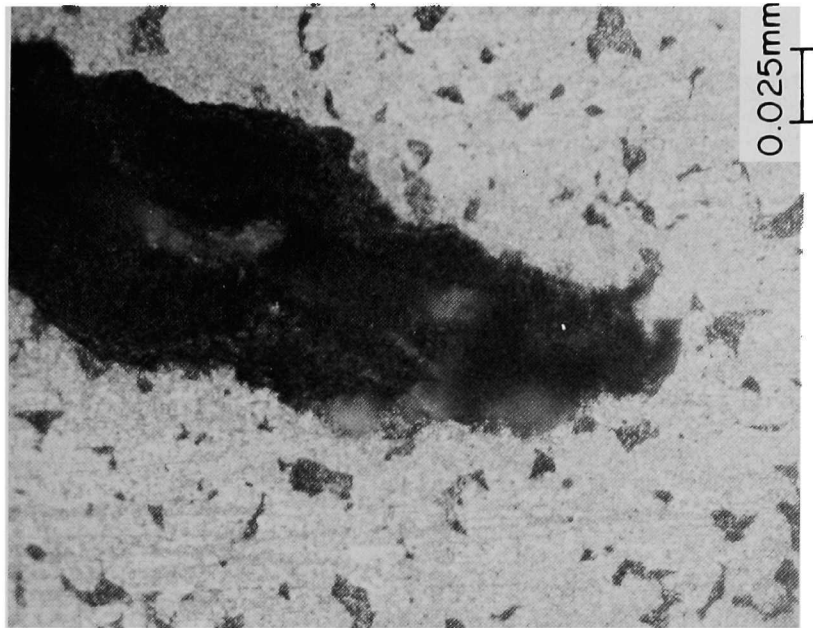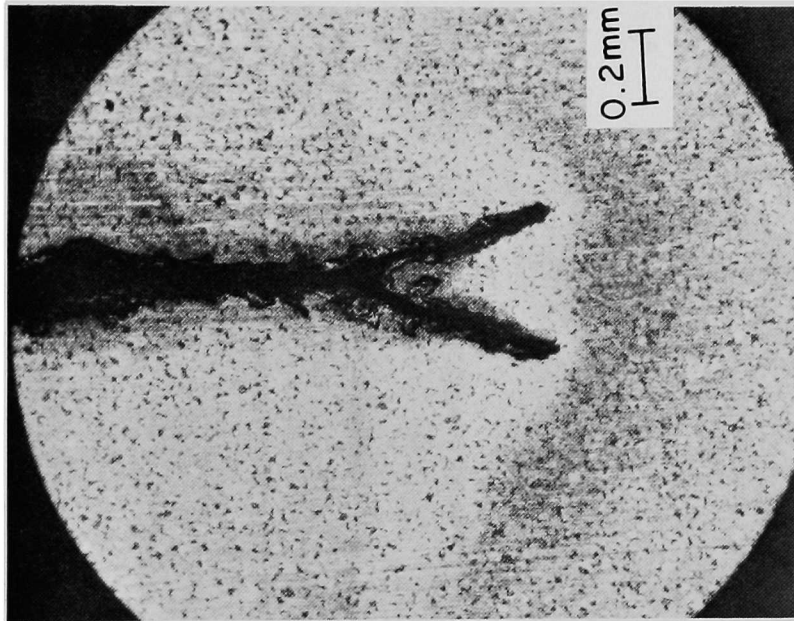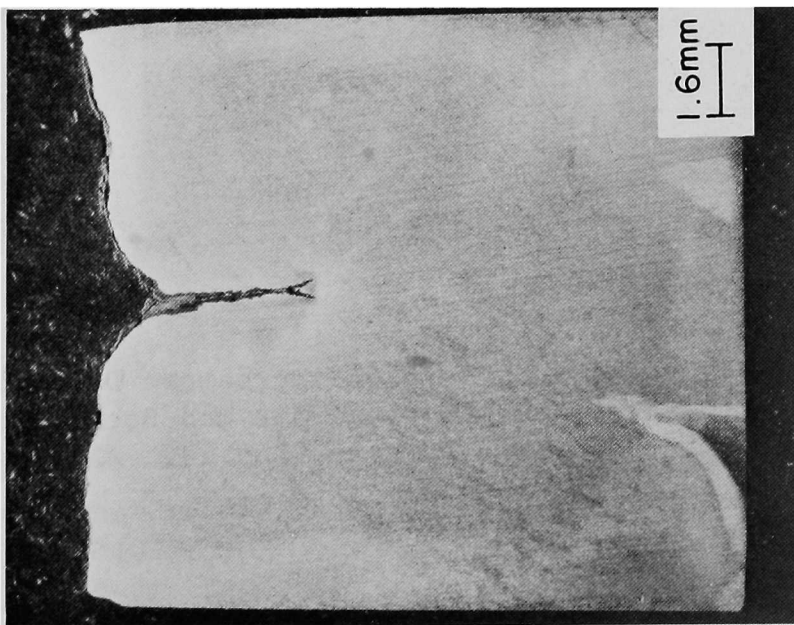
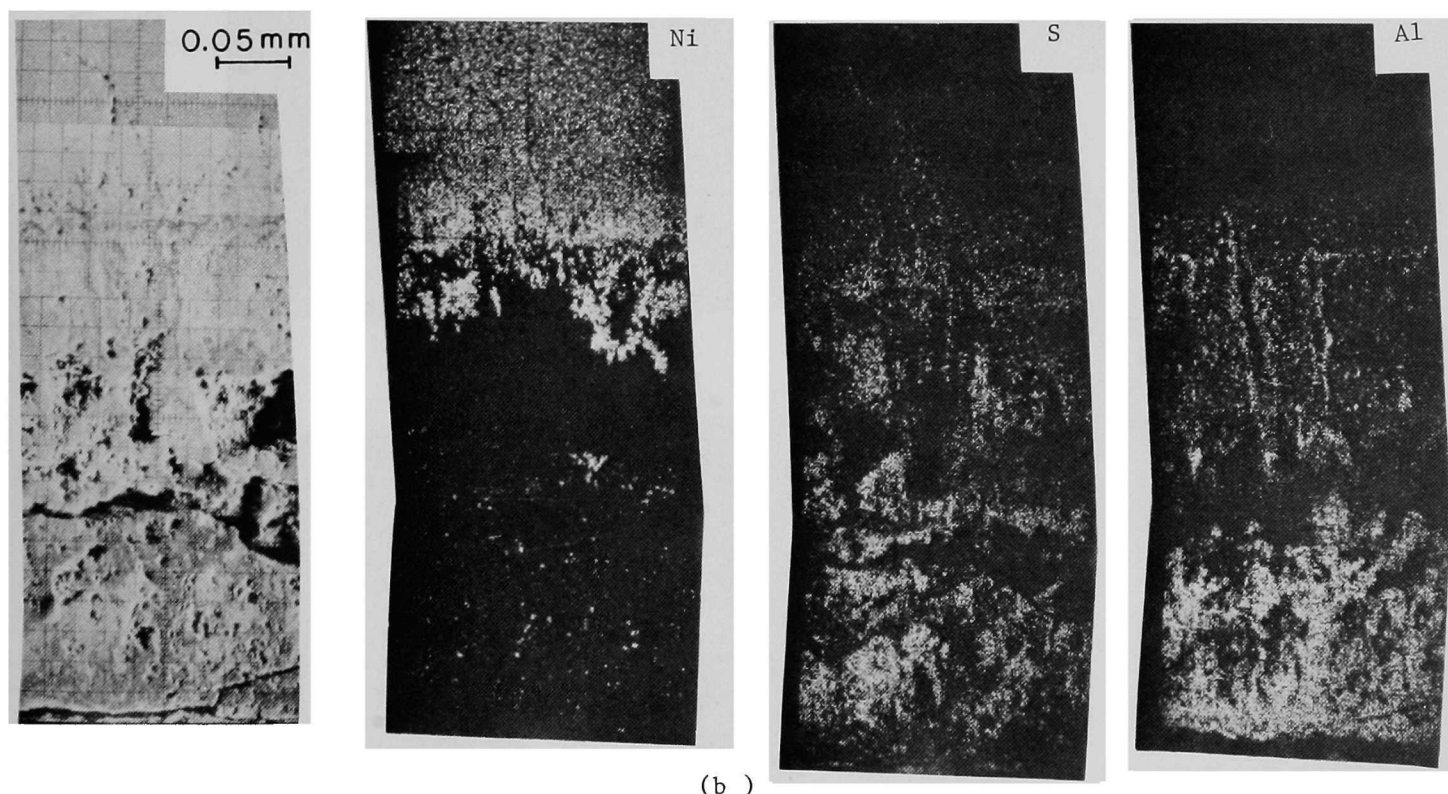Fig. 51. Photographs of a Crack that had been Electroetched. ANL Neg. No. 306-77-197.

75
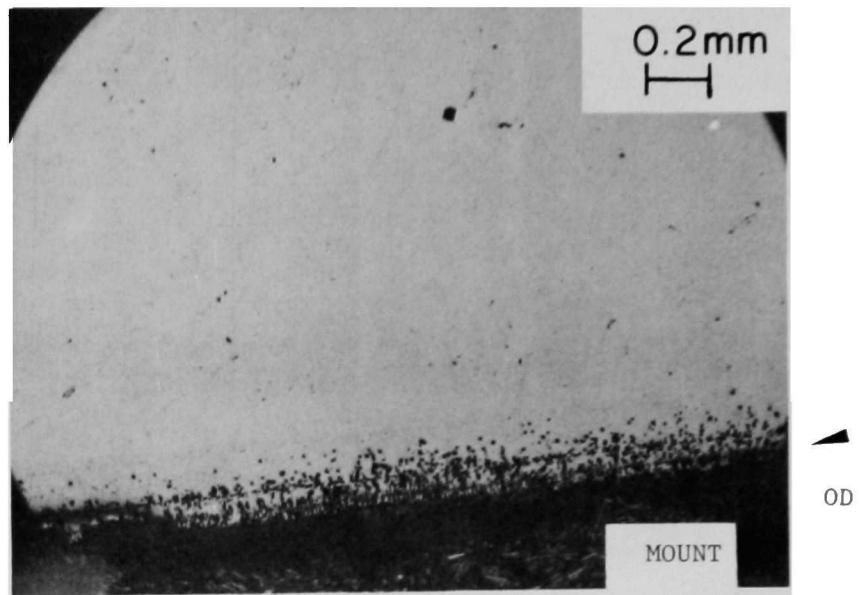
(a.)
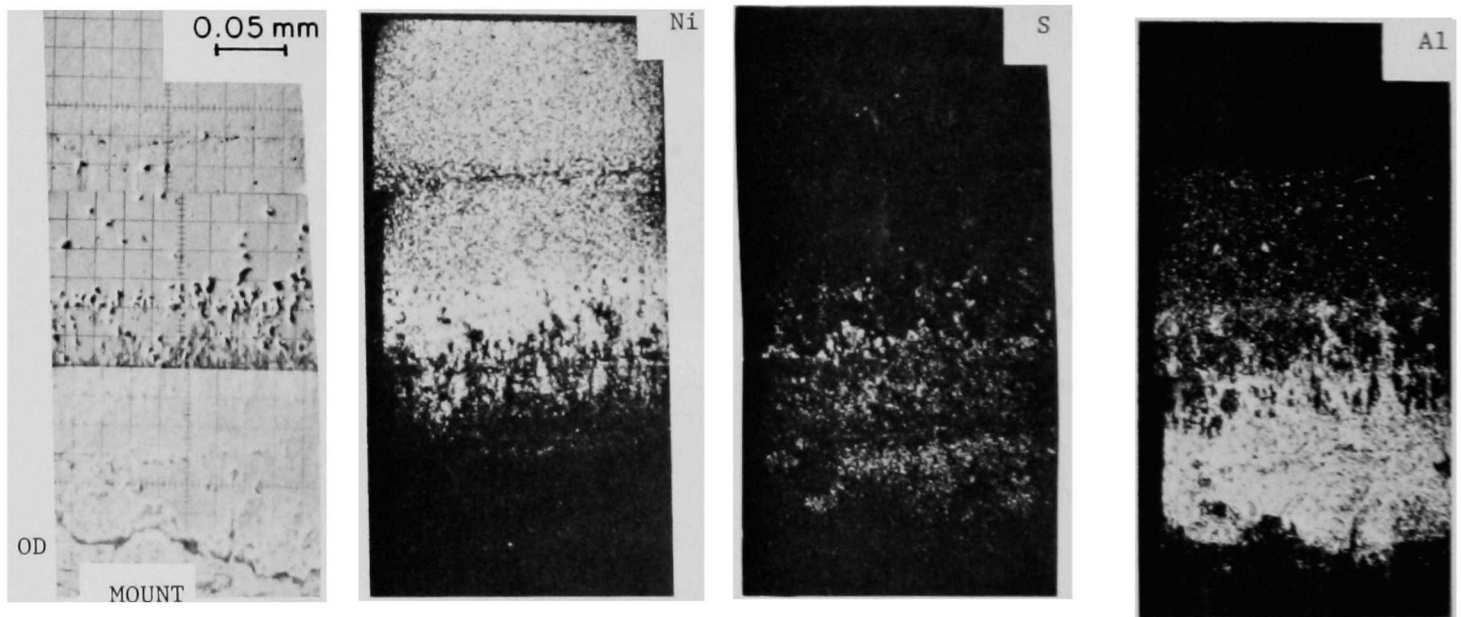
(b)

Fig. 52. Optical Photograph (a) and Electron-microprobe Data (b) of an "Alonized" Type 316 Stainless Steel Coupon That Had Been Exposed to the HYGAS Gasifier Environment and Removed after Run 61. ANL Neg. No. 306-77-4.
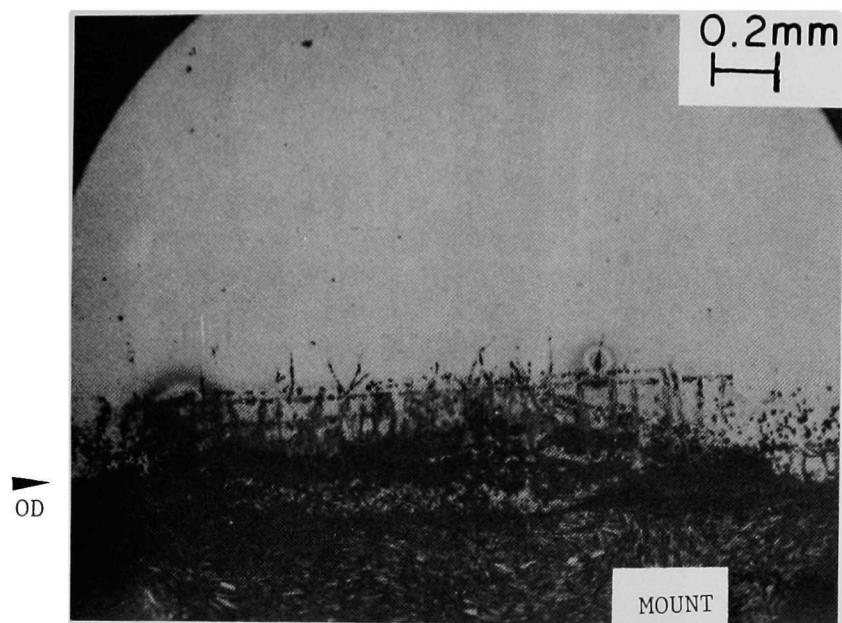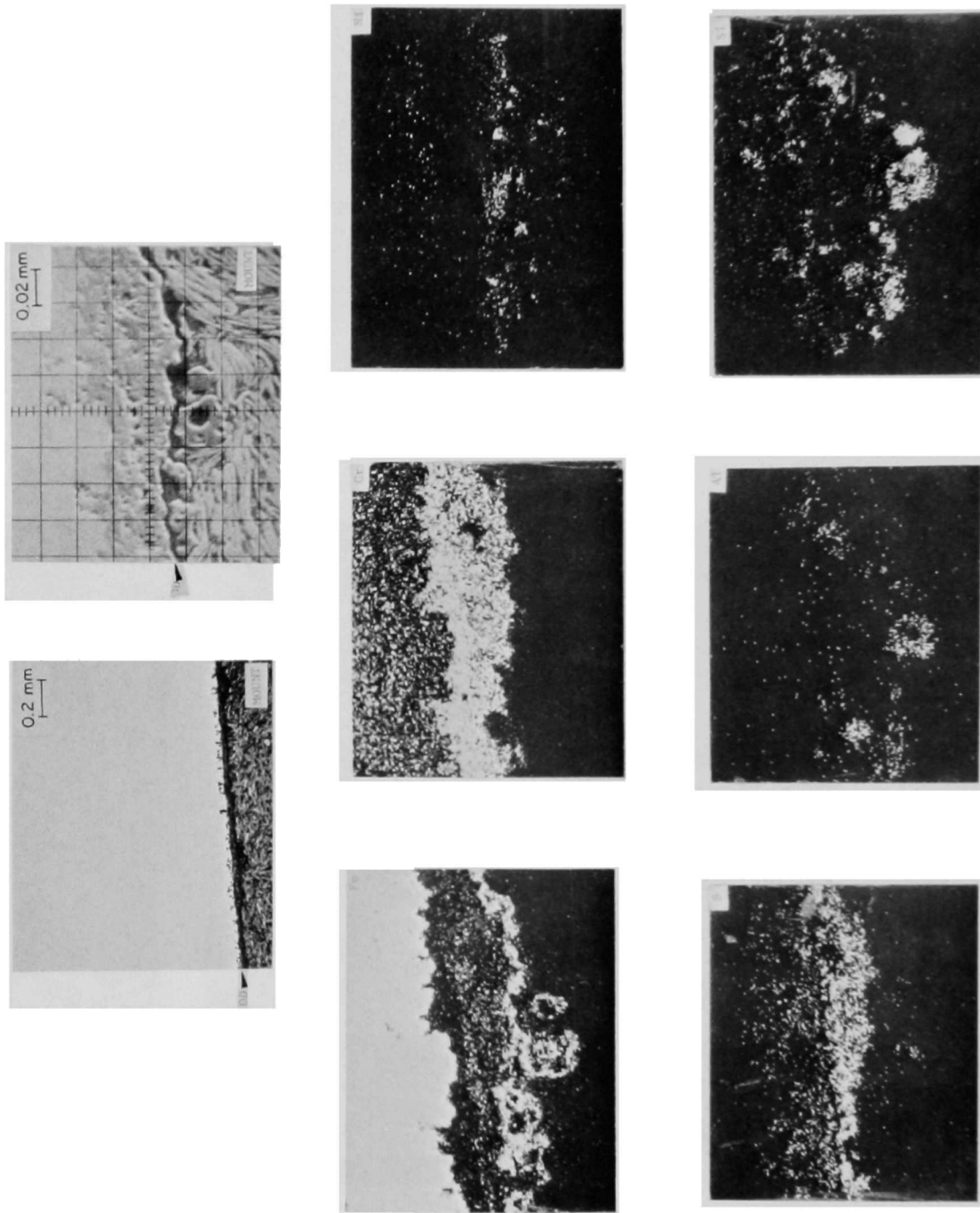
(a)

(b)

Fig. 53. Optical Photograph (a) and Electron-microprobe Data (b) of an
"Alonized" Type 316 Stainless Steel Coupon That Had Been Exposed to the
HYGAS Gasifier Environment and Removed after Run 67.

Fig. 54. Optical Photograph and Electron-microprobe Data of an "Alonized" Type 446 Stainless Steel Coupon That Had Been Exposed to the HYGAS Gasifier Environment and Removed after Run 61. ANL Neg. No. 306-77-189.
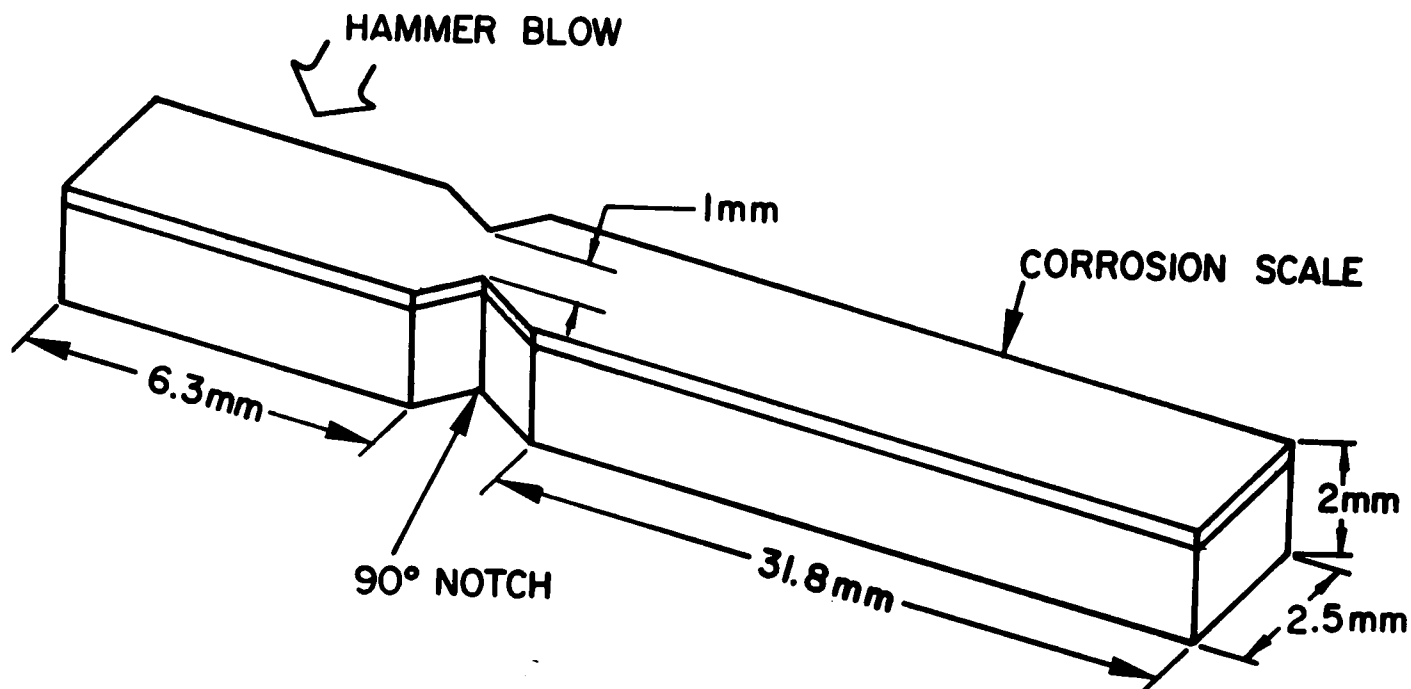
Fig. 55. Geometry of Machined Coupons Used for the Auger Experiment. ANL
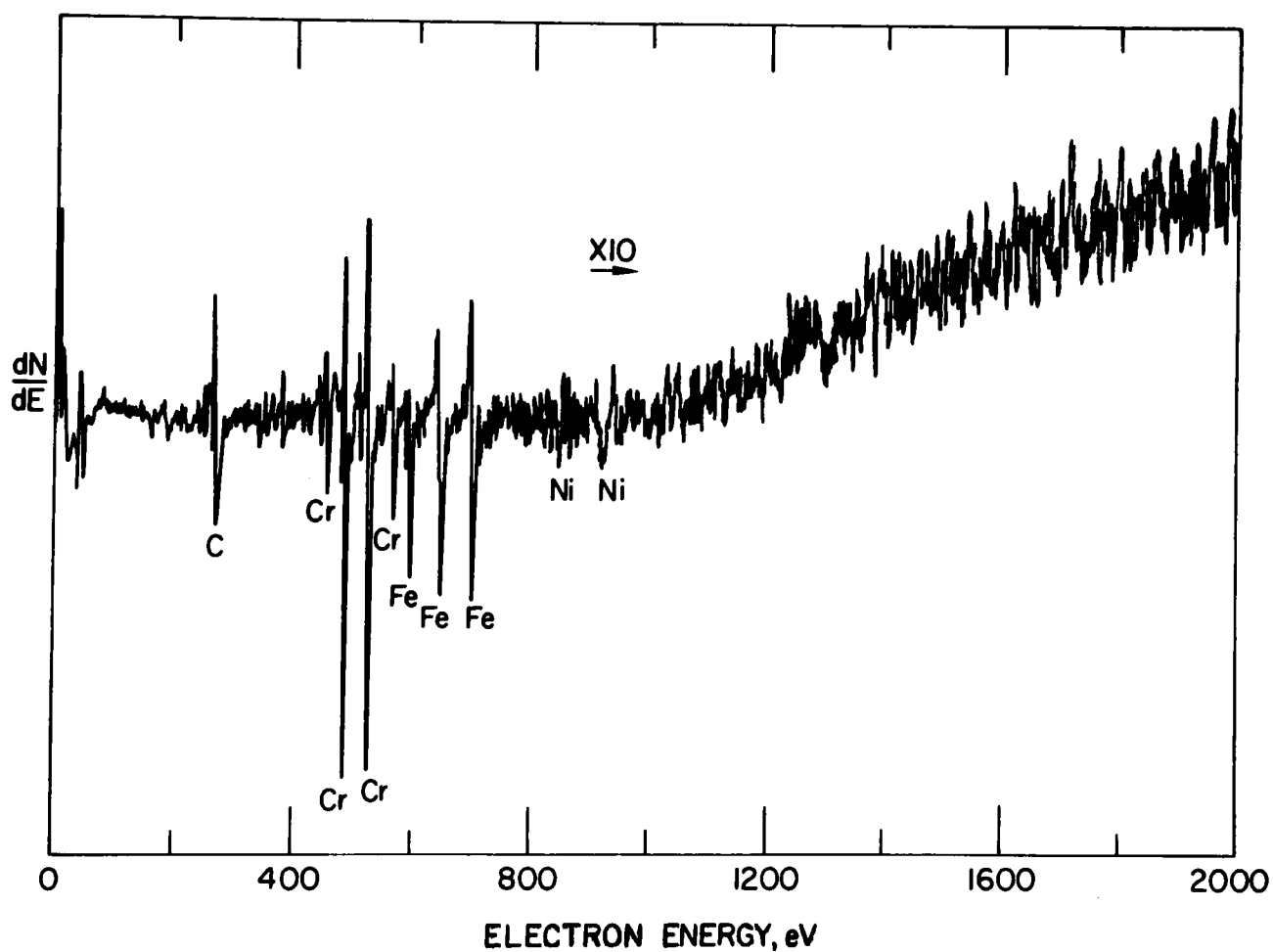Neg. No. 306-77-174.

Fig. 56. Auger Spectra of the As-fractured Type 316 Stainless Steel.
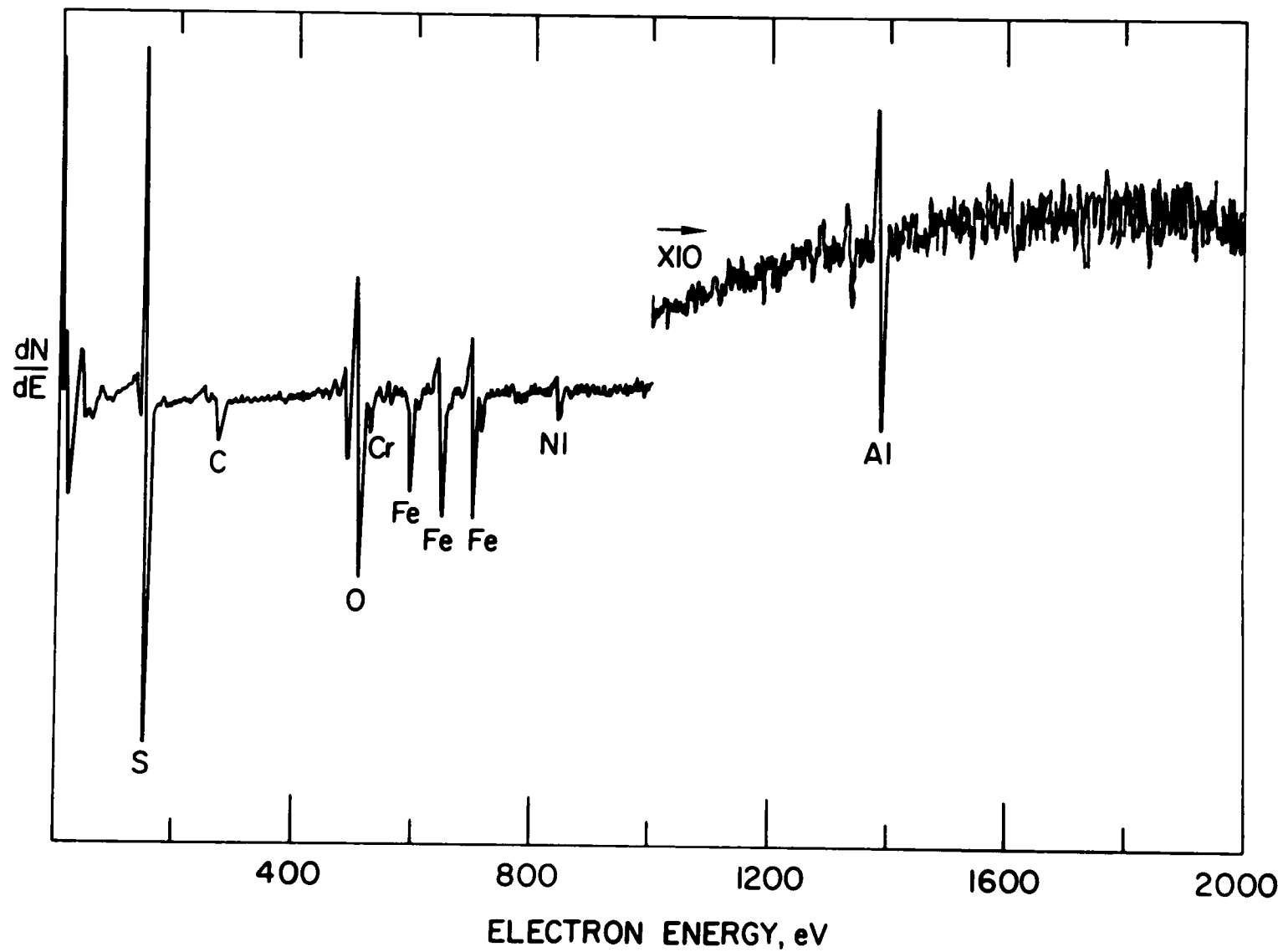ANL Neg. No. 306-77-171.

Fig. 57. Auger Spectra of the Corrosion Scale at the Type 316 Stainless Steel
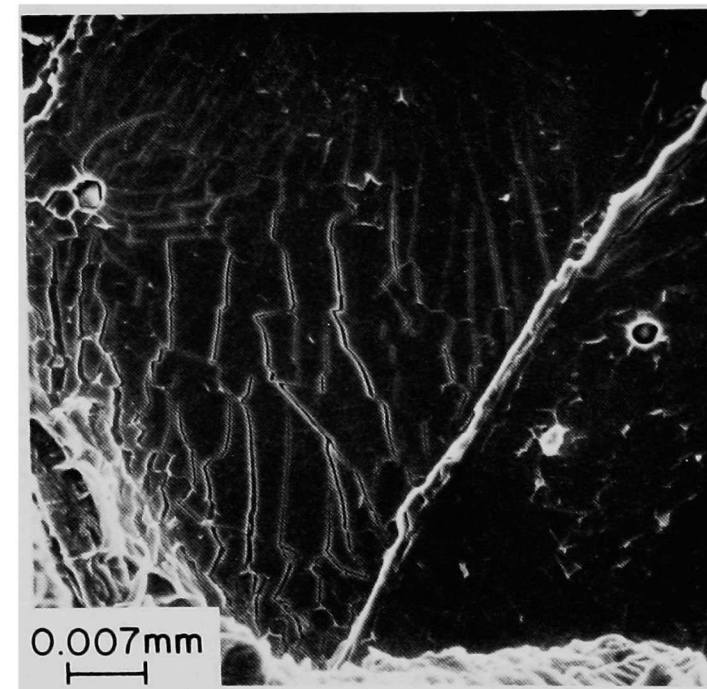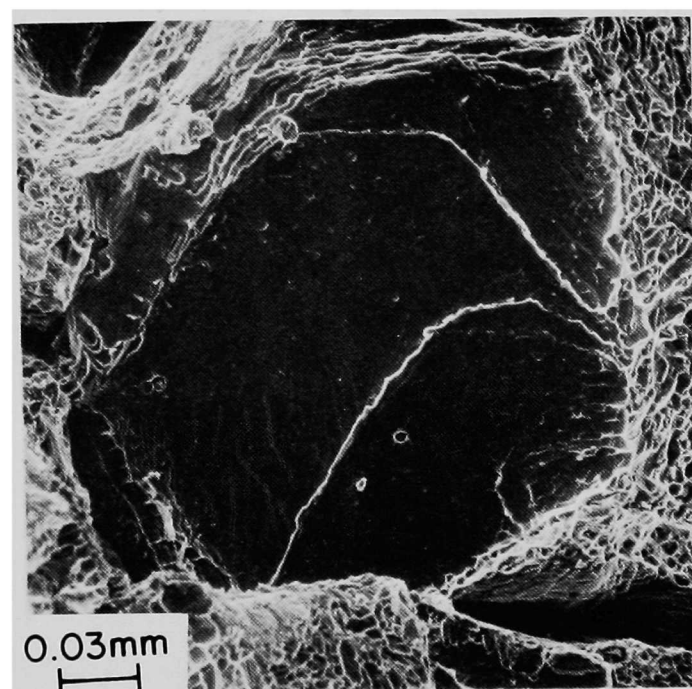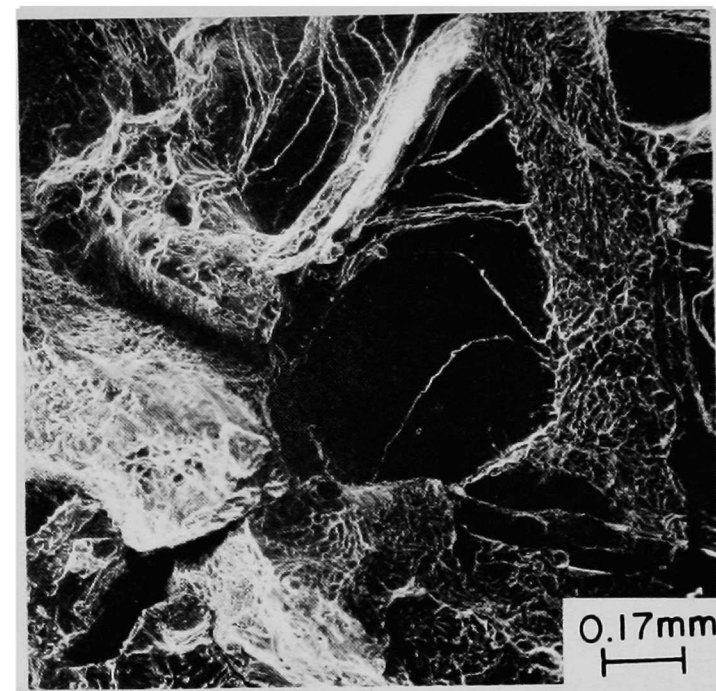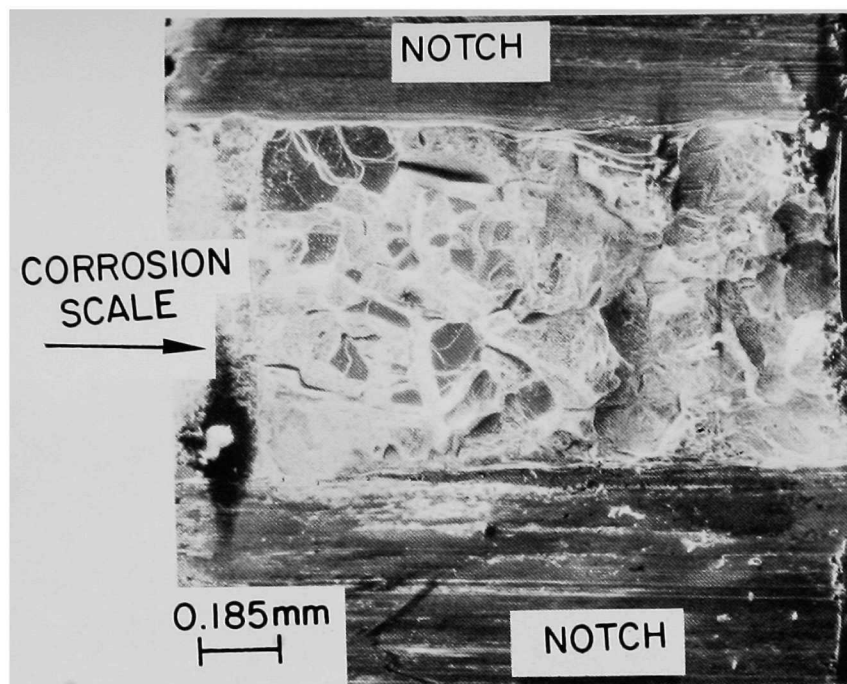Surface. ANL Neg. No. 306-77-176.

Fig. 58. SEM Micrographs of the Fracture Surface of Type 316 Stainless Steel Showing Embrittled Grain Boundaries. ANL Neg. No. 306-77-198.
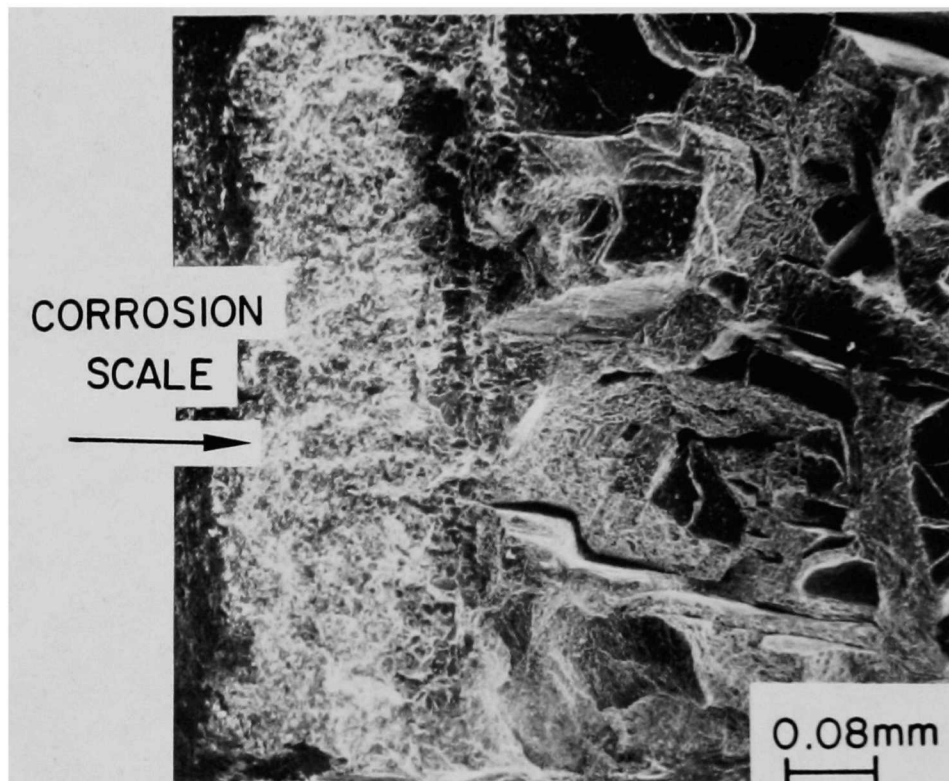
Fig. 59. SEM Micrograph of the Corrosion Scale and
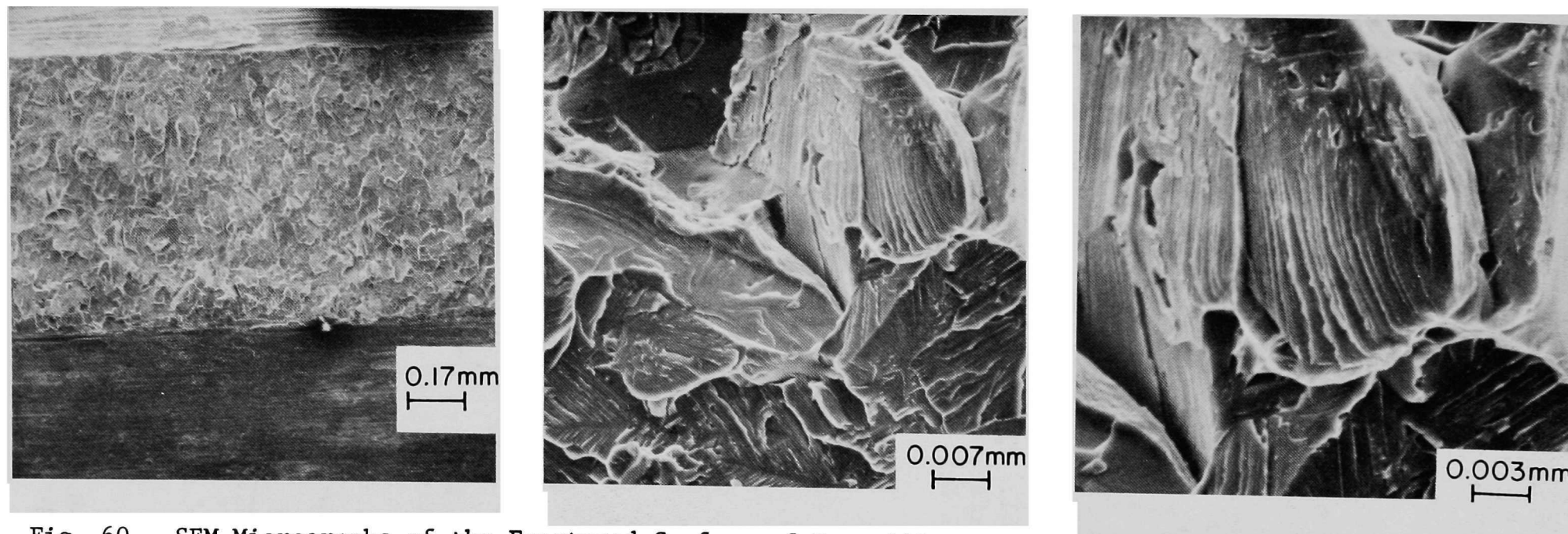the Fracture Surface of Type 316 Stainless Steel.
ANL Neg. No. 306-77-188.

Fig. 60. SEM Micrographs of the Fractured Surface of Type 446 Stainless Steel. ANL Neg. No. 306-77-200.
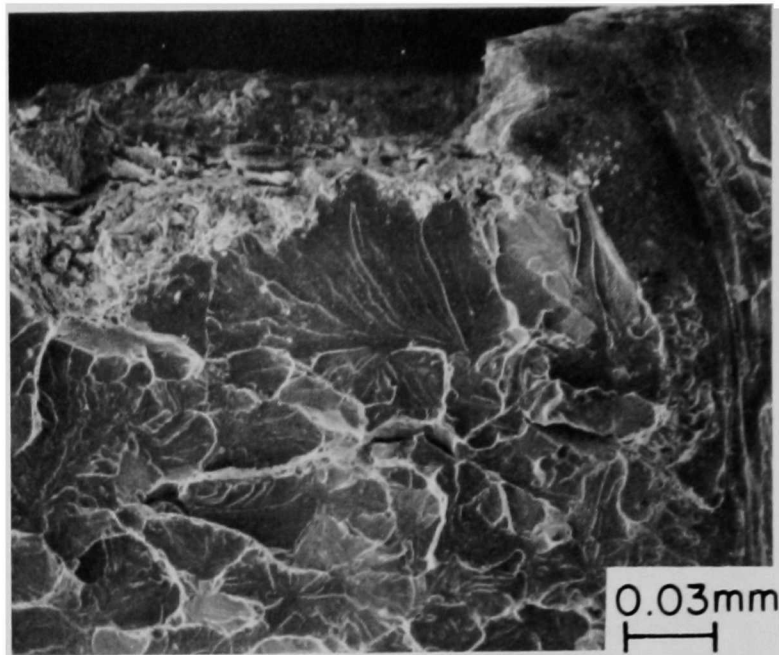
Fig. 61. SEM Micrograph of the Fractured
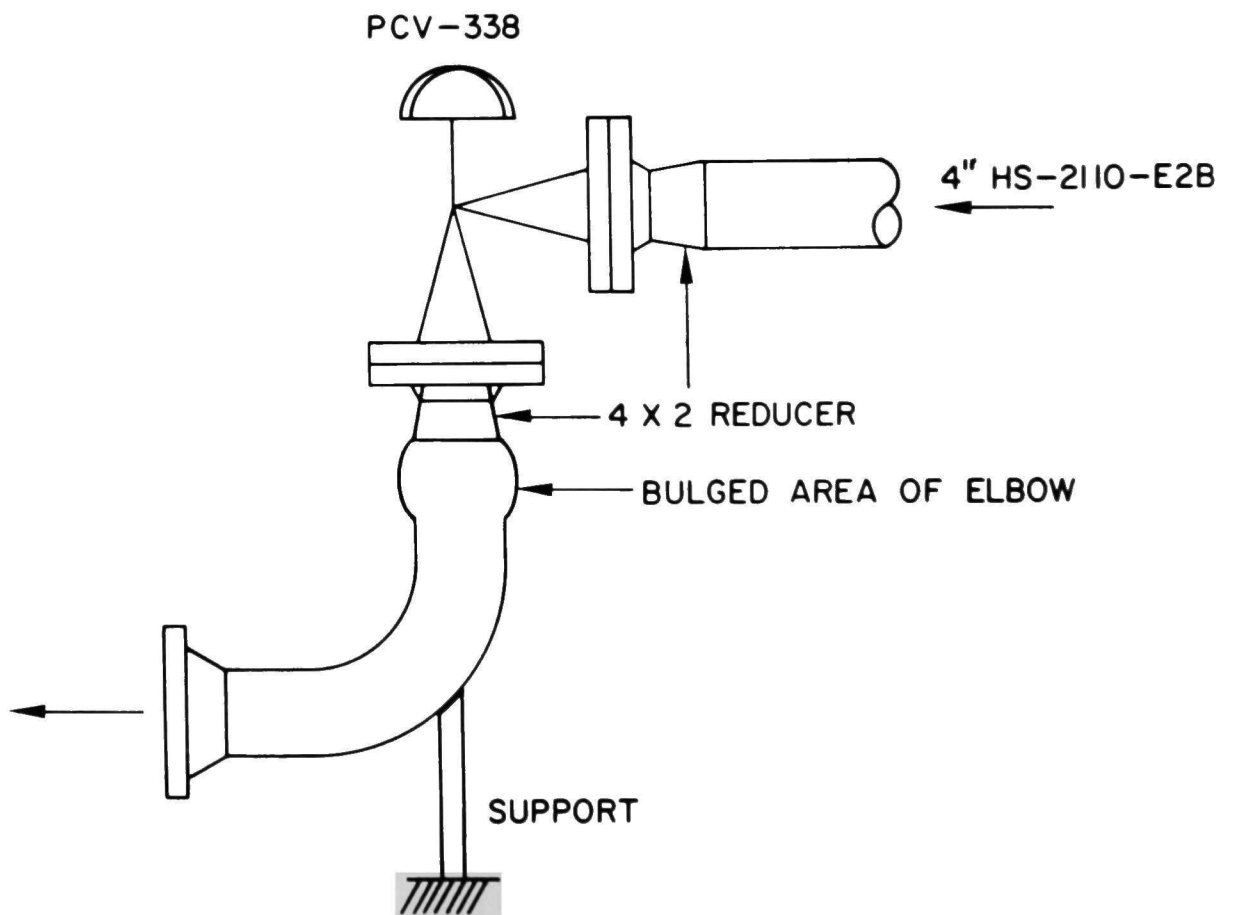Surface of Type 446 Stainless Steel.
ANL Neg. No. 306-77-184.

Fig. 62. Schematic Showing the Elbow, Bulged Pipe, and Letdown
Valve. ANL Neg. No. 306-77-180.

Internal:

E. G. Pewitt
R. O. Ivins
B. R. T. Frost
R. W. Weeks (6)
M. F. Adams
O. K. Chopra
S. Danyluk
D. R. Diercks
W. A. Ellingson (6)
J. Fischer
K. J. Reimann

A. A. Jonke
T. F. Kassner
C. R. Kennedy
K. Natesan
J. L. Nivens
J. Y. Park
R. B. Poeppel
W. J. Shack
A. B. Krisciunas
ANL Contract Copy
ANL Libraries (5)
TIS Files (6)

External:

ERDA-TIC, for distribution per UC-90h (231)
Manager, Chicago Operations Office
Chief, Chicago Patent Group
President, Argonne Universities Association
Materials Science Division Review Committee:
    G. S. Ansell, Rensselaer Polytechnic Inst.
    R. W. Balluffi, Cornell Univ.
    S. Doniach, Stanford Univ.
    H. L. Falkenberry, Tennessee Valley Authority
    C. Laird, Univ. Pennsylvania
    D. Lazarus, Univ. Illinois
    M. T. Simnad, General Atomic
    A. R. C. Westwood, Martin Marietta Laboratories
R. R. Adams, Battelle Columbus Laboratories
E. M. Anderson, The Babcock & Wilcox Company
W. G. Bair, Inst. of Gas Technology
W. Bakker, USERDA/FE
S. Carson, CE Lummus Co., Bruceton, Pa.
A. Conn, Amoco Oil Co., Naperville, Ill.
W. C. Corder, Battelle Columbus Laboratories
M. Crowley, Standard Oil of Indiana, Naperville, Ill.
J. Flagg, Universal Oil Products Co., Des Plaines, Ill.
E. Fox, Stearns-Roger Corp., Homer City, Pa.
H. E. Frankel, USERDA/FE
S. M. Gaitonde, Commonwealth Edison Co., Maywood, Ill.
D. Glaser, Stearns Roger Corp., Denver
H. Heysteck, Tuscaloosa Metallurgy Research Center, University, Ala.
V. Hill, IIT Research Inst.
D. Hull, Phillips Petroleum Co., Homer City, Pa.
R. I. Jaffee, Electric Power Research Institute
D. L. Keairns, Westinghouse Research Labs.
H. Leavenworth, Albany Metallurgy Research Center
A. V. Levey, Lawrence Berkeley Laboratory
R. Lewis, Synthane Pilot Plant, USERDA/FE, Pittsburgh
G. Long, Northern Illinois Gas Co., Aurora
R. M. Lundberg, Commonwealth Edison Co., Chicago

J. M. O'Donnell, The Lummus Co., Bloomfield, N.J.
A. L. Plumley, Combustion Engineering Power Systems, Windsor
J. Pope, Science Applications, Inc.
A. Schaeffer, Metals Properties Council, New York
S. J. Schneider, National Bureau of Standards
J. R. Schorr, Battelle Columbus Laboratories
J. Stevenson, Rolla Metallurgy Research Center
J. Sudbury, Consolidated Coal Co., Library, Pa.
C. Whitten, Peabody Coal Co., Columbia, Tenn.
F. Woods, Albany Metallurgy Research Center